ARL-CR-0850 ● June 2020

Conceptual Design: Optimization of Medium-Scale Unmanned Aerial Vehicle Propulsion System

by Hans DeSmidt

under contract W911NF-18-2-0025

NOTICES

Disclaimers

ARL-CR-0850 ● June 2020

Conceptual Design: Optimization of Medium-Scale Unmanned Aerial Vehicle Propulsion System

Hans DeSmidt
University of Tennessee

under contract W911NF-18-2-0025

REPORT DOCUMENTATION PAGE

Form Approved
OMB No. 0704-0188

1. REPORT DATE *(DD-MM-YYYY)* June 2020	**2. REPORT TYPE** Contractor Report	**3. DATES COVERED (From - To)** 12 March 2018–11 March 2019

4. TITLE AND SUBTITLE
Conceptual Design: Optimization of Medium-Scale Unmanned Aerial Vehicle Propulsion System

5a. CONTRACT NUMBER
W911NF-18-2-0025

5b. GRANT NUMBER

5c. PROGRAM ELEMENT NUMBER

6. AUTHOR(S)
Hans DeSmidt

5d. PROJECT NUMBER

5e. TASK NUMBER

5f. WORK UNIT NUMBER

7. PERFORMING ORGANIZATION NAME(S) AND ADDRESS(ES)
University of Tennessee
1038 20th Street
Knoxville, TN 37916

8. PERFORMING ORGANIZATION REPORT NUMBER
ARL-CR-0850

9. SPONSORING/MONITORING AGENCY NAME(S) AND ADDRESS(ES)
CCDC Army Research Laboratory
ATTN: FCDD-RLV-P
Aberdeen Proving Ground, MD 21005

10. SPONSOR/MONITOR'S ACRONYM(S)

11. SPONSOR/MONITOR'S REPORT NUMBER(S)

12. DISTRIBUTION/AVAILABILITY STATEMENT
Approved for public release; distribution is unlimited.

13. SUPPLEMENTARY NOTES
ORCID ID: Hans DeSmidt, 0000-0002-5012-3020

14. ABSTRACT

The goal of this project is to explore propulsion system configurations and designs for medium-scale (100–1000 lb payload) unmanned aerial vehicles (UAVs) with vertical takeoff and landing (VTOL) capabilities. Recently, there has been much interest in developing medium-scale VTOL UAVs for support, resupply, and search and rescue operations. Such UAVs will need to have sufficient endurance, must have inherent safety when operating in close proximity to personnel, and must be capable of transporting payloads on the order of 500 lb distances on the order of 10 km. Such medium-scale UAVs currently fall into somewhat of a gray area for propulsion system designs. At the large-scale end of the spectrum, the optimal propulsion system design is based on a conventional gas turbine engine/shaft/gearbox/rotor mechanical configuration. While at the limit of the small scale, a pure electric battery/motor/rotor propulsion system similar to many RC hobby drones or so-called micro aerial vehicles (MAVs) is most feasible and practical. In the middle scale, however, it is not yet clear what the optimal propulsion system configuration for VTOL UAV applications would be. To advance the state of the art, this project will design and compare several conceptual propulsion system configurations for a medium-scale VTOL UAV application.

15. SUBJECT TERMS
UAV, VTOL, hybrid-electric propulsion, electric propulsion, optimization

16. SECURITY CLASSIFICATION OF:			**17. LIMITATION OF ABSTRACT**	**18. NUMBER OF PAGES**	**19a. NAME OF RESPONSIBLE PERSON**
					Mark Riggs
a. REPORT	**b. ABSTRACT**	**c. THIS PAGE**			**19b. TELEPHONE NUMBER (Include area code)**
Unclassified	Unclassified	Unclassified	UU	94	(410) 278-9604

Standard Form 298 (Rev. 8/98)
Prescribed by ANSI Std. Z39.18

Contents

List of Figures

List of Tables

Acknowledgments

This research was funded by the Government under Agreement No. W911NF-18-2-0025. The US Government is authorized to reproduce and distribute reprints for Government purposes notwithstanding any copyright notation thereon.

1. Introduction

The goal of this project is to explore propulsion system configurations and designs for medium-scale (100–1000 lb payload) unmanned aerial vehicles (UAVs) with vertical takeoff and landing (VTOL) capabilities. Recently, there has been much interest in developing medium-scale VTOL UAVs for support, resupply, and search and rescue operations. Such UAVs will need to have sufficient endurance, must have inherent safety when operating in close proximity to personnel, and must be capable of transporting payloads on the order of 500 lb distances on the order of 10 km. Such medium-scale UAVs fall into a gray area of propulsion system design. At the large-scale end of the spectrum, the optimal propulsion system design is based on a conventional gas turbine engine/shaft/gearbox/rotor mechanical configuration. While at the limit of the small scale, a pure electric battery/motor/rotor propulsion system similar to many RC hobby drones or so-called micro aerial vehicles (MAVs) is most feasible and practical. In the middle scale, however, it is not yet clear what the optimal propulsion system configuration for VTOL UAV applications would be.

A hybrid-electric vehicle (HEV) is “a vehicle in which propulsion energy is available from two or more kinds or types of energy stores, sources, or converters, and at least one of them can deliver electrical energy.”[1] Within the automotive industry, HEV technology is leading to vehicles with increased fuel economy and reduced emissions. The same technology would have similar benefits if applied to UAVs. Because of the hybrid and electric-only modes, the potential benefits include increased time on station, longer range, and reduced signature. A parallel hybrid-electric propulsion system for a small UAV provides increased time on station and longer range as compared to electric-powered UAVs such as the Dragon Eye or Desert Hawk.[2] The internal combustion (IC) engine is downsized for steady-state conditions and operated near a constant torque output. The electric motor (EM) provides additional power for acceleration or climbing and serves as a generator during charge-sustaining operation or regeneration. Electric-only operation reduces the acoustic, smoke, and thermal signatures as compared to gasoline-powered UAVs.[3] The battery pack/generator that usually provides power for the avionics, flight control system, and payload also provides propulsion power during certain flight phases. The electric system also provides redundancy for the gasoline engine. The Defense Advanced Research Projects Agency (DARPA) and other agencies are considering hybrid-electric propulsion systems for its MAV program.[4] The MAV is a vertical takeoff and landing vehicle utilizing ducted fan technology. A series hybrid-electric propulsion system that includes a diesel engine, generator, electric motor, and battery pack has been considered for the

MAV.[5] Furthermore, NASA's high-altitude, long-endurance UAV, Helios, is designed for telecommunications and atmospheric monitoring.[6] Also, Israel Institute of Technology researched the concept of using a hybrid-propulsion system for a high-altitude long-endurance UAV.[7] Most recently, Top Flight Technologies, a manufacturer of multirotor UAV solutions, has developed a hybrid gas-electric multirotor UAV called the Airborg H6. This quad rotor UAV has a total takeoff weight of 55 lb and uses a serial gas-electric hybrid propulsion system that has achieved 2+ hour flight endurance and a 100-mile range.[8] These projects illustrate that various organizations are evaluating hybrid-electric propulsion systems for aerospace applications.

To advance the state-of-the-art, this project designs and compares several conceptual propulsion system configurations for a medium-scale (100–1000 lb payload) VTOL UAV application. Specifically, this study develops sizing and design codes for a multirotor UAV for three different propulsion system architectures: 1) IC engine gas/mechanical, 2) battery-electric, and 3) series gas-electric hybrid concept. Table 1 summarizes the configurations which are designed and evaluated in this study.

Table 1 Propulsion system concepts for VTOL UAV

Drive system	IC engine	Electric motor	Flight control	Battery pack	Generator	Distribution drive shafts	Gearboxes	Rotor config.
IC engine/ mechanical	Centralized engine[a]	No	Collective pitch	No	No	Yes	3 stages (X and H configs.)	Multirotor (4, 6, and 8 rotors considered)
Battery-electric	No	Nacelle motors[b]	Variable RPM[c]	Yes	No	No	1 stage	
Series gas-electric hybrid	Centralized engine[a]	Nacelle motors[b]	Variable RPM[c]	Yes	Yes	No	2 stage	

[a] Single IC engine within the fuselage
[b] One motor per rotor located within each rotor nacelle
[c] RPM = revolutions per minute

The focus of this study is aimed around a VTOL UAV application. Hence, the typical quadrotor configuration (Fig. 1) is selected as the basis upon which the three different propulsion system architectures are compared. Along these lines, no fixed-wing flight surfaces are included in the study. In addition to quadrotors, this study also considers multirotor designs greater than four rotors to further evaluate any benefits of distributed electric propulsion over mechanical shaft power distribution.

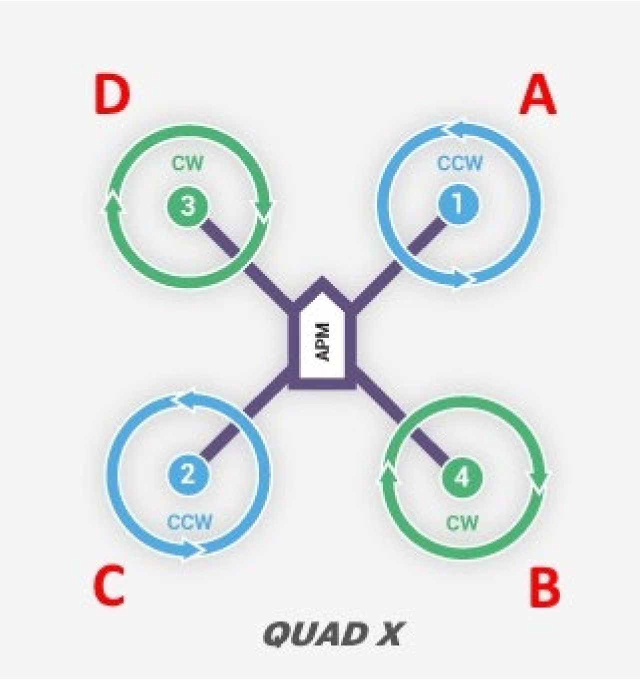

Fig. 1 Quadrotor layout (X layout) for VTOL UAV platform

The quad and multirotor configurations have several inherent benefits for the medium-scale VTOL UAV application. In particular, the multirotor configuration lends itself to smaller diameter rotors, which can be more easily shrouded or have ducted fans which enhance ground personnel safety. Furthermore, the quadrotor configuration enables full flight control authority via either collective pitch or rotor RPM variations, thus avoiding the need for cyclic pitch control and complex swash plate mechanisms.

The objectives of this project are summarized as follows:

- Develop a design code for sizing each of the proposed mechanical, electrical, and hybrid-electric propulsion systems in a quadrotor UAV platform for a given range, payload, and flight time based on idealized quasi-steady operation.
- Evaluate flight performance and determine the maximum range, speed, and payload for several mission scenarios.
- Explore and evaluate the benefits of direct-drive versus single and multistage gear-reduced transmissions in each configuration.
- Perform a comparison study to evaluate benefits and drawbacks of each drive system architecture.

The modeling, design, and performance results for each of the three architectures is described in Sections 2–4 of this report. Furthermore, the comparisons study is detailed in Section 5 and finally the conclusions and recommendations are given in Section 6.

2. Battery-Electric Configuration

The design and analysis of the system is conducted based on the assumption of quasi-steady operation. Figure 2 shows a schematic of the battery-electric quadrotor UAV considered in this section.

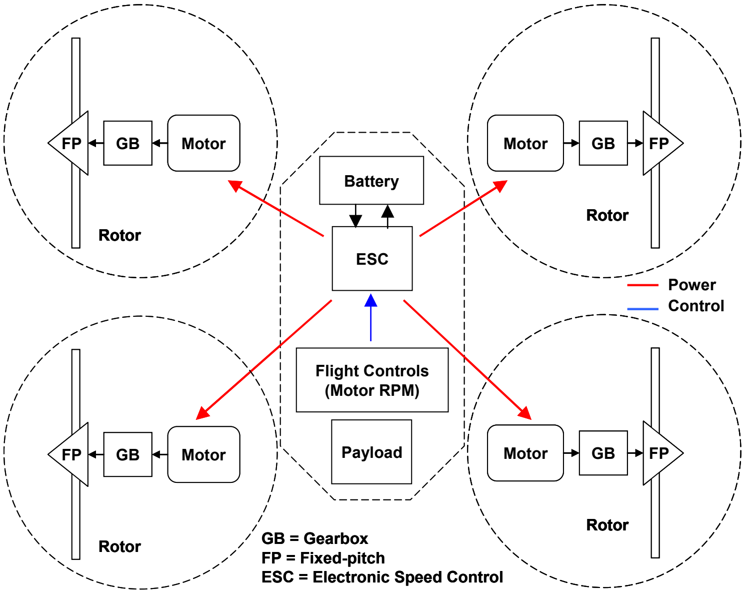

Fig. 2 Quadrotor UAV with battery-electric propulsion and variable rotor speed flight control

An iterative sizing algorithm and design code is developed and utilized to obtain a family of feasible designs. The hover and forward flight performance of these designs is then evaluated for a variety of payloads and forward flight speeds.

2.1 Modeling and Design of Battery-Electric Configuration

To evaluate the hover and forward flight performance, the total gross weight of the vehicle must be computed. The total mass, m, and empty mass, m_{empty}, are

$$\begin{aligned} m_{empty} &= (m_r + m_{gb} + m_m)N_r + m_{esc} + m_s \\ m &= m_{empty} + m_b + m_p \end{aligned} \tag{1}$$

Here m_{empty} is composed of the rotor mass, m_r, gearbox mass, m_{gb}, DC electric motor mass, m_m, electronic speed controller (ESC) mass, m_{esc}, and the vehicle structural mass m_s. As shown in Fig. 2, and by Eq. 1, some of the components are duplicated by the number rotors, N_r. In order to size the system components, an iterative design code is developed which determines the size of each component based on power and energy requirements during hover for a given battery mass, m_b, and payload mass, m_p. The flowchart of the sizing algorithm developed under this project for the battery-electric UAV configuration is shown in Fig 3.

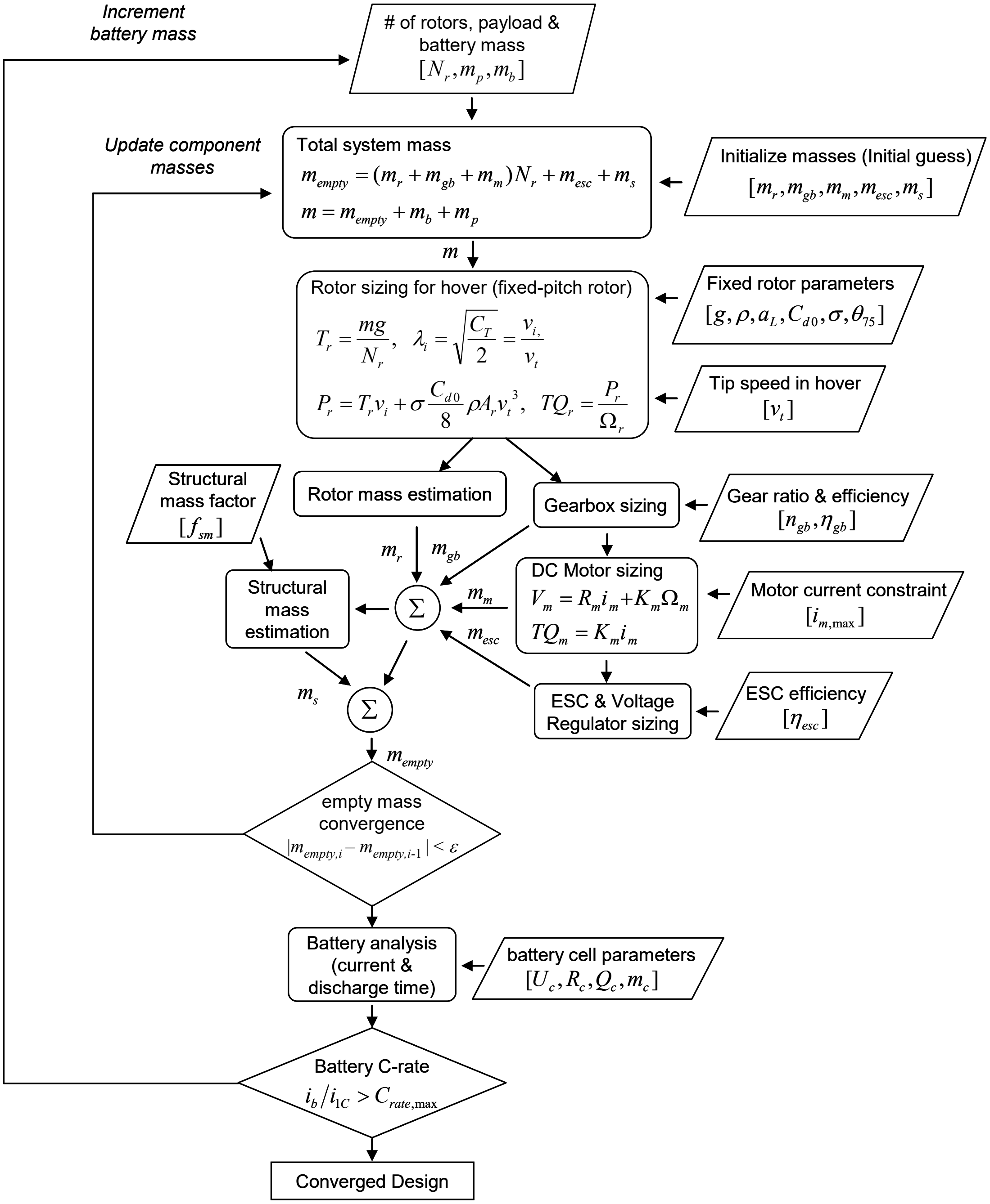

Fig. 3 Iterative sizing algorithm for design of the multirotor VTOL UAV with battery-electric propulsion and variable RPM rotor flight control

Starting with initialized mass estimates for each component, the required rotor thrust, T_r, blade tip speed, v_t, and rotor power, P_r, is computed. These results are then propagated down the drivesystem where each subsequent component is sized based on the required rotational speed and power levels. The updated component masses from the *ith* iteration step are then used to generate a new estimate, $m_{empty,i}$, which is compared with the prior estimate, $m_{empty,i\text{-}1}$, to evaluate convergence (see Fig. 3). The details of each component model and sizing equations are described in the following subsections.

2.1.1 Hover and Forward-Flight Aeromechanics Model

For a given total gross weight, *W*, and steady forward speed, v_v, the trim solution for the required rotor thrust, T_r, and vehicle angle of attack, α, is (see Fig. 4)

$$T_r = \frac{\sqrt{W^2 + D^2}}{N_r} \qquad \text{and} \qquad \alpha = \tan^{-1`}\left(\frac{D}{W}\right) \tag{2-a}$$

where weight, *W*, is computed based on *m* and gravitational acceleration constant *g*

$$W = mg \tag{2-b}$$

and the vehicle aerodynamic drag force, *D,* is computed as

$$D = \frac{1}{2}\rho C_d S {v_v}^2 \tag{2-c}$$

where ρ is air density, C_d is vehicle drag coefficient, and *S* is vehicle frontal area. In this study the product $C_d S$ is estimated based on vehicle mass adapted from Johnson[9] as

$$f_d = C_d S = 0.015 * 0.6 m^{\frac{2}{3}} \tag{3}$$

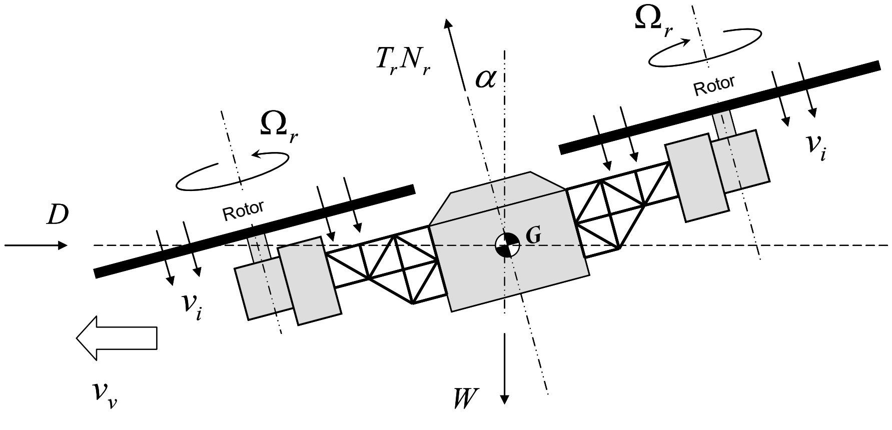

Fig. 4 Multirotor UAV in trimmed forward flight

Utilizing Momentum Theory under the assumption of uniform inflow, the relationship between T_r and induced velocity, v_i, is

$$T_r = 2\rho A_r v_i \sqrt{{v_v}^2 + 2 v_v v_i \sin\alpha + {v_i}^2} \tag{4}$$

Where A_r is rotor disk area.[9] The design code computes v_i from the roots of the following polynomial, which is obtained by combining Eqs. 2–4.

$${v_i}^4 + 2 v_v {v_i}^3 \sin\alpha + v_v {v_i}^2 - \frac{W^2 + D^2}{{N_r}^2 4\rho^2 A^2} = 0 \tag{5}$$

Next, as usual, we define the rotor thrust coefficient, C_T, as

$$C_T = \frac{T_r}{\rho A_r {v_t}^2} \tag{6}$$

Where v_t is blade tip speed, which can be expressed in terms of rotor rotational speed, Ω_r, and rotor disk radius, R_r, as

$$v_t = \Omega_r R_r \tag{7}$$

and where R_r is related to the rotor disk area via

$$A_r = \pi {R_r}^2 \tag{8}$$

Next, in the usual way, we define the rotor inflow ratio, λ_i, and advance ratio, μ

$$\lambda_i = \frac{v_v \sin\alpha + v_i}{v_t} \quad \text{and} \quad \mu = \frac{v_v \cos\alpha}{v_t} \tag{9}$$

Combining Eqs. 4, 6, and 9 we obtain

$$C_T = 2\lambda_i \sqrt{\mu^2 + (\mu \tan\alpha + \lambda_i)^2} \tag{10}$$

Furthermore, applying Blade Element theory to a rotor with linearly twisted blades along with the uniform inflow approximation we obtain

$$C_T = a_L \frac{\sigma}{2}\left[\frac{\theta_{75}}{3}\left(1 + \frac{3}{2}\mu^2\right) - \frac{\lambda_i}{2}\right] \tag{11}$$

Where a_L, σ, and θ_{75} are rotor blade lift coefficient slope, rotor solidity, and blade pitch at the three-quarters radial location, respectively. Furthermore, the power required to drive an individual rotor, P_r, is computed as

$$P_r = T_r v_i + \sigma \frac{C_{d0}}{8}\left(1 + 4.6\mu^3\right)\rho A_r {v_t}^3 + \frac{D v_v}{N_r} \tag{12}$$

Which accounts for induced, parasitic, and profile power. Here, C_{d0}, is blade drag coefficient. Finally, the torque required to drive the rotor is

$$TQ_r = \frac{P_r}{\Omega_r} \tag{13}$$

2.1.2 Fixed-Pitch Variable Speed Rotor Trim Solution in Forward Flight

In the case of fixed-pitch rotors, which are assumed for both the battery-electric and series gas-electric hybrid cases evaluated in this study, trimmed hover and forward flight are achieved by adjusting Ω_r. For constant blade parameters [a_L, σ, θ_{75}] and given flight condition [v_v, v_i, α], the trim solution is obtained by equating the C_T expressions, Eqs. 10 and 11, and then solving for the required blade tip speed, v_t, from the roots of resulting polynomial

$$a_4 {v_t}^4 + a_3 {v_t}^3 + a_2 {v_t}^2 + a_1 v_t + a_0 = 0 \tag{14-a}$$

Which has coefficients

$$\begin{aligned}
a_4 &= 4{a_L}^2\sigma^2{\theta_{75}}^2 \\
a_3 &= -12{a_L}^2\sigma^2\theta_{75}(v_i + v_v \sin\alpha) \\
a_2 &= 3{a_L}^2\sigma^2(4{\theta_{75}}^2{v_v}^2\cos^2\alpha + 3(v_i + v_v\sin\alpha)^2) \\
a_1 &= -18{a_L}^2\sigma^2\theta_{75}{v_v}^2\cos^2\alpha(v_i + v_v\sin\alpha) \\
a_0 &= 9({a_L}^2\sigma^2{\theta_{75}}^2{v_v}^4\cos^4\alpha) - 576({v_v}^2\cos^2\alpha(v_i + v_v\sin\alpha)^2 + ({v_i}^2 + {v_v}^2 - {v_v}^2\cos 2\alpha + 3v_iv_v\sin\alpha)^2)
\end{aligned} \tag{14-b}$$

After computing the multiple roots of Eq. 14, the code considers v_t to be the lowest real valued positive root as the physical solution.

2.1.3 Rotor Sizing Based on Hover Condition

To determine the required rotor disk area, A_r, the rotor is sized about the hover condition ($v_v = 0$) for a specified rotor tip speed, $v_t \equiv v_{t,h}$. Considering Eqs. 9–11 with $\mu = 0$ we have

$$C_{T,h} = a_L \frac{\sigma}{2}\left(\frac{\theta_{75}}{3} - \frac{1}{2}\sqrt{\frac{C_{T,h}}{2}}\right) \tag{15-a}$$

Where $C_{T,h}$, is the rotor thrust coefficient during hover given as

$$C_{T,h} = \frac{T_{r,h}}{\rho A_r {v_{t,h}}^2} \tag{15-b}$$

With rotor thrust during hover

$$T_{r,h} = \frac{mg}{N_r} \tag{16}$$

Combining Eqn. 15 with 16 we solve for A_r as

$$A_r = \frac{mg}{\rho a_L \sigma N_r v_{t,h}^{2}} \left(\frac{192}{3a_L\sigma + 32\theta_{75} - \sqrt{a_L\sigma(9a_L\sigma + 192\theta_{75})}} \right) \tag{17}$$

Thus the rotor operating speed during hover is computed as

$$\Omega_{r,h} = \frac{v_{t,h}}{R_r} \qquad \text{with} \qquad R_r = \sqrt{\frac{A_r}{\pi}} \tag{18}$$

Also, using Eqs. 12 and 13, the torque required to drive the rotor in hover is

$$TQ_{r,h} = \frac{1}{v_{t,h}} \sqrt{\frac{m^3 g^3}{2\rho\pi N_r^{3}}} + \sigma \frac{C_{d0}}{8} \rho\pi R_r^{3} v_{t,h}^{2} \tag{19}$$

Finally, the rotor mass is then estimated based on the following empirical relation[10]

$$m_r = p_1(2R_r)^2 + p_2 2R_r + p_3 \quad \text{Units}: R_r \ \{\text{inch}\},\ m_r\ \{\text{g}\} \tag{20}$$

With fitting coefficients $p_1 = 0.1207$, $p_2 = -0.5122$, and $p_3 = 0$ selected based on carbon fiber reinforced composite blades.

2.1.4 DC Electric Motor Model and Sizing

The motors considered in this study are considered to be permanent magnet DC electric motors.

Figure 5 shows a basic model of the DC motor with steady-state torque and voltage relations given as

$$\begin{aligned} V_m &= R_m i_m + K_m \Omega_m \\ TQ_m &= K_m i_m \end{aligned} \tag{21-a}$$

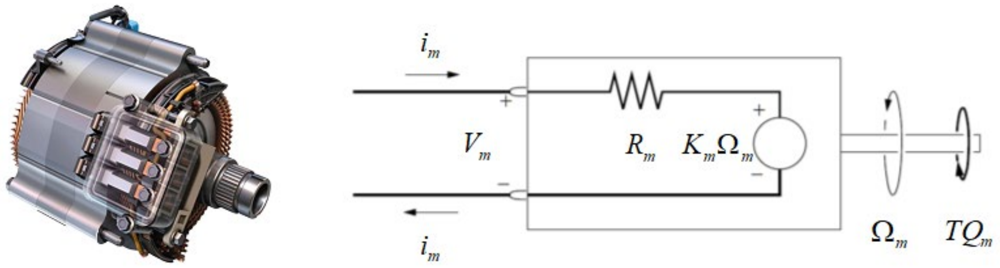

Fig. 5 Permanent magnet DC electric motor model

Figure 5 shows a basic model of the DC motor with steady-state torque and voltage relations given as

$$\begin{aligned} V_m &= R_m i_m + K_m \Omega_m \\ TQ_m &= K_m i_m \end{aligned} \tag{21-b}$$

Here, V_m is motor armature voltage, i_m is motor current, TQ_m is motor shaft torque, and Ω_m is motor shaft rotation speed. The motor parameters are the torque constant, K_m, and armature resistance R_m. It is also common to define the motor speed constant

$$K_{v,m} = \frac{1}{K_m} \tag{22}$$

which is typically reported in units of RPM/V. Following Johnson,[11] the motor mass is estimated based on the maximum design torque $TQ_{m,\max}$ as

$$m_m = 0.137(TQ_{m,\max})^{0.8587} \qquad \text{Units}: TQ_{m,\max}\ \{\text{Nm}\},\ m_m\ \{\text{kg}\} \tag{23}$$

Furthermore, following Gur and Rosen,[12] $K_{v,m}$ is empirically estimated based on m_m as

$$K_{v,m} = \frac{B_K}{m_m} \qquad \text{Units}: K_{v,m}\left\{\frac{\text{RPM}}{\text{V}}\right\},\ m_m\ \{\text{kg}\} \tag{24-a}$$

Where fitting coefficient, B_K, for high-performance motors falls into the range

$$50\left\{\frac{\text{RPM kg}}{\text{V}}\right\} < B_K < 600\left\{\frac{\text{RPM kg}}{\text{V}}\right\} \tag{24-b}$$

Specifically, $B_K = 170\left\{\frac{\text{RPM kg}}{\text{V}}\right\}$ was selected and used in the present study. Next, further following Gur and Rosen,[12] R_m is empirically estimated using

$$R_m = \frac{B_R}{K_{v,m}^{\ 2}} \qquad \text{Units}: K_{v,m}\left\{\frac{\text{RPM}}{\text{V}}\right\},\ R_m\ \{\Omega\} \tag{25-a}$$

Where fitting coefficient, B_R, for high-performance motors falls into the range

$$2{,}500\left\{\frac{\text{V}^2\,\Omega}{\text{RPM}^2}\right\} < B_R < 1{,}000{,}000\left\{\frac{\text{V}^2\,\Omega}{\text{RPM}^2}\right\} \tag{25-b}$$

Here, the value $B_R = 60{,}000\left\{\frac{\text{V}^2\,\Omega}{\text{RPM}^2}\right\}$ was used in the present study. In addition, the motor input power, $P_{m,in}$, and output power, $P_{m,out}$, are computed as

$$P_{m,in} = V_m i_m \quad \text{and} \quad P_{m,out} = TQ_m \Omega_m \tag{26}$$

Which, after applying Eq. 21, gives the relation

$$P_{m,out} = P_{m,in} - R_m i_m^{\ 2} \tag{27}$$

Finally, motor efficiency is computed as

$$\eta_m = \frac{P_{m,out}}{P_{m,in}} \tag{28}$$

2.1.5 Single-Stage Motor/Rotor Gearbox Sizing

As shown in Fig. 6, the battery-electric configuration includes the possibility of a single-stage gear reduction gearbox between the motor and rotor to improve impedance matching.

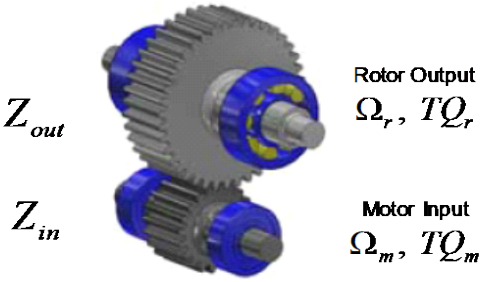

Fig. 6 Single-stage gear reduction

As a result of the gearbox, the rotation speeds Ω_r and Ω_m obey the following kinematic relation

$$\Omega_r = n_{gb}\Omega_m \quad \text{with} \quad n_{gb} = \frac{Z_{in}}{Z_{out}} \tag{29}$$

Where n_{gb} is the gear ratio computed from the number of gear teeth, Z_{in} and Z_{out}, on the input and output sides, respectively. Furthermore, the torques TQ_r and TQ_m are related by

$$TQ_r = \eta_{gb} \frac{TQ_m}{n_{gb}} \tag{30}$$

Where η_{gb} is the gearbox efficiency. Furthermore, the relationship between motor output power $P_{m,out}$ and rotor power P_r,

$$P_r = \eta_{gb} P_{m,out} \tag{31}$$

Finally, following a similar method described by Rejman and Rejman,[13] the gearbox mass is estimated based on maximum allowable spur gear tooth contact stress, σ_c, with American Gear Manufacturing Association (AGMA) design safety factors (overload factor, K_o=1.5; load distribution factor, K_l=1.6; size factor, K_s=1.0; dynamic factor, K_d=1.3; and surface condition factor, C_f=1.0.)

$$\sigma_c = C_p \sqrt{\frac{F_t}{2R_p b}\frac{K_o K_s K_d K_l C_f}{I}} \qquad \text{with} \qquad F_t = \frac{TQ_m}{R_p} \tag{32}$$

where F_t is the tangential tooth load, R_p is pinion gear pitch radius, b is gear facewidth (see Fig. 7), I is the external spur gear geometry factor which is a function tooth pressure angle $\phi = 20°$

$$I = \frac{\cos\phi \sin\phi}{2}\frac{1}{1+n_{gb}} \tag{33}$$

and C_p is the Hertzian contact stress coefficient,

$$C_p = \sqrt{\frac{E}{2\pi(1-\nu^2)}} \tag{34}$$

where E and ν are gear material elastic modulus and Poisson's ratio, respectively.

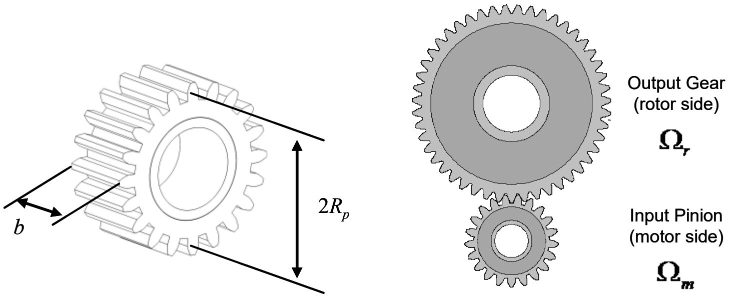

Fig. 7 Pinion gear facewidth and pitch diameter

The design condition is

$$\sigma_c = \bar{s}_{fc} \tag{35}$$

where $\bar{s}_{fc}$ is the modified contact strength

$$\bar{s}_{fc} = \frac{Z_N C_H}{K_T K_R} s_{fc} \tag{36}$$

which is computed in terms of the material contact strength, $s_{fc} = 125{,}000 \text{ psi}$, and AGMA strength modifiers (stress cycle factor, Z_N = 1.0; temperature factor,

K_T = 1.0; reliability factor, K_R = 1.0; hardness ratio factor for pitting resistance, C_H = 1.0). After combining Eqs. 32–36 the mass of the gear pair is computed as

$$m_{gb} = \rho_g \pi \frac{C_p^{\,2}}{\bar{s}_{fc}^{\,2} \cos\phi \sin\phi} K_o K_d K_s K_l C_f \left(1 + n_{gb}\right)\left(1 + \frac{1}{n_{gb}^{\,2}}\right) T Q_m \qquad \text{for } n_{gb} \neq 1$$

$$m_{gb} = 0 \qquad \text{for } n_{gb} = 1 \tag{37}$$

where ρ_g is the gear material density. Here, for the special case of n_{gb} = 1 (direct drive) there is no gearbox required so the code reverts to m_{gb} = 0.

2.1.6 Electric Battery Model

The electric battery is modeled based on the schematic in Fig. 8, which considers N_p parallel banks of N_s cells connected in series for a total of $N_c = N_p N_s$ cells.

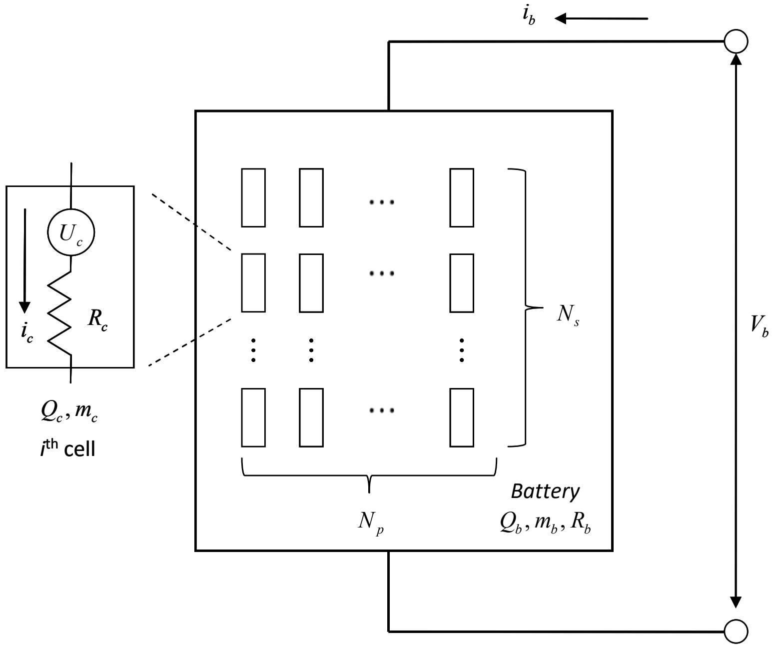

Fig. 8 Multiple cell electric battery model schematic

The battery cells are assumed to be based on currently available lithium polymer (Li-Po) technology. Each cell is characterized as having an inherent cell voltage U_c = 3.7 V, cell resistance $R_c = 6.0 \times 10^{-3}\Omega$, cell charge capacity Q_c = 2,200 mAh, and cell mass m_c = 63.33 g. Based on this, the combined battery properties are

$$U_b = N_s U_c\,, \quad Q_b = N_p Q_c\,, \quad R_b = \frac{N_s}{N_p} R_c\,, \quad \text{and} \quad m_b = N_c m_c \tag{38}$$

where U_b, Q_b, R_b, and m_b are battery voltage, charge capacity, electrical resistance and mass, respectively. Furthermore, the total energy stored in the battery is

$$E_b = Q_b U_b \tag{39}$$

and the battery terminal voltage is

$$V_b = U_b - R_b i_b \tag{40}$$

where i_b is battery current, which is computed in terms of electrical power supplied to the load P_b

$$i_b = \frac{U_b}{2R_b} - \sqrt{\frac{1}{R_b}\left(\frac{U_b^{\ 2}}{4R_b} - P_b\right)} \tag{41}$$

From this, the maximum theoretical battery power output is

$$P_{b\max} = \frac{U_b^{\ 2}}{4R_b} \tag{42}$$

Also, assuming constant power draw, P_b, from the battery, the battery discharge time t_d, is

$$t_d = \frac{Q_b}{i_b} = \frac{N_p Q_c}{\dfrac{N_p U_c}{2R_c} \pm \sqrt{\left(\dfrac{N_p^{\ 2} U_c^{\ 2}}{4R_c^{\ 2}} - \dfrac{N_p}{N_s R_c} P_b\right)}} \tag{43}$$

and the total energy delivered to the load is

$$E_{load} = P_b t_d \tag{44}$$

Using Eqs. 43 and 44, the battery Ragone curve is generated by plotting the E_{load} versus P_b as shown in Fig. 9. Furthermore, considering Eqs. 38–44, the minimum required battery mass, m_b, of a battery capable of delivering a specified power output, P_b, over specified discharge time, t_d, is

$$m_b(P_b, t_d) = \frac{m_c P_b t_d^{\ 2}}{Q_c (U_c t_d - Q_c R_c)} \tag{45}$$

Typically, the nominal discharge rating for a battery is based on a 1 h discharge time. The current draw for a 1 h discharge time, i_{1C}, is

$$i_{1C} = \frac{Q_b}{3600} \qquad (C_{rate} = 1) \tag{46}$$

Higher "C-rates" correspond to shorter t_d and higher P_b. The C-rate can be computed as

$$C_{rate} = \frac{t_d}{3600} \quad \text{and} \quad i_b = C_{rate}\, i_{1C} \tag{47}$$

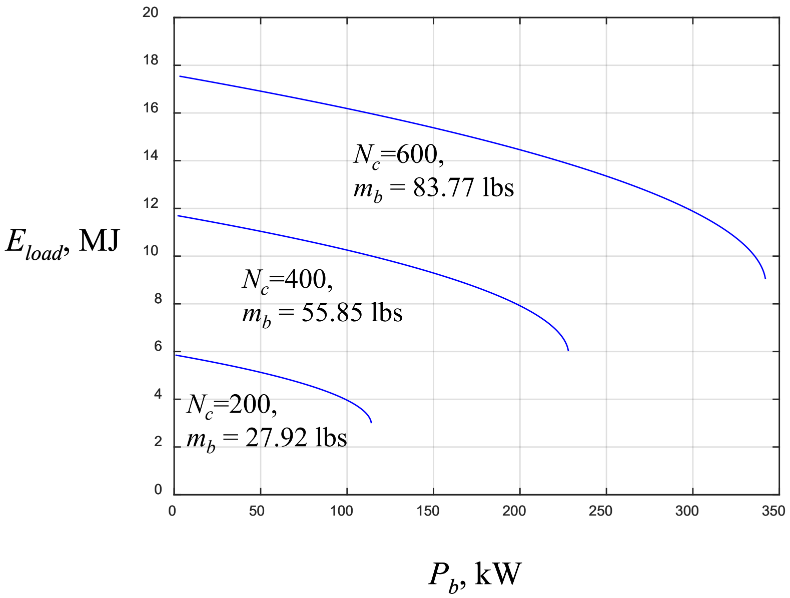

Fig. 9 Ragone plot: battery energy output vs. power output for three different size batteries

Practical battery power output, $P_b << P_{b\max}$, is restricted to much lower values compared with the theoretical maximum, $P_{b\max}$, due to thermal effects and heat dissipation requirements. In order to address this in the analysis, the maximum C_{rate} is constrained to be

$$C_{rate} < C_{rate,\max} \quad \text{with} \quad C_{rate,\max} = 10 \tag{48}$$

Here a C_{rate} = 10 corresponds to t_d = 360 s (6 min battery discharge time). The required battery output power, P_b, is determined based on the motor electronic speed controller (ESC) input power levels, which are considered in the next section.

2.1.7 ESC and Battery Sizing

The interface between the battery and the electric motors is the ESC, which distributes the battery power to each motor as depicted in Fig. 10.

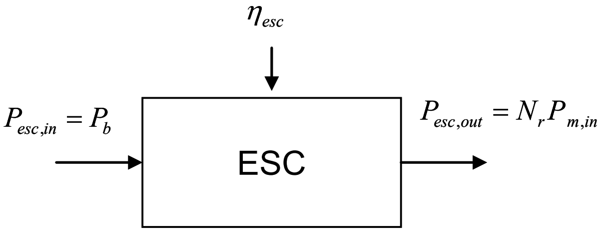

Fig. 10 Electronic speed controller with input and output power flows

The required output power from the ESC is determined from the motor input power and the number of motors as

$$P_{esc,out} = N_r P_{m,in} \tag{49}$$

Furthermore, the corresponding ESC input power is

$$P_{esc,in} = \frac{P_{esc,out}}{\eta_{esc}} \tag{50}$$

where η_{esc} is the ESC efficiency. Next, P_b, is determined from Eq. 50 as

$$P_b = P_{esc,in} \tag{51-a}$$

Utilizing Eqs. 21, 26–31, 49, 50, and 51, the steady-state battery power demand is

$$P_b = \frac{N_r}{\eta_{esc}} \left(\frac{P_r}{\eta_{gb}} + \left(\frac{n_{gb}}{\eta_{gb}} \right)^2 TQ_r^{\,2} \frac{R_m}{K_m^{\,2}} \right) \tag{51-b}$$

Finally, the ESC mass is estimated based on the following empirical relation given in Bershadsky et al.[10]

$$m_{esc} = 0.052 * P_{esc,out} + 5.747 \qquad \text{Units: } m_{esc}\{\text{g}\},\ \ P_{esc,out}\,\{\text{W}\} \tag{52}$$

2.1.8 Battery-Electric UAV Structural Mass Estimation

The remaining major system mass contribution to be included in the sizing analysis is the vehicle structural mass m_s. In the case of the battery-electric VTOL UAV considered in this study, m_s is estimated as

$$m_s = f_{sm}((m_r + m_{gb} + m_m)N_r + m_{esc} + m_p + m_b) \tag{53}$$

Where f_{sm} is defined as the structural mass fraction. This study considers different values of f_{sm} ranging from f_{sm} = [0.25 to 1.0] as a measure of overall structural efficiency.

2.2 Battery-Electric Configuration Design Results

This section shows the design and performance results obtained by applying the sizing and design code outlined in Fig. 3 and described in Section 2.1 for the medium-scale battery-electric VTOL UAV configuration shown in Fig. 2. Table 2 gives the system parameters used in the design study and analysis.

Table 2 Fixed design parameters for medium-scale battery-electric multirotor VTOL UAV

Parameter	**Value**	**Parameter**	**Value**
Acceleration of gravity, g	9.81 m/s^2	Gear ratio, n_{gb}	[$0.2 < n_{gb} < 1.0$]
Air density, ρ	1.225 kg/m^3	Gear efficiency, η_{gb}	0.97
		Gear pressure angle, ϕ	20°
Number of rotors, N_r	[4, 6 or 8]	Gear material:	
Number of blades per rotor, N_b	4	Density, ρ_g	7870 kg/m^3
Blade lift coefficient slope, a_L	5.7	Elastic modulus, E	200 GPa
Blade drag coefficient, C_{d0}	0.008	Poisson's ratio, ν	0.29
Rotor solidity ratio, σ	0.12	Contact strength, s_{fc}	125,000 psi
Blade pitch at 3/4 span, θ_{75}	10°		
Blade tip speed at hover, $v_{t,h}$	550 ft/s		
		Li-Po battery cell:	
		Voltage, U_c	3.7 V
Motor current constraint, $i_{m,\max}$	400 A	Resistance, R_c	$6.0 \times 10^{-3}\,\Omega$
ESC efficiency, η_{esc}	0.85	Charge capacity, Q_c	2200 mAh
		Mass per cell, m_c	63.33 g
Structural mass fraction, f_{sm}	0.25		

To begin the study, the sizing code is used to generate a family of designs over a range of battery weights, W_b, for different maximum payload weights, W_p.

$$W_b = m_b g \quad \text{and} \quad W_p = m_p g \tag{54}$$

Figures 11 and 12 show the hover endurance and maximum range results for the pure electric quadrotor (N_r=4) configuration with n_{gb}=1 (direct drive, no gearbox) for four different maximum design payloads W_p = [100, 200, 300, and 400] lb. Here, each point on the figures represents a unique design.

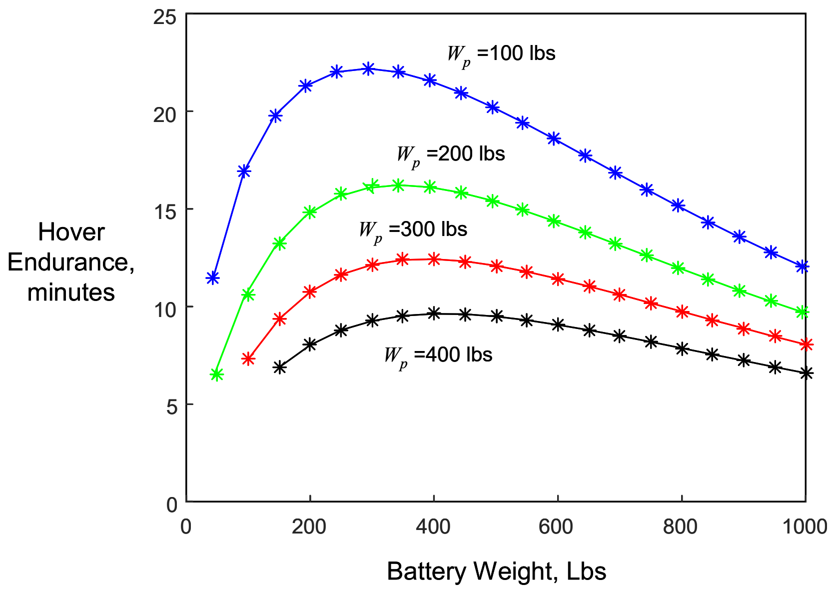

Fig. 11 **Battery-electric quadrotor UAV hover endurance vs. battery mass for four different design payloads W_p = [100, 200, 300, and 400] lb, N_r = 4, n_{gb} = 1:1 (direct drive, no gearbox)**

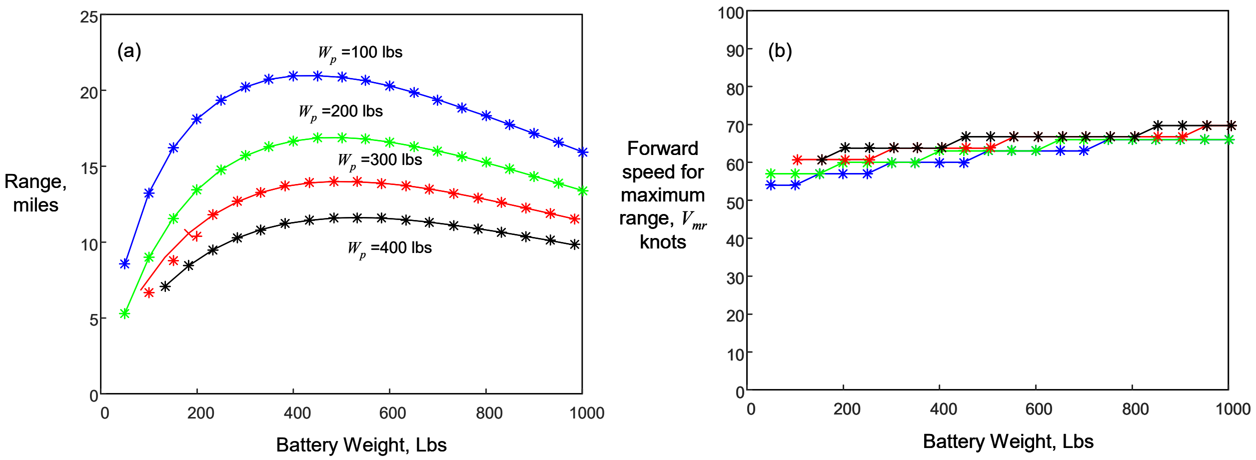

Fig. 12 **Battery-electric quadrotor UAV; a) maximum range and b) forward speed for max range vs. battery mass; W_p = [100, 200, 300, and 400] lbs, N_r = 4, n_{gb} = 1:1 (direct drive, no gearbox)**

Furthermore, Fig. 13 shows the individual component weights in the direct drive designs (for the W_p = 200 lb payload design cases).

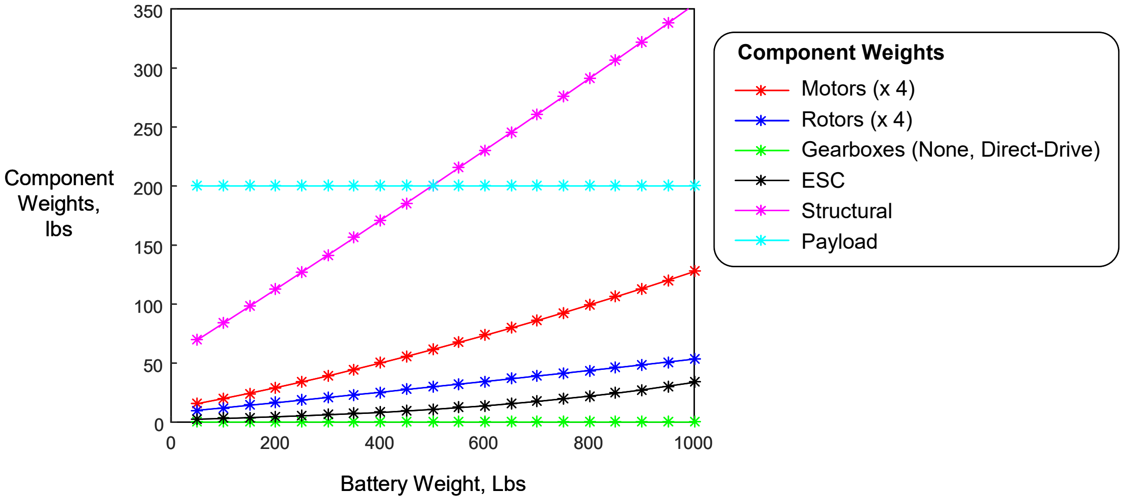

Fig. 13 **Battery-electric quadrotor UAV component weights vs. battery mass; W_p = 200 lb, N_r = 4, n_{gb} = 1:1 (direct drive, no gearbox)**

Here, from Figs. 11 and 12, it is clearly observed that there is an optimum battery mass value that maximizes either the hover endurance or the range. These results match well with conclusions from prior studies on battery-electric VTOL aircraft.[10, 12] Note, these prior studies only considered the case of direct drive.

Next, the effects of motor/rotor gearbox reduction ratio, n_{gb}, on the medium-scale pure electric quadrotor UAV design and performance is explored.

Figures 14 and 15 show the hover endurance and maximum range for the case with a 5:1 reduction (n_{gb} = 0.2) from the motor to the rotor for two different design payloads W_p = [100 and 400] lb. For reference, the direct drive (n_{gb} = 1:1) design results for the same payload levels are also plotted on the graphs.

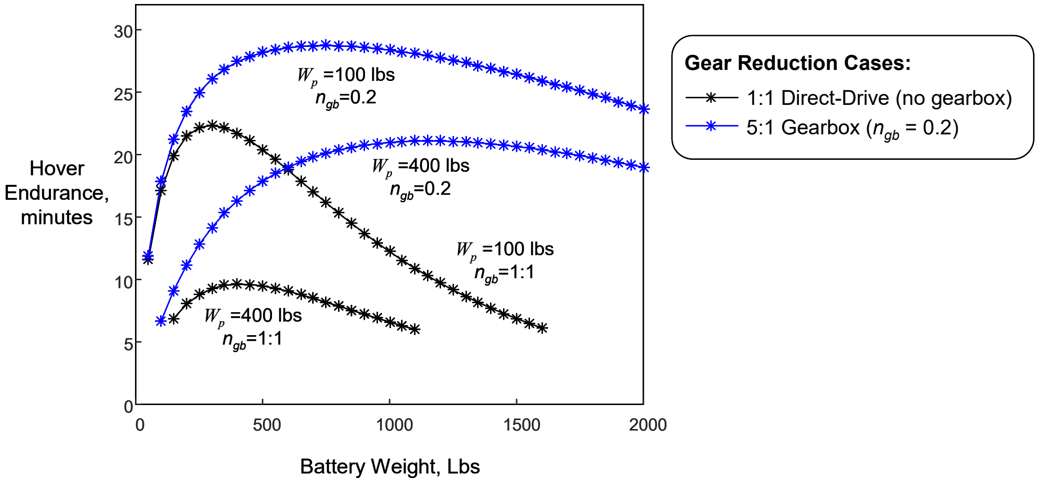

Fig. 14 **Battery-electric quadrotor UAV hover endurance vs. battery mass with and without gear reduction; N_r = 4, W_p = [100 and 400] lb**

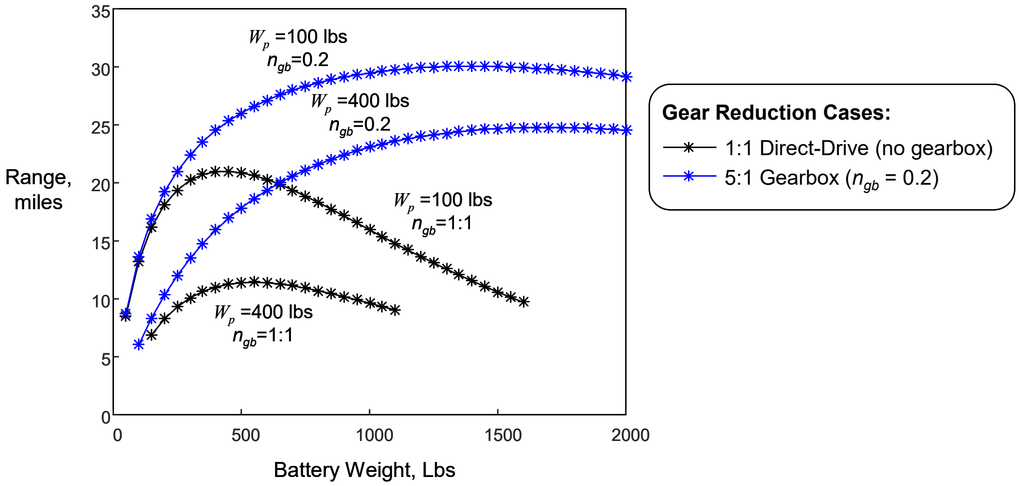

Fig. 15 Battery-electric quadrotor UAV maximum range vs. battery mass with and without gear reduction; N_r = 4, W_p = [100 and 400] lb

Furthermore, Fig. 16 shows the individual component weights of the designs that include the motor/rotor gearbox (for the W_p = 200 lb payload design cases).

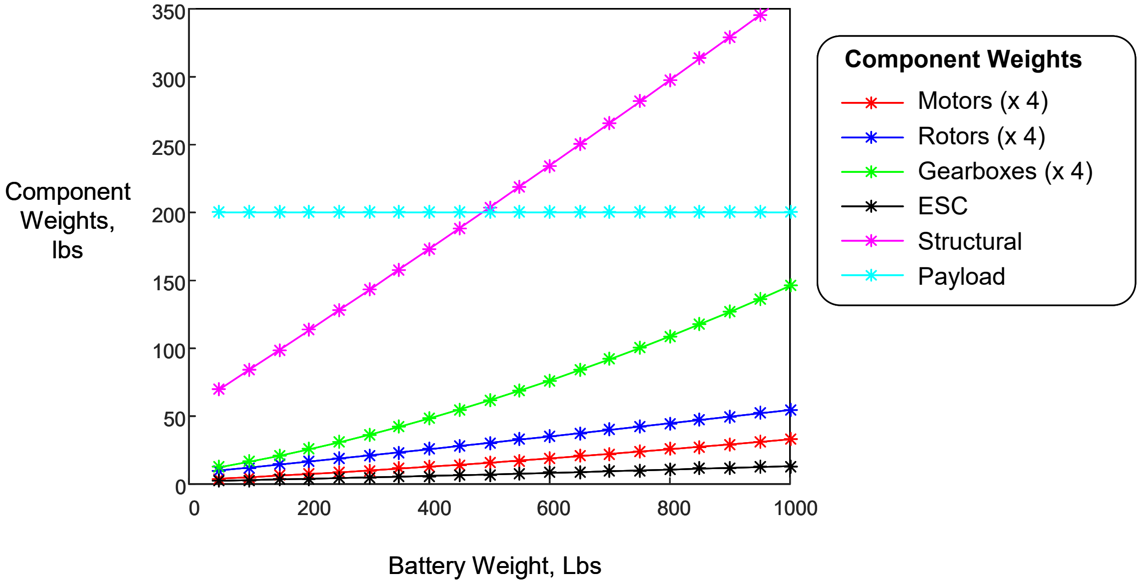

Fig. 16 Battery-electric quadrotor UAV component weights vs. battery mass; W_p = 200 lb, N_r = 4, n_{gb} = 0.2 (5:1 reduction)

As seen in Fig. 16, the weight contribution of the gearboxes is larger than the weight of both the rotors and motors. However, as seen in Figs. 14 and 15, the overall system performance improvements more than compensates for the added weight penalty. Specifically, for a given battery size, the results show that both maximum possible range and hover endurance are significantly improved through the use of a gear reduction stage between the motors and rotors. Additionally, the gear reduction also enables a heavier battery to be utilized, resulting in even further improved range and hover endurance.

To further examine effects of the gearbox on battery-electric quadrotor performance, the design code was used to generate a set of designs over a range of gear ratios, n_{gb}. Specifically, the hover endurance and maximum range results for these designs are shown in Figs. 17 and 18. As seen in these figures, there is an optimum gear ratio that maximizes both range and hover endurance for a given maximum design payload. The optimum gear ratios are summarized in Table 3.

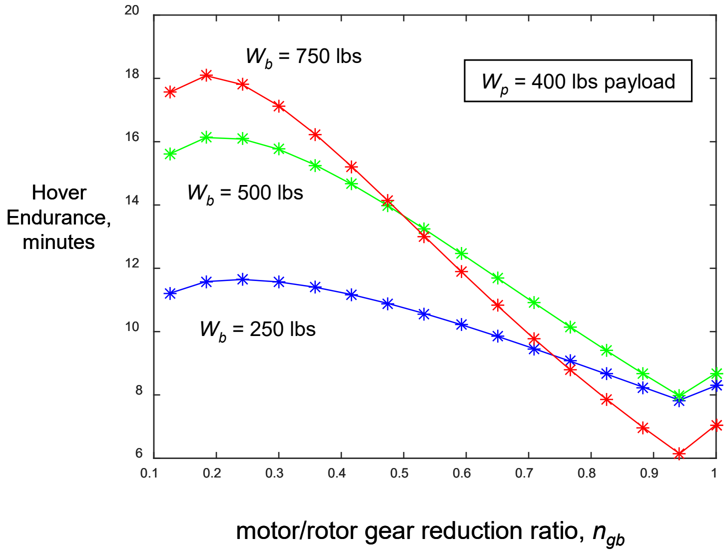

Fig. 17 Battery-electric quadrotor UAV hover endurance vs. motor/rotor gear ratio for several size batteries; W_b = [250, 500, and 750] lb with W_p = 400 lb, N_r = 4

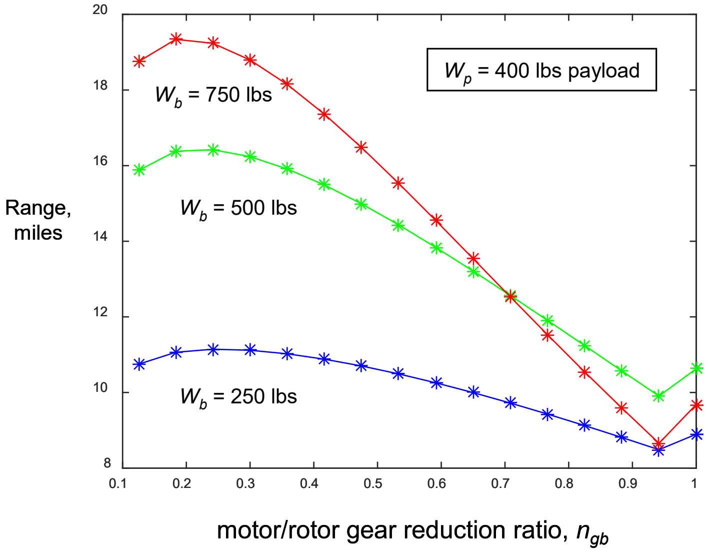

Fig. 18 Battery-electric quadrotor UAV maximum range vs. motor/rotor gear ratio for several size batteries; W_b = [250, 500, and 750] lb with W_p = 400 lb, N_r = 4

Table 3 Optimum gear ratios for battery-electric quadrotor UAV

Design payload	Gear ratio to maximize hover endurance	Gear ratio to maximize range
$W_p = 250$ lb	$n_{gb} = 0.19$	$n_{gb} = 0.19$
$W_p = 500$ lb	$n_{gb} = 0.23$	$n_{gb} = 0.23$
$W_p = 750$ lb	$n_{gb} = 0.24$	$n_{gb} = 0.24$

Figures 19 and 20 show the forward flight performance results as a function of vehicle forward speed, v_v, for a particular battery-electric quadrotor design with direct drive.

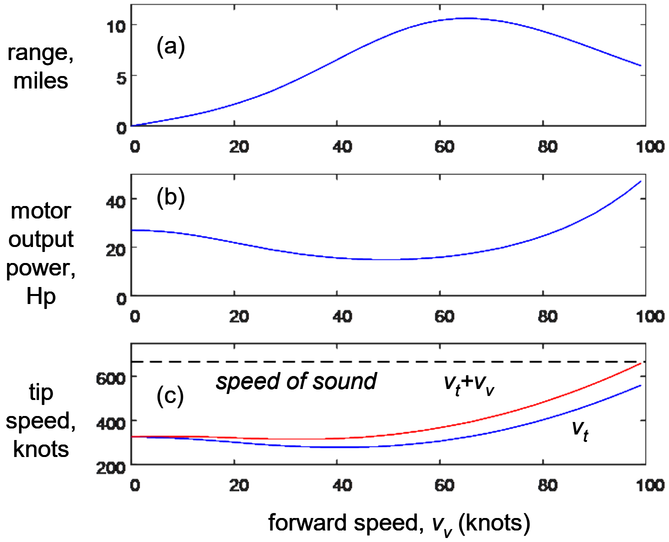

Fig. 19 **Battery-electric quadrotor UAV forward flight performance vs. forward speed; n_{gb} = 1:1 (direct drive), battery W_b = 500 lb, payload W_p = 400 lb, N_r = 4**

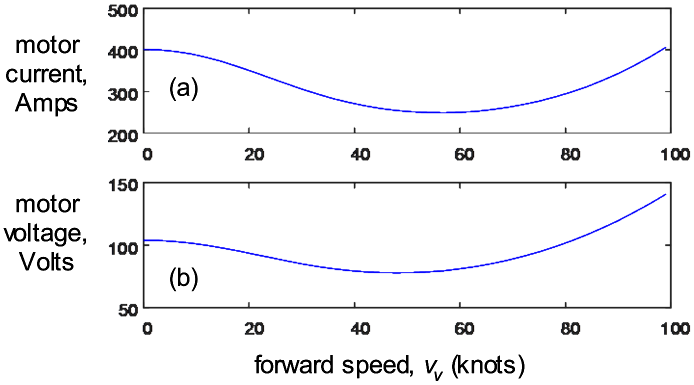

Fig. 20 **Battery-electric quadrotor UAV motor current and motor voltage in flight; n_{gb} = 1:1 (direct drive), W_b = 500 lb, W_p = 400 lb, N_r = 4**

Finally, Figs. 21 and 22 show the forward flight performance results as a function of vehicle forward speed, v_v, for a particular battery-electric quadrotor design with gear ratio $n_{gb} = 0.2$.

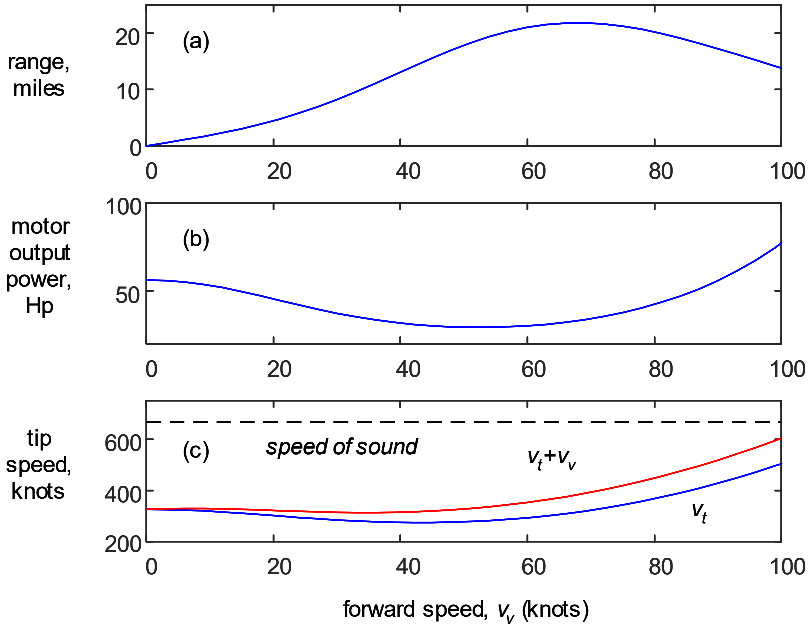

Fig. 21 **Battery-electric quadrotor UAV forward-flight performance vs. forward speed; $n_{gb} = 0.2$ (5:1 reduction), battery $W_b = 1250$ lb, payload $W_p = 400$ lb, $N_r = 4$**

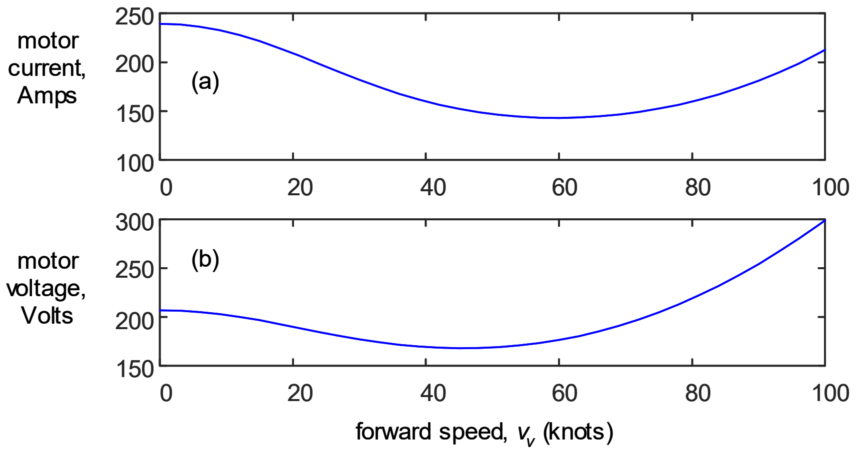

Fig. 22 **Battery-electric quadrotor UAV motor current and motor voltage in flight; $n_{gb} = 0.2$ (5:1 reduction), $W_b = 1250$ lb, $W_p = 400$ lb, $N_r = 4$**

Figures 19c and 21c show how rotor blade tip speed, v_t, varies with v_v as dictated by the variable rotor RPM control trim solution. By comparing Figs. 20 and 22, it is observed that one effect of the gear reduction on the design is that it reduces motor currents and increases motor operating voltages. Since copper losses are related to $R_m i_m^2$, reduction in i_m allows more efficient motor operation.

3. Internal Combustion Engine Powered Configuration

The design and analysis of the system is conducted based on the assumption of quasi-steady operation. Figure 23 shows a schematic of the internal combustion (IC) engine-powered quadrotor UAV considered in this section.

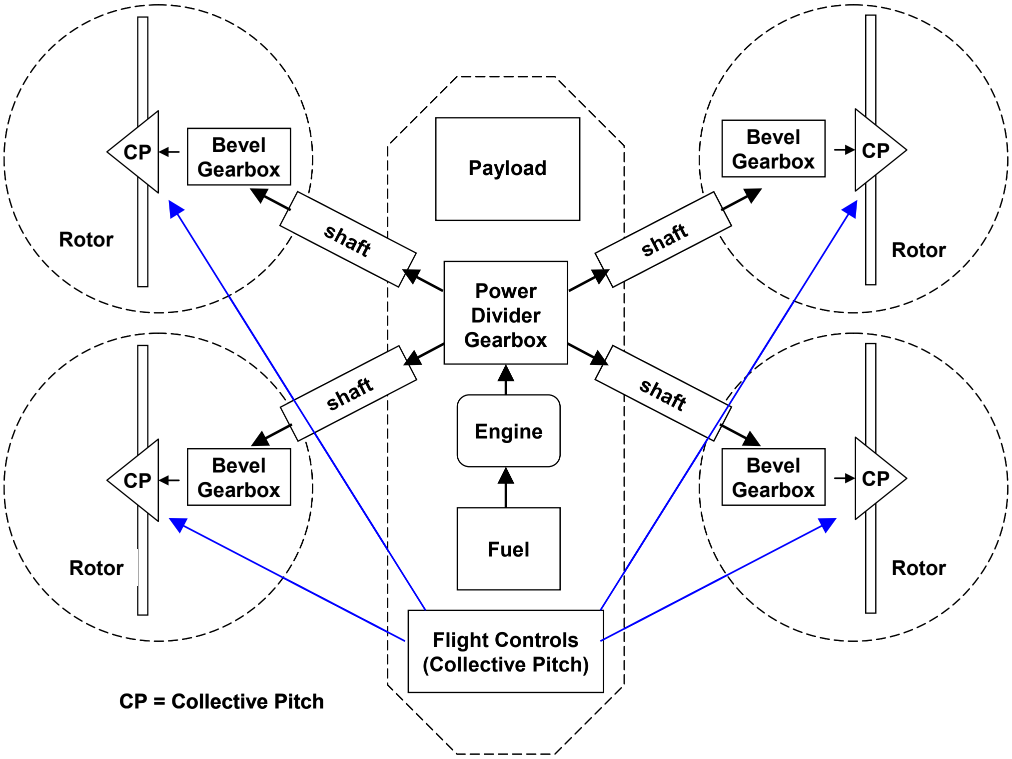

Fig. 23 IC engine-powered quadrotor UAV with multistage transmission and blade collective pitch flight control

This pure mechanical configuration (Fig. 23) is based on a centralized four-stroke piston engine with a power-dividing gearbox, multiple drive shafts, and a final gear reduction stage at the rotor. The system is designed to operate around a fixed rotational speed with blade collective pitch flight controls. An iterative sizing algorithm and design code is developed and utilized to obtain a family of feasible designs. The hover and forward flight performance of these designs is then evaluated for a variety of payloads and forward flight speeds.

3.1 Modeling and Design of IC Engine-Powered Configuration

The flowchart of the sizing algorithm developed under this project for the gas-powered IC engine quadrotor UAV configuration is shown in Fig. 24. To evaluate the hover and forward flight performance, the total gross weight of the vehicle must be computed. The total mass, m, and empty mass, m_{empty}, are

$$\begin{aligned} m_{empty} &= m_r N_r + m_{gb} + m_e + m_{ft} + m_s \\ m &= m_{empty} + m_p + m_{f,0} \end{aligned} \tag{55}$$

Where m_{empty} is composed of the rotor mass, m_r, total gearbox mass, m_{gb}, IC engine mass, m_e, fuel tank mass, m_{ft}, and the vehicle structural mass m_s. Here, m_{gb}, represents the combined mass of all the gearboxes in the multistage transmission system (see Fig. 23).

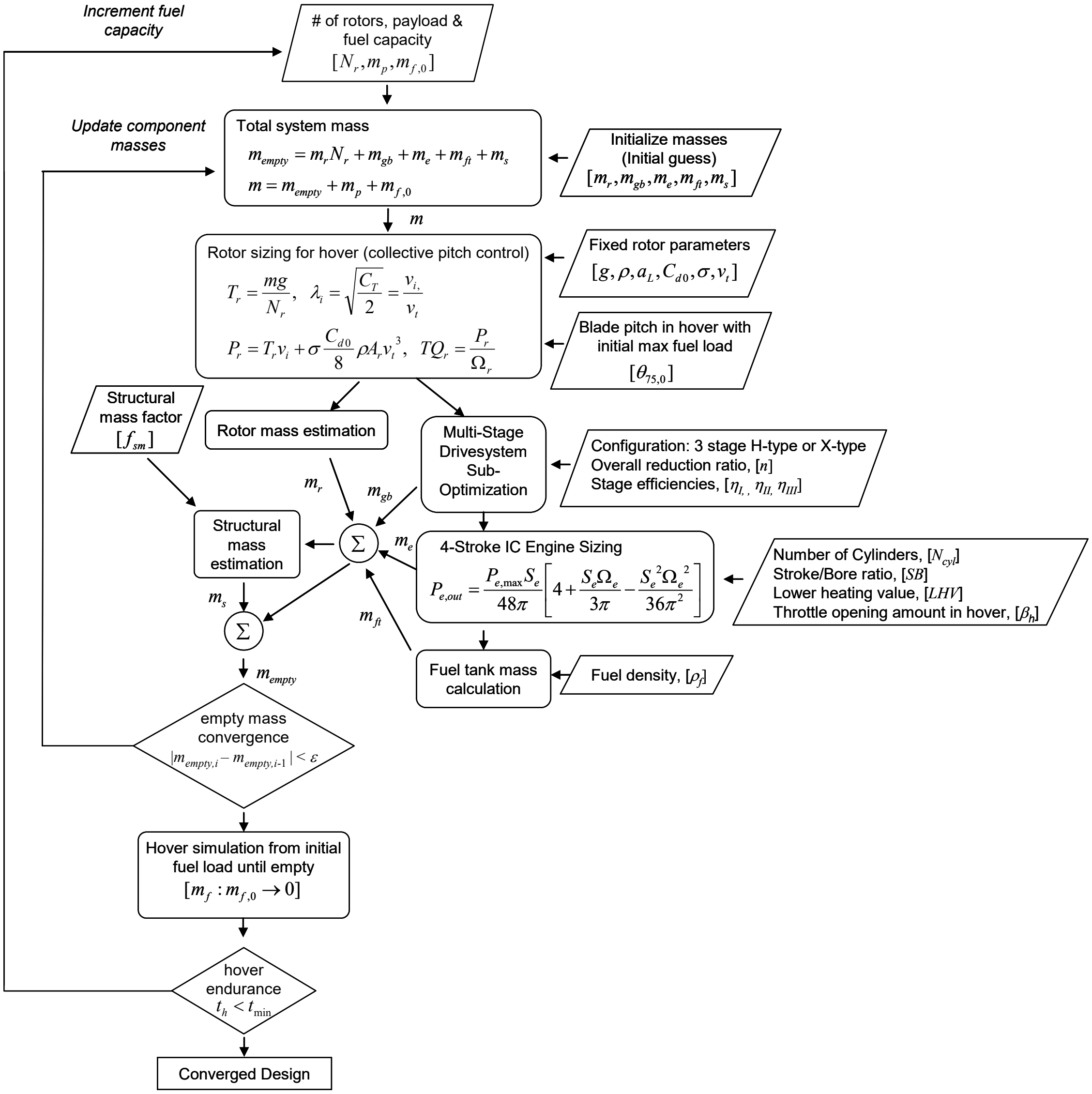

Fig. 24 Iterative sizing algorithm for design of the multirotor VTOL UAV with IC piston-engine propulsion and blade collective pitch flight control

As before, in order to size the system components, an iterative design code is developed that determines the size of each component based on power and energy requirements during hover for a given maximum initial fuel load, $m_{f,0}$, and payload mass, m_p. Starting with initialized mass estimates for each component, the required rotor thrust, T_r, and rotor power, P_r, is computed. These results are then propagated down the drivesystem where each subsequent component is sized based on the required rotational speed and power levels. The updated component masses from the i^{th} iteration step are then used to generate a new estimate, $m_{empty,i}$, which is compared with the prior estimate, $m_{empty,i-1}$, to evaluate convergence (see Fig. 24).

The details of each component model and sizing equations are described in the subsections following.

3.1.1 Hover and Forward-Flight Aeromechanics Model

Please refer to Section 2.1.1, since the hover and forward-flight aeromechanics models are identical for the battery-electric and IC engine-powered quadrotor cases.

3.1.2 Collective Blade Pitch Trim Solution in Forward Flight

In this study, the flight control method for the IC engine-powered quadrotor UAV is considered to be based on articulated rotors with collective blade pitch control. The rotors are assumed to operate at a constant specified design blade tip speed v_t. For given blade parameters [a_L, σ] and given flight condition [v_v, v_i, α], the trim solution is obtained by equating the C_T expressions, Eqs. 10 and 11, and then solving for the required blade collective pitch angle, θ_{75}, from the roots of resulting polynomial

$$b_2 \theta_{75}{}^2 + b_1 \theta_{75} + b_0 = 0 \tag{56-a}$$

Which has coefficients

$$\begin{aligned} b_2 &= a_L{}^2 \sigma^2 \left(\frac{1}{9} + \frac{\mu^2}{3} + \frac{\mu^4}{4} \right) \\ b_1 &= -a_L{}^2 \sigma^2 \lambda_i \left(\frac{1}{3} + \frac{\mu^2}{2} \right) \\ b_0 &= -16 \lambda_i{}^2 \left(\lambda_i^2 + \mu^2 + 2\lambda_i \mu \tan\alpha + \mu^2 \tan^2\alpha - \frac{a_L{}^2 \sigma^2}{32} \right) \end{aligned} \tag{56-b}$$

After computing the two roots of Eq. 56, the code considers θ_{75} to be the lowest positive valued root as the physical solution.

3.1.3 Rotor Sizing Based on Hover Condition

To determine the required rotor disk area, A_r, the rotor is sized about the hover condition ($v_v = 0$) for a specified rotor tip speed, v_t and a specified blade collective pitch setting during hover as θ_{75}=$\theta_{75,h}$. Please refer to Section 2.1.3, since the rotor sizing process for the battery-electric and IC engine-powered quadrotor cases is otherwise identical.

3.1.4 Internal Combustion Piston Engine Model

The IC piston engine model used in this study is based on the so-called polynomial engine model approach.[14]

The basic starting point is the assumption of a non-dimensional brake mean effective cylinder pressure (BMEP), $\bar{p}_{cyl}$, curve at wide open throttle (WOT) of the form (see Fig. 25).

$$\bar{p}_{cyl,WOT} = \frac{4}{5} + \frac{2}{5}\bar{v}_{pst} - \frac{1}{5}\bar{v}_{pst}^{\ 2} \tag{57}$$

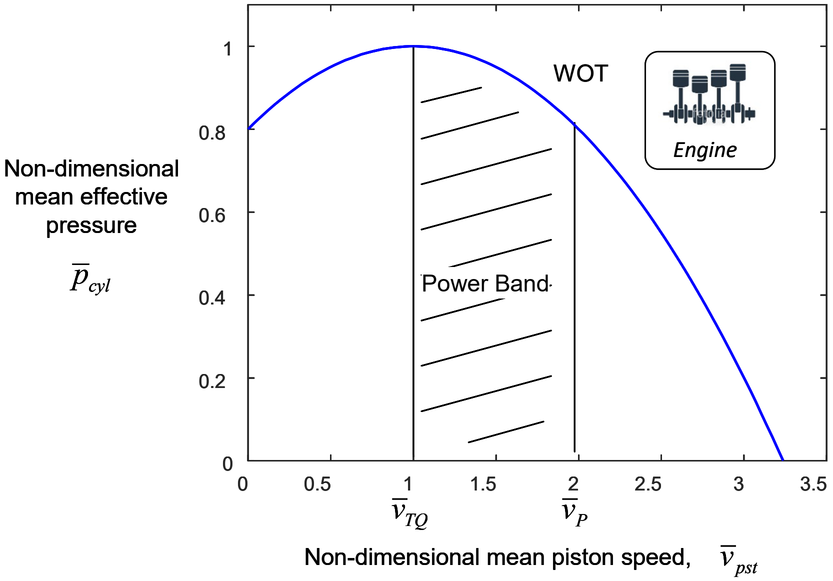

Fig. 25 Polynomial IC engine model: non-dimensional mean effective pressure vs. non-dimensional mean piston speed

Where $\bar{p}_{cyl,WOT}$ is the non-dimensional mean effective cylinder pressure at WOT and $\bar{v}_{pst}$ is non-dimension mean piston speed defined as

$$\bar{v}_{pst} = \frac{v_{pst}}{v_{TQ}} \tag{58}$$

where v_{pst} is mean piston speed and v_{TQ} is mean piston speed at which maximum engine output torque $TQ_{e,\max}$ is delivered. Furthermore, $\bar{p}_{cyl}$ is defined as

$$\bar{p}_{cyl} = \frac{p_{cyl}}{p_{cyl,\max}} \tag{59}$$

where p_{cyl} is mean effective cylinder pressure and $p_{cyl,\max}$ is maximum possible cylinder pressure, which based on Eq. 57 along with the assumption of a four-stroke cycle, is

$$p_{cyl,\max} = \frac{5P_{e,\max}S_e}{2v_{TQ}V_{disp}} \tag{60}$$

where $P_{e,\max}$ is maximum engine output power, V_{disp} is engine displacement volume, and S_e is piston stroke length, which can be expressed as

$$S_e = \left[\frac{4V_{disp}}{N_{cyl}\pi} SB^2\right]^{\frac{1}{3}} \tag{61}$$

where SB is the stroke-over-bore ratio and N_{cyl} is the number of engine cylinders. Also, engine output torque, TQ_e, and engine rotational speed, Ω_e, can be expressed as

$$TQ_e = p_{cyl}\frac{V_{disp}}{4\pi} \quad \text{and} \quad \Omega_e = v_{pst}\frac{\pi}{S_e} \tag{62}$$

and the engine output power is

$$P_e = TQ_e\Omega_e \tag{63}$$

Next, after considering Eqs. 57–62, the engine WOT torque curve is obtained as

$$TQ_{e,WOT} = \frac{P_{e,\max}S_e}{\pi^3 v_P}\left(\frac{S_e^2\Omega_e^2 - 2\pi\, S_e\Omega_e v_{TQ} - 4\pi^2 v_{TQ}^2}{v_P^2 - 2v_P v_{TQ} - 4v_{TQ}^2}\right) \tag{64}$$

where v_P is the mean piston at which $P_{e,\max}$ is delivered at WOT. Which, according to Eqs. 63 and 64 is

$$v_P = 2v_{TQ} \tag{65}$$

Finally, the engine output torque map is

$$TQ_e(\Omega_e,\beta) = \beta\, TQ_{e,WOT}\left(\Omega_e/\beta\right) \tag{66}$$

which is parameterized in terms of Ω_e and a representative throttle opening parameter β $[0 < \beta \leq 1]$ with $\beta = 1$ corresponding to WOT conditions. In particular, from Eqs. 64 and 66, the resulting engine output torque map at partial throttle is

$$TQ_e(\Omega_e,\beta) = \frac{P_{e,\max}S_e}{\pi^3 v_P}\left(\frac{\beta 4\pi^2 v_{TQ}^2 + 2\pi\, S_e\Omega_e v_{TQ} - \frac{1}{\beta}S_e^2\Omega_e^2}{4v_{TQ}^2 + 2v_P v_{TQ} - v_P^2}\right) \tag{67}$$

with $TQ_{e,\max}$ and $P_{e,\max}$ occurring at engine rotation speeds Ω_{TQ} and Ω_P, respectively

$$
\begin{aligned}
TQ_e &= TQ_{e,\max} \quad @ \quad \Omega_{TQ} = v_{TQ}\frac{\pi}{S_e} \quad \text{with} \quad \beta = 1 \quad \text{(WOT)} \\
P_e &= P_{e,\max} \quad @ \quad \Omega_P = v_P\frac{\pi}{S_e} \quad \text{with} \quad \beta = 1 \quad \text{(WOT)}
\end{aligned} \tag{68}
$$

In IC piston engines, v_{TQ} is typically found in the range [$6 \le v_{TQ} \le 8$] m/s, v_P is typically in the range [$12 \le v_P \le 16$] m/s and engine redline typically falls within the range [$18 \le v_{max} \le 20$] m/s.[14] In this investigation, the values $v_{TQ} = 6$ m/s and $v_P = 12$ m/s are used throughout the design study. In addition, the following empirical relation between $P_{e,\max}$ and V_{disp} is also assumed.[10]

$$P_{e,\max} = 86.7 * V_{disp} \qquad \text{Units: } P_{e,\max}\{\text{Hp}\},\ \ V_{disp}\ \{\text{L}\} \tag{69}$$

Which essentially equates to an engine power density of about 86 horsepower (Hp) per liter, which is somewhat conservative for aerospace applications. Furthermore, engine mass, m_e, is estimated based on the empirical relation

$$m_e = 37.53 * V_{disp} \qquad \text{Units: } m_e\ \{\text{kg}\},\ \ V_{disp}\ \{\text{L}\} \tag{70}$$

which is 37.5 kg/liter. After considering both Eqs. 69 and 70, the IC engine specific power output is about 1.05 Hp/lb. Figure 26 shows a plot of the parameterized engine map Eq. 67 for the specific engine parameters [$P_{e,\max} = 100$ Hp, $N_{cyl} = 4$, $SB = 1.0$]. Furthermore, Fig. 27 shows the corresponding engine output power map for the same parameters.

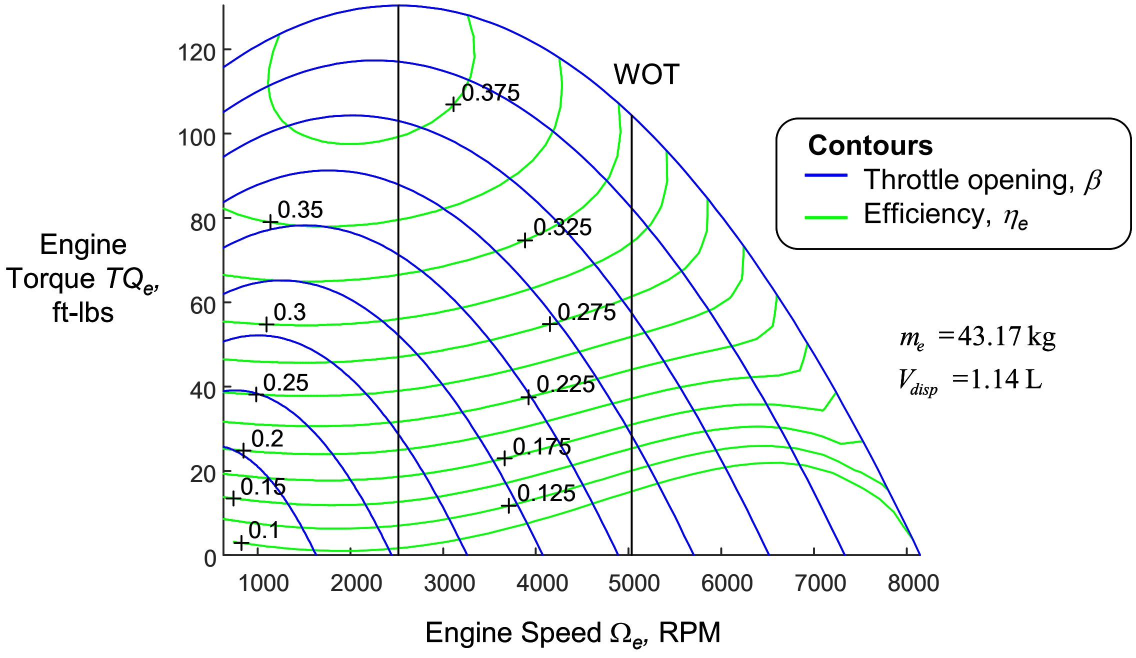

Fig. 26 Sample IC engine torque map generated from the model with specified parameters [$P_{e,\max}$ = 100 Hp, N_{cyl} = 4, SB = 1.0]

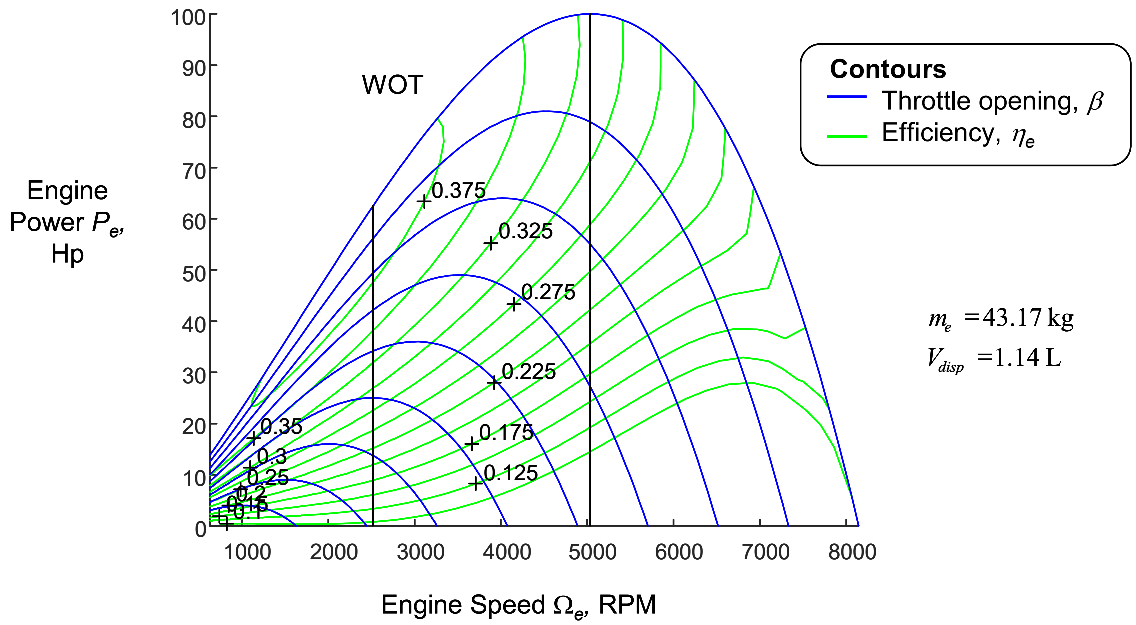

Fig. 27 Sample IC engine output power map generated from the model with specified parameters [$P_{e,\max}$ = 100 Hp, N_{cyl} = 4, SB = 1.0]

In addition to the torque and power curves plotted in blue, the engine efficiency map contours are plotted in green. The engine efficiency, η_e, used in this study is based on a typical quadratic efficiency map,[14] which is parameterized in terms of non-dimension piston speed and cylinder pressure as

$$\eta_e(\bar{v}_{pst},\bar{p}_{cyl}) = 0.08 + 0.019\bar{v}_{pst} + 0.615\bar{p}_{cyl} - 0.003\bar{v}_{pst}^{\ 2} + 0.003\bar{v}_{pst}\bar{p}_{cyl} - 0.34\bar{p}_{cyl}^{\ 2} \quad (71)$$

The engine efficiently is defined by

$$\eta_e = \frac{P_e}{P_{fuel}} \quad (72)$$

where P_e is the engine mechanical output power and P_{fuel} is the input fuel power

$$P_{fuel} = LHV\,\dot{m}_f \quad (73)$$

where LHV is the lower heating value of the fuel and $\dot{m}_f$ is the fuel mass burn rate. During the evaluation of hover endurance and maximum range the onboard fuel mass decreases based on

$$m_f = m_{f,0} - \int_0^t \dot{m}_f dt \quad (74)$$

In order to perform the engine sizing, a bisection algorithm approach based on Eqs. 67–69 is utilized (see Fig. 28). For a specified engine operating point

$[TQ_e = \overline{TQ}_e, \Omega_e = \overline{\Omega}_e, \beta = \overline{\beta}]$ with specified parameters [*SB* and N_{cyl}], the bisection algorithm returns the engine displacement, stroke length, maximum power output, and mass [V_{disp}, S_e, $P_{e,\max}$, and m_e].

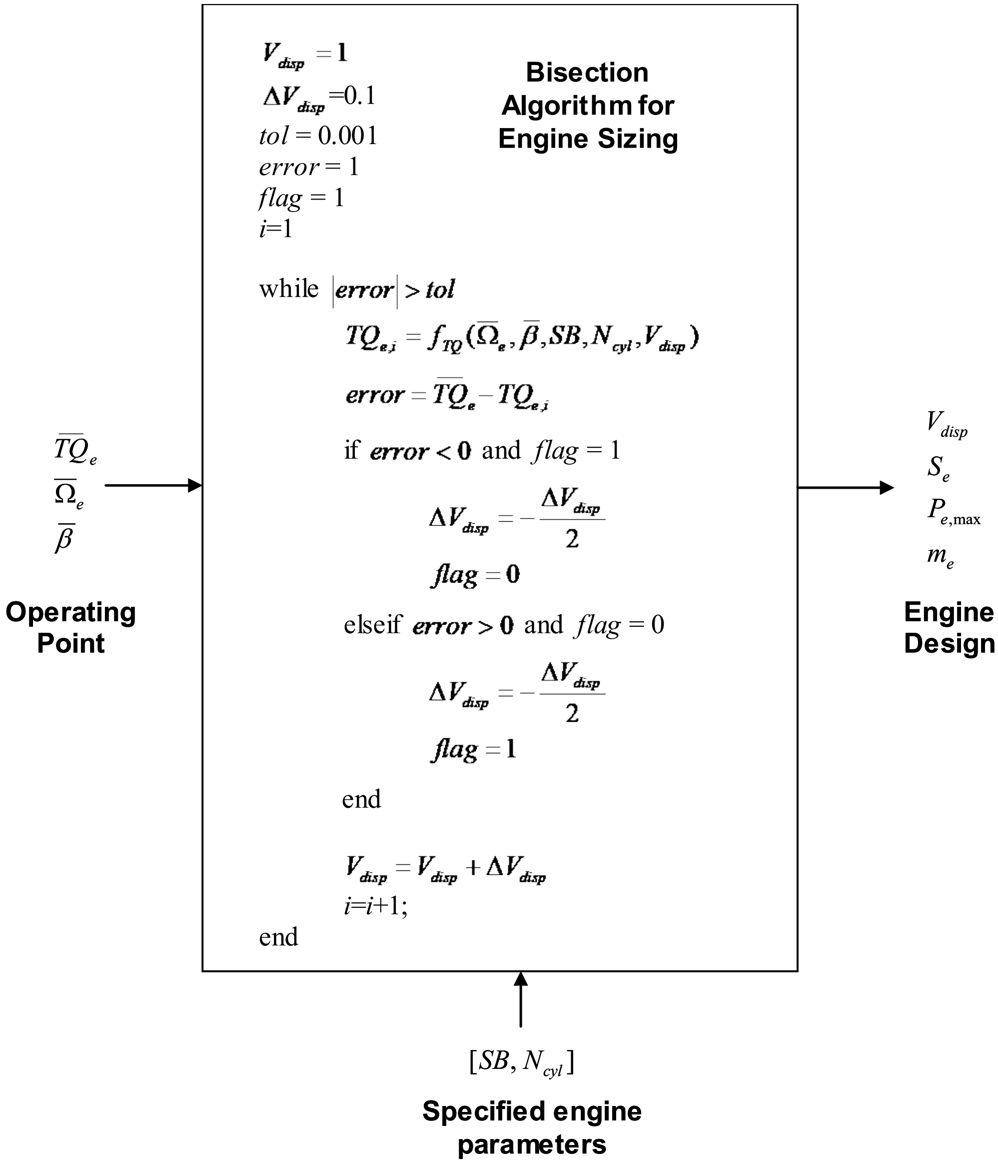

```
$V_{disp} = 1$
$\Delta V_{disp} = 0.1$
$tol = 0.001$
$error = 1$
$flag = 1$
$i = 1$

while $|error| > tol$
        $TQ_{e,i} = f_{TQ}(\overline{\Omega}_e, \overline{\beta}, SB, N_{cyl}, V_{disp})$
        $error = \overline{TQ}_e - TQ_{e,i}$
        if $error < 0$ and $flag = 1$
                $\Delta V_{disp} = -\frac{\Delta V_{disp}}{2}$
                $flag = 0$
        elseif $error > 0$ and $flag = 0$
                $\Delta V_{disp} = -\frac{\Delta V_{disp}}{2}$
                $flag = 1$
        end

        $V_{disp} = V_{disp} + \Delta V_{disp}$
        $i = i + 1;$
end
```

Fig. 28 Bisection algorithm for IC piston engine sizing for operation at specified operating point $[TQ_e = \overline{TQ}_e, \Omega_e = \overline{\Omega}_e, \beta = \overline{\beta}]$

During operation of any given IC engine design, due to the quadratic nature of the engine torque map, the trim solution of the throttle opening parameter, β, required for the engine to deliver a specified TQ_e at a specific Ω_e can be solved closed-form as

$$\beta = \frac{\pi^3 T Q_e v_P (4 v_{TQ}{}^2 + 2 v_P v_{TQ} - v_P{}^2) - 2\pi S_e{}^2 v_{TQ} \Omega_e P_{e,\max}}{8\pi^2 P_{e,\max} S_e v_{TQ}{}^2} \\ \ldots + \sqrt{\frac{S_e{}^2 \Omega_e{}^2}{4\pi^2 v_{TQ}{}^2} + \left(\frac{\pi^3 T Q_e v_P (4 v_{TQ}{}^2 + 2 v_P v_{TQ} - v_P{}^2) - 2\pi S_e{}^2 v_{TQ} \Omega_e P_{e,\max}}{8\pi^2 P_{e,\max} S_e v_{TQ}{}^2} \right)^2} \qquad (75)$$

3.1.5 Multiple Stage Transmission System Sizing and Optimization

As shown in Fig. 23, the IC engine-powered quadrotor configuration utilizes a multiple-stage transmission system to a) transmit power from the centralized engine to each of the rotors as well as b) to provide an overall speed reduction between the engine and rotors. In this study, two types of three-stage transmission system layouts are considered; the H-type shown in Fig. 29a and the X-type configuration shown in Fig. 29b.

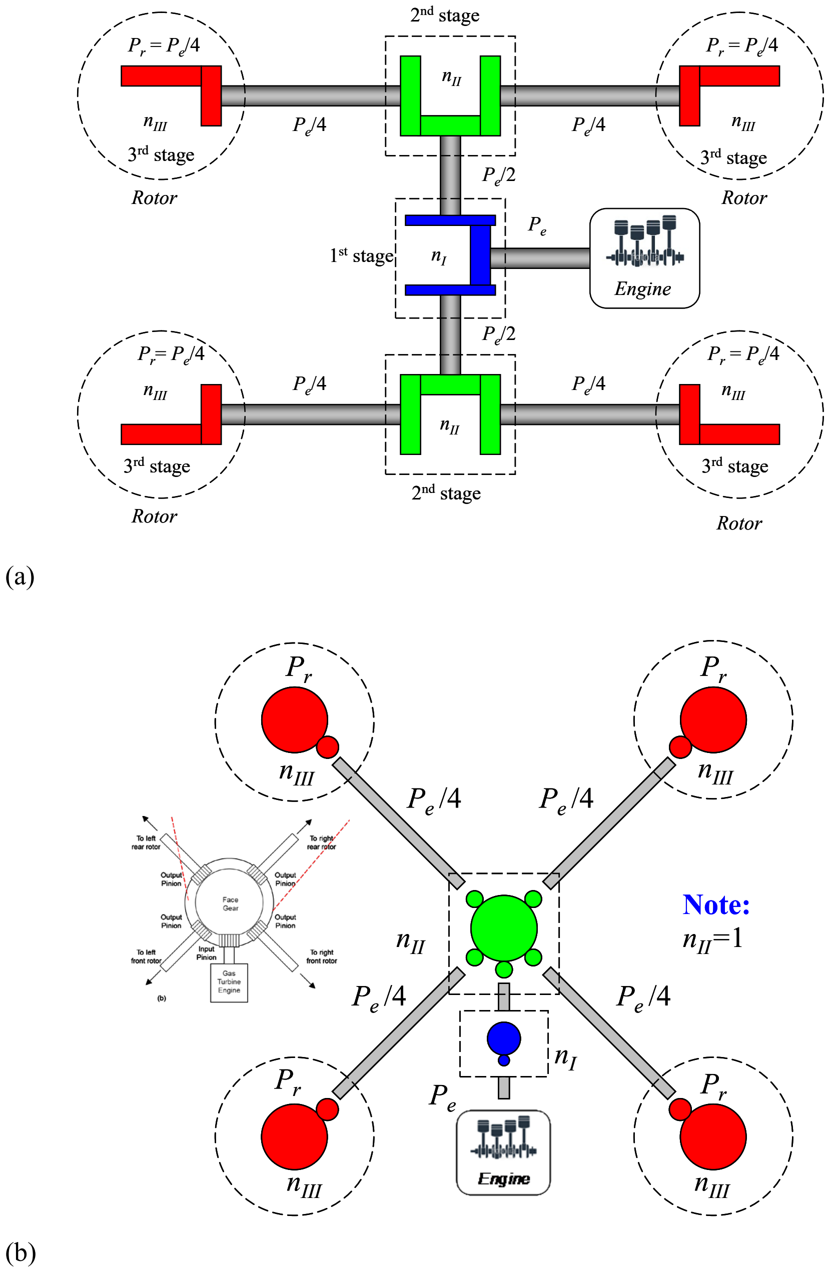

Fig. 29 Two types of three-stage transmission system layouts: a) H-type transmission layout (three gear stages I, II, and III), and b) X-type transmission layout (three gear stages I, II, and III)

In both configurations, the overall gear reduction ratio, n, between the engine and rotors is

$$n = n_I n_{II} n_{III} \quad \text{with} \quad \Omega_r = n\Omega_e \tag{76}$$

Where n_I, n_{II}, and n_{III} are the gear ratios for each gearbox stage I, II, and III of the transmission. In the case of the H-type layout, the total transmission system mass, $m_{gb,H}$, is computed as

$$m_{gb,H}(n_I, n_{II}, n_{III}) = m_{I,H} + 2m_{II,H} + 4m_{III,H} \tag{77-a}$$

with individual stage gearbox masses

$$\begin{aligned} m_{I,H} &= \rho\pi\kappa \frac{P_e}{2\Omega_e}(1+n_I)\left(1+\frac{2}{n_I^{\,2}}\right) \\ m_{II,H} &= \rho\pi\kappa \frac{P_e}{4\Omega_e}\frac{1+n_{II}}{n_I}\left(1+\frac{2}{n_{II}^{\,2}}\right) \\ m_{III,H} &= \rho\pi\kappa \frac{P_e}{4\Omega_e}\frac{1+n_{III}}{n_I n_{II}}\left(1+\frac{1}{n_{III}^{\,2}}\right) \end{aligned} \tag{77-b}$$

Here, $m_{I,H}$, $m_{II,H}$, and $m_{III,H}$ are derived based on the same method described in Section 2.1.5. The mass of each stage depends upon the input torque Eq. 37, which in this case has been expressed in terms of P_e and Ω_e. Stages I and II are power-dividing gearboxes with one input gear and two output gears while stage III is an ordinary gear stage with one input and one output gear (see Fig. 28). The resulting power input into stages I, II, and III is P_e, $P_e/2$, and $P_e/4$, respectively.

For the X-type layout, the total transmission system mass $m_{gb,X}$ is computed as

$$m_{gb,X}(n_I, n_{II}, n_{III}) = m_{I,X} + m_{II,X} + 4m_{III,X} \tag{78-a}$$

with individual stage gearbox masses

$$\begin{aligned} m_{I,X} &= \rho\pi\kappa \frac{P_e}{\Omega_e}(1+n_I)\left(1+\frac{1}{n_I^{\,2}}\right) \\ m_{II,X} &= \rho\pi\kappa \frac{P_e}{n_I\Omega_e}\left(1+\frac{\sin(\pi/8)}{1-\sin(\pi/8)}\right)\left(2+\left[\frac{1}{\sin(\pi/8)}-1\right]^2\right) \\ m_{III,X} &= \rho\pi\kappa \frac{P_e}{4\Omega_e}\frac{1+n_{III}}{n_I}\left(1+\frac{1}{n_{III}^{\,2}}\right) \end{aligned} \tag{78-b}$$

Again, $m_{I,X}$, $m_{II,X}$, and $m_{III,X}$ are derived based on the same method described in Section 2.1.5. Here, stages I and III are ordinary gear stages each with one input and one output gear, while stage II is a power-dividing stage based on a multiple pinion/face-gear arrangement (see Fig. 29b). It is assumed that the input and output pinions are all the same size, hence the gear ratio of X-type stage II is always 1:1 ($n_{II} = 1$), meaning that its only purpose is as a power distribution stage. Note, the factors involving $\sin(\pi/8)$ in Eq. 78-b arise from the geometric constraint that the face-gear has the smallest possible pitch radius without interferences between adjacent pinions. The power input into stages I and II is P_e and the power input into stage III is $P_e/4$, respectively.

Once either the H-type or X-type layout is chosen and once the desired overall transmission ratio n is selected, the primary design question becomes how to select the best combination of gear ratios n_I, n_{II}, and n_{III} to yield the lowest overall transmission mass. This problem is formulated as the non-convex search for the lowest mass. For the H-type layout starting from Eq. 77 combined with Eq. 76 we have

H-type layout mass function: Search domain: Constraints:

$$m_{gb,H}(n_{II},n_{III}) = m_{gb,H}(n_I(n_{II},n_{III}),n_{II},n_{III}) \qquad \begin{array}{l} [n_{II,\min} \le n_{II} \le n_{II,\max}] \\ [n_{III,\min} \le n_{III} \le n_{III,\max}] \end{array} \tag{79}$$

and for the X-type layout we have

X-type layout mass function: Search domain: Constraints:

$$m_{gb,X}(n_{III}) = m_{gb,X}(n_I(1,n_{III}),1,n_{III}) \quad [n_{III,\min} \le n_{III} \le n_{III,\max}] \quad \begin{array}{l} n_I = \dfrac{n}{n_{II}n_{III}} \\ [n_{I,\min} \le n_I \le n_{I,\max}] \\ n_{II} = 1 \end{array} \tag{80}$$

Where $n_{I,\min}$, $n_{II,\min}$, and $n_{III,\min}$ are the minimum allowable gear ratios of any individual stage, which in this study was set as

$$n_{I,\min} = n_{II,\min} = n_{III,\min} = 0.2 \tag{81-a}$$

and where $n_{I,\max}$, $n_{II,\max}$, and $n_{III,\max}$ are the maximum allowable gear ratios of any individual stage, which in this study was set as

$$n_{I,\max} = n_{II,\max} = n_{III,\max} = 2.0 \tag{81-b}$$

Figure 30 shows an example of how the H-type transmission system mass varies with individual stage ratios for a fixed overall transmission ratio $n = 0.2$ at a 5000 RPM design input speed and 100 Hp design input power level. This figure shows there is a global optimum combination of stage ratios, which achieve minimum overall weight. The minimum weight design for this case is summarized in Table 4.

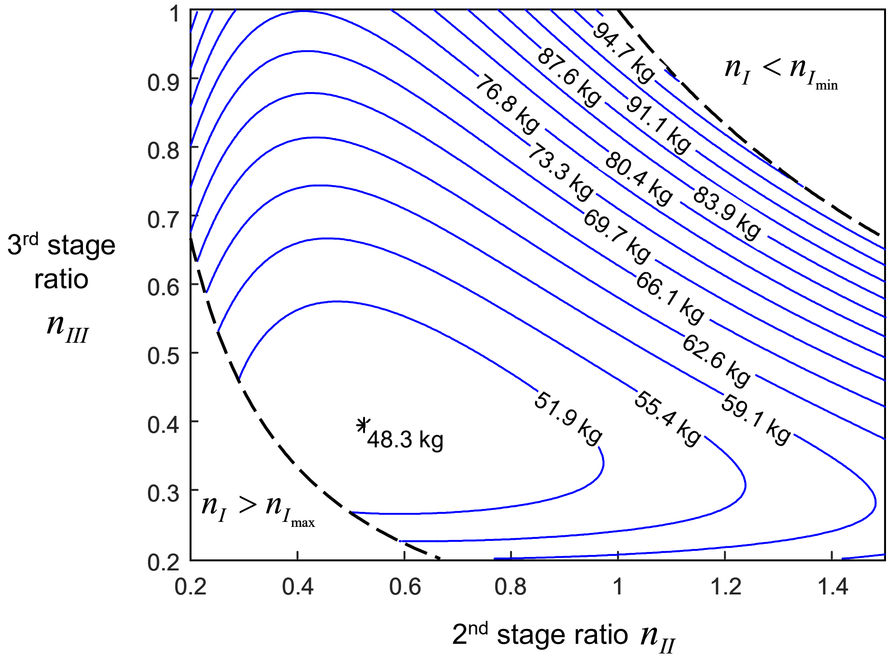

Fig. 30 Total mass contours of H-type transmission system; [*n* = 0.2, P_e = 100 Hp, Ω_e = 5000 RPM]

Table 4 Minimum weight H-type transmission design [*n* = 0.2, P_e = 100 Hp, Ω_e = 5000 RPM]

Transmission property	Stage I	Stage II	Stage III	Overall
Gear ratio	0.966	0.524	0.395	0.2
Gearbox mass	4.97 kg (× 1)	5.26 kg (× 2)	8.21 kg (× 4)	48.3 kg

Qualitatively speaking, Fig. 30 also shows that the design region around the optimum is fairly flat, indicating that there are many practical combinations of stage ratios around the optimum that would yield overall transmission system mass values close to the minimum. Figures 31–33 show the results of the minimum mass design search described in Eqs. 79 and 80 for the X and H-type layouts for the example case with 5000 RPM design input speed and 100 Hp design input power level. Specifically, Fig. 31 shows the minimum achieved total drive system weights

$$W_{gb,H} = m_{gb,H}g \quad \text{and} \quad W_{gb,X} = m_{gb,X}g \tag{82-a}$$

plotted as a function of overall transmission gear ratio *n*.

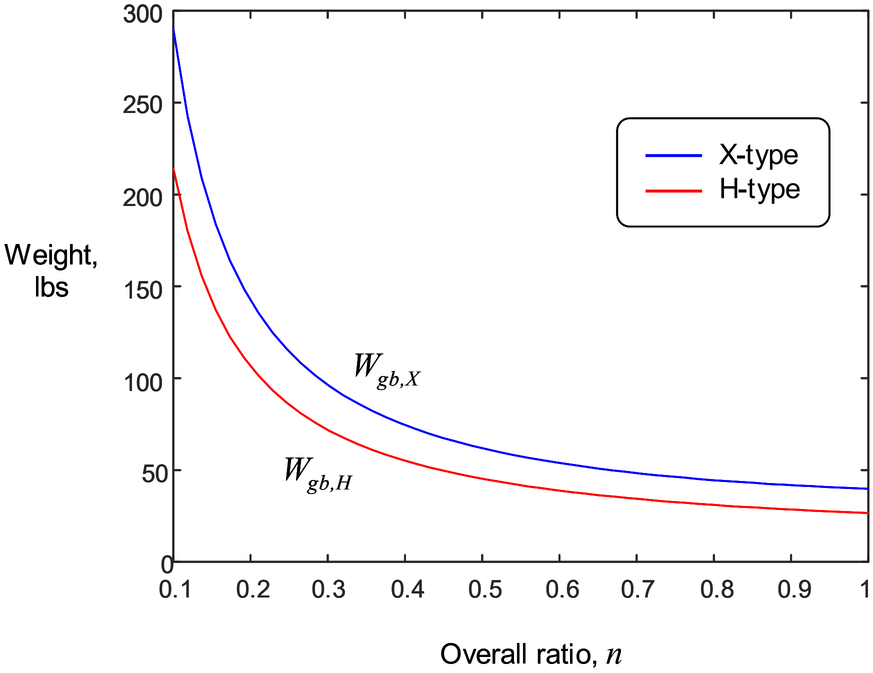

Fig. 31 Minimum transmission system weight design vs. overall ratio [P_e = 100 Hp, Ω_e = 5000 RPM]

Figure 31 shows that the H-type designs are approximately 30% lighter compared to the X-type designs over the entire design range of n, hence making the H-type layout a better design choice. Furthermore, Figs. 32 and 33 show the optimum individual stage ratios and corresponding individual stage weights for the minimum weight H-type and X-type designs, respectively.

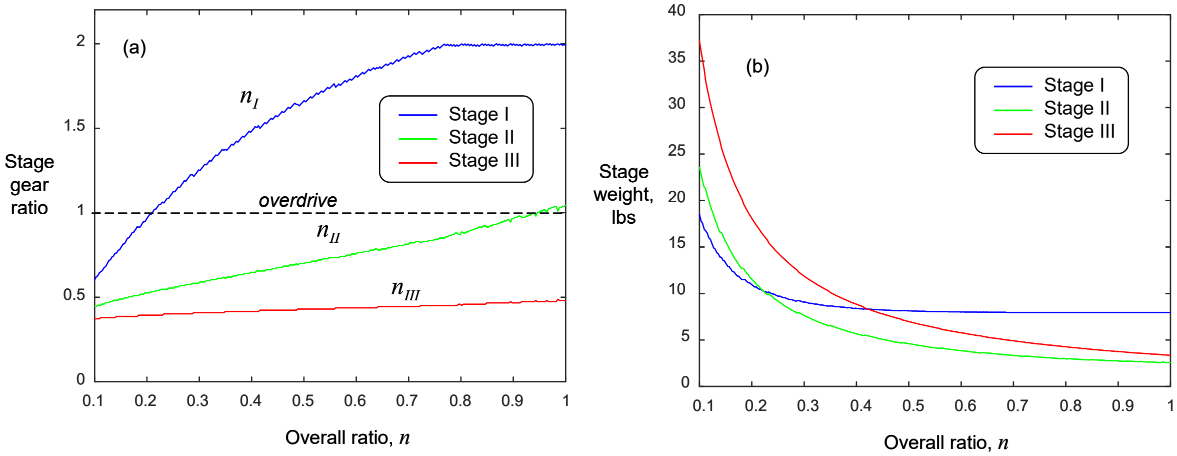

Fig. 32 Minimum weight H-type transmission design details vs. overall gear ratio n: a) individual stage gear ratios, and b) individual gearbox stage weights [P_e = 100 Hp, Ω_e = 5000 RPM]

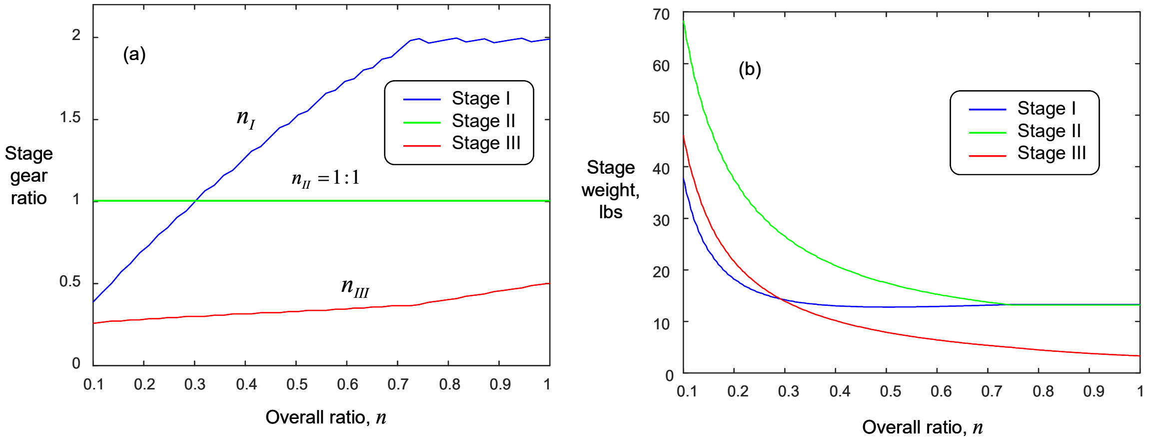

Fig. 33 Minimum weight X-type transmission design details vs. overall gear ratio *n*: a) individual stage gear ratios, and b) individual gearbox stage weights [P_e = 100 Hp, Ω_e = 5000 RPM]

The minimum weight design results for both the X-type and H-type layouts show that when the overall reduction ratio, *n*, is sufficiently small ($n < 0.2$ for H-type and $n < 0.3$ for X-type) then n_I, n_{II}, and n_{III} are all less than 1 (i.e., they are all reduction stages). However, for moderate overall gear reductions ($n > 0.2$ for H-type and $n > 0.3$ for X-type) the optimizer makes n_I greater than 1, meaning the first stage becomes an overdrive stage while stages II and III remain reduction stages (i.e., $n_{II} < 1$ and $n_{III} < 1$). Please refer to Figs. 32a and 33a. What this means is, for moderate overall reductions, *n*, ideally only two gear reduction stages would be needed, which would enable the first stage to be dropped entirely, saving even more weight. However, since all three gearbox stages are necessary for power redirection and distribution from the engines to the rotors (see Figs. 29a and b), the next best solution is to make $n_I > 1$. By overdriving the first stage, the downstream torque transmitted to the second and third stages becomes reduced, yielding an overall weight savings in stages II and III. The total transmission system mass is most heavily dominated by the final output gearboxes in stage III (there are N_r of them, see Eqs. 77-a and 78-a). For both X-type and H-type transmissions, the output power of the final stage (stage III) gearbox is equal to the rotor power, hence, in hover and forward flight we require

$$P_e = \frac{N_r P_r}{\eta_{gb}} \tag{82-b}$$

Where η_{gb} is the overall transmission efficiency computed as

$$\eta_{gb} = \eta_I \eta_{II} \eta_{III} \tag{83}$$

where η_I, η_{II}, and η_{III} are the individual gear stage efficiencies, which are assumed to be $\eta_I = \eta_{II}$ $\eta_{III} = 0.97$. The minimum transmission system mass design process described here is executed during each iteration step of the main design code for the multirotor VTOL UAV (Fig. 24) to ensure an overall optimum design.

3.1.6 Fuel Tank Mass Estimation

Another contributor to the IC engine-powered UAV system mass is the fuel tank. The required fuel tank volume V_{ft} is

$$V_{ft} = \frac{m_{f,0}}{\rho_f} \tag{84}$$

Where $m_{f,0}$ is the maximum fuel mass to be carried and ρ_f is the fuel mass density. Next, following Johnson,[11] the fuel tank mass, m_{ft}, is empirically estimated as

$$m_{ft} = 42.72 * V_{ft} + 30.65 \quad \text{Units: } m_{ft}\{\text{g}\},\ V_{ft}\{\text{L}\} \tag{85}$$

3.1.7 IC Engine-Powered Multirotor UAV Structural Mass Estimation

The remaining major system mass contribution to be included in the sizing analysis is the vehicle structural mass m_s. In the case of the IC engine-powered VTOL UAV considered in this study, m_s is estimated as

$$m_s = f_{sm}(m_r N_r + m_{gb} + m_e + m_{ft} + m_p + m_{f,0}) \tag{86}$$

where f_{sm} the structural mass fraction. This is the same structural mass estimation approach used for the battery-electric VTOL UAV configuration (Eq. 53). This study considers f_{sm} = 0.25, which is a measure of overall structural efficiency.

3.2 IC Engine-Powered Multirotor VTOL UAV Design Results

This section shows the design and performance results obtained by applying the sizing and design code outlined in Fig. 24 and described in Section 3.1 for the medium-scale IC piston engine-powered multirotor VTOL UAV configuration shown in Fig. 23.

Table 5 gives the system parameters used in the design study and analysis. To begin the study, the sizing code is used to generate a family of designs over a range of overall transmission gear ratios, n, for different initial fuel loads, $W_{f,0}$, and different maximum payload weights, W_p.

$$W_{f,0} = m_{f,0} g \quad \text{and} \quad W_p = m_p g \tag{87}$$

Table 5 Fixed design parameters for medium-scale IC engine-powered multirotor VTOL UAV

Parameter	Value	Parameter	Value
Acceleration of gravity, g	9.81 m/s^2	Transmission layout:	X or H type (3 stage)
Air density, ρ	1.225 kg/m^3	Overall gear ratio, n	[$0.2 < n_{gb} < 1.0$]
		Stage efficiencies, η_I η_{II} η_{III}	0.97
Number of rotors, N_r	4	Gear pressure angle, ϕ	20°
Number of blades per rotor, N_b	4		
Blade lift coefficient slope, a_L	5.7	Gear material:	7870 kg/m^3
Blade drag coefficient, C_{d0}	0.008	Density, ρ_g	200 GPa
Rotor solidity ratio, σ	0.12	Elastic modulus, E	0.29
Blade pitch in hover, $\theta_{75,h}$	10°	Poisson's ratio, ν	125,000 psi
Blade tip speed, v_t	550 ft/s	Contact strength, s_{fc}	
			1.0
Structural mass fraction, f_{sm}	0.25	Four stroke piston engine:	4.0
		Stroke over bore ratio, SB	0.95
Fuel:	43.71 MJ/kg	Number of cylinders, N_{cyl}	
Lower heating value, LHV	720 kg/m^3	Throttle parameter in hover, β_h	
Density, ρ_f			

Figures 34 and 35 show the calculated forward flight range results for the IC engine-powered quadrotor (N_r=4) configuration for three maximum design payloads W_p = [200, 300, and 400] lb as a function of n using both the X-type and H-type transmission layouts. Specifically, the results in Fig. 34 are for the case with a maximum fuel capacity of $W_{f,0}$=5 lb and Fig. 35 gives the results for the case with $W_{f,0}$=50 lb. Here, each point on the figures represents a unique quadrotor design, which is operating at the optimum forward speed, v_v, for maximum range.

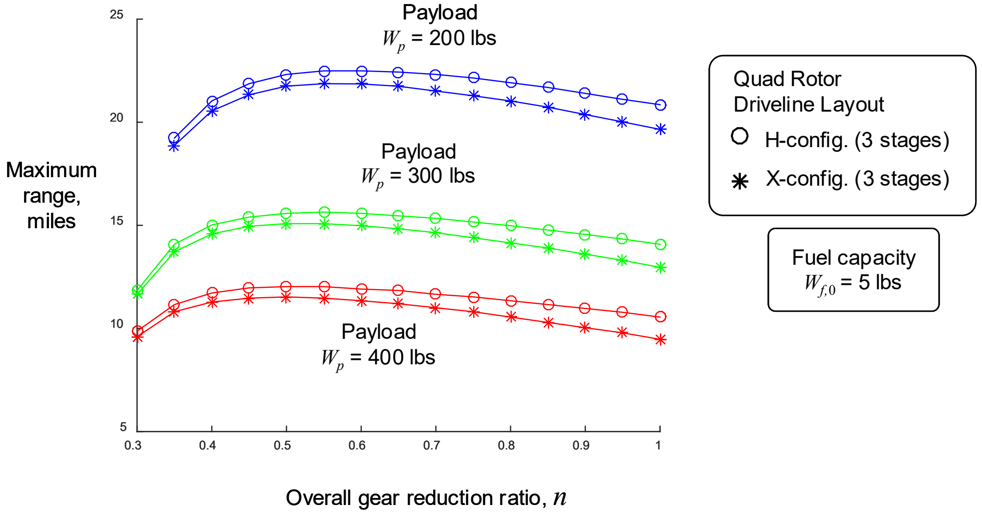

Fig. 34 IC engine-powered quadrotor results: maximum range vs. overall gear ratio with $W_{f,0}$ = 5 lb

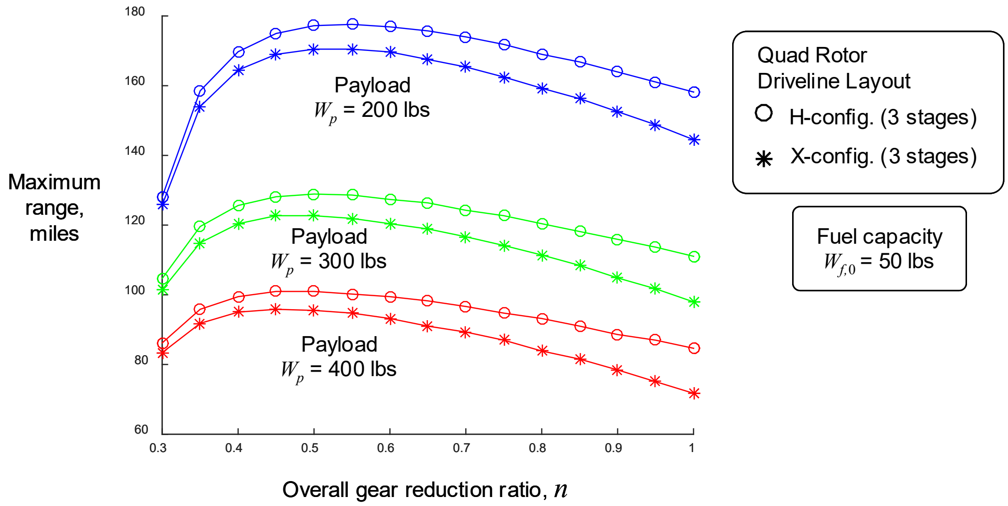

Fig. 35 IC engine-powered quadrotor results: maximum range vs. overall gear ratio with $W_{f,0}$ = 50 lb

These figures show that, for a given W_p, there is an optimum transmission ratio, n, which maximizes the forward flight range. Furthermore, the results show that the H-type transmission layout outperforms the X-type as expected due to lower mass of the H-type for a given n.

Next, the sizing code was used to generate designs that maximize forward flight range by simultaneously optimizing over both gear ratio, n, and forward speed, v_v. These results are summarized in Figs. 36–39. In particular, Figs. 36 and 37 show the design details for the IC engine-powered quadrotor equipped with the X-type transmission layout for the case having a 10-lb ($W_{f,0}$ = 10 lb) fuel capacity. Furthermore, Fig. 38 shows the corresponding hover endurance (Fig. 38a) and maximum range (Fig. 38b) for the fully optimized IC engine-powered quadrotor over the range of design payload levels from W_p = [100 to 400 lb] for three different fuel capacities $W_{f,0}$ = [5, 10, and 15 lb]. As expected, for a fixed fuel capacity, both the hover endurance and flight range decrease with increasing payload. However, it is observed that this decrease is nonlinear. Furthermore, both hover endurance and range can be increased by increasing onboard fuel capacity, which is also shown in Fig 39.

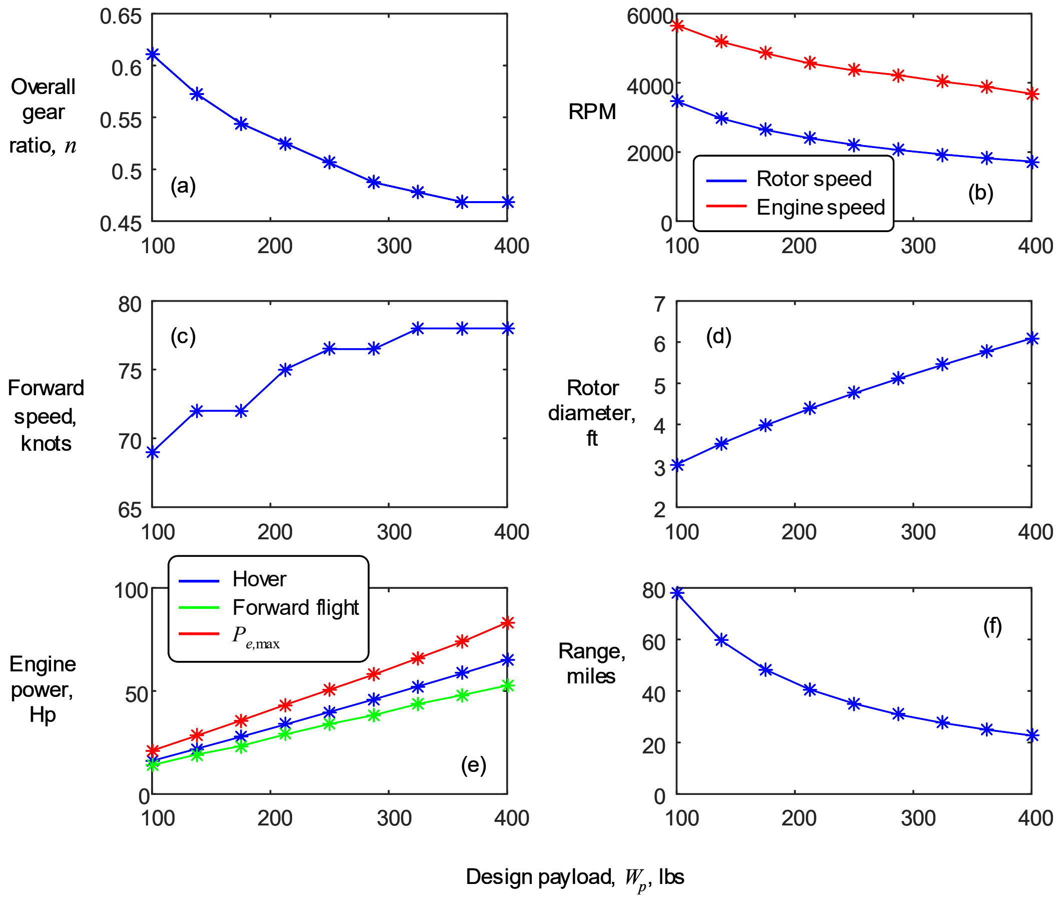

Fig. 36 IC engine-powered quadrotor optimization for different payloads: a) optimum gear ratio (X-type); b) engine and rotor RPM; c) optimum speed; d) rotor diameter; e) engine power; f) range

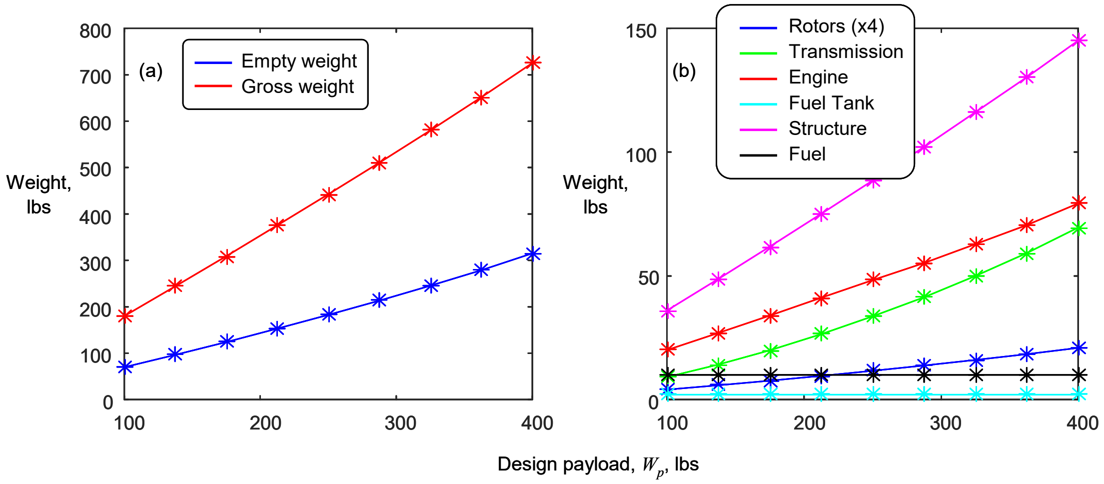

Fig. 37 IC engine-powered quadrotor optimization at different design payloads: a) vehicle empty and gross weight; b) component weights (X-type transmission)

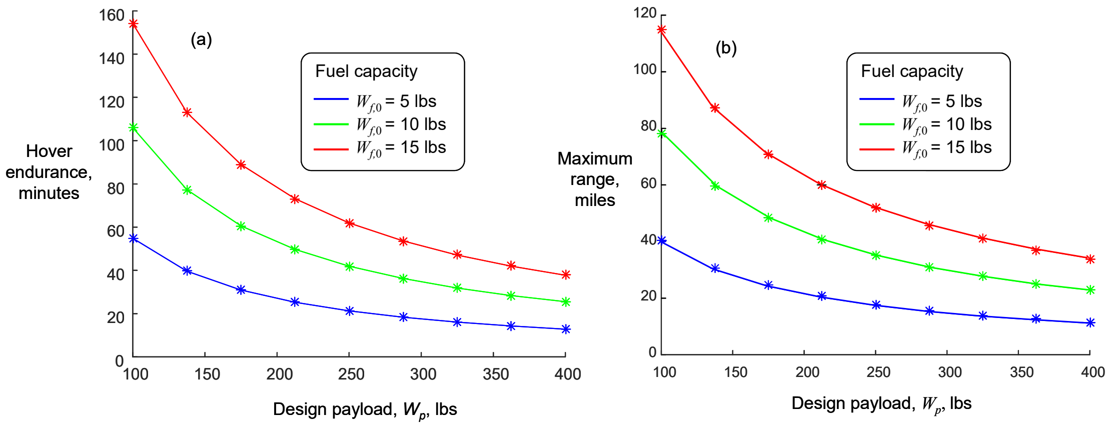

Fig. 38 Optimized IC engine-powered quadrotor performance vs. design payload: a) hover endurance; b) maximum range (X-type transmission)

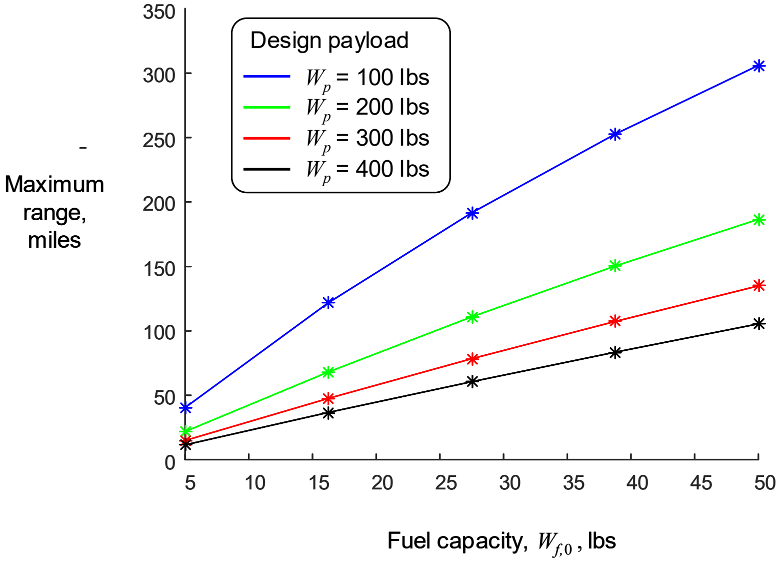

Fig. 39 Optimized IC engine-powered quadrotor performance: maximum range vs. fuel capacity (X-type transmission)

Figure 39 demonstrates that the maximum flight range scales monotonically with onboard fuel capacity. This behavior is unlike the battery-electric case (Figs. 14 and 15) where a peak range value occurs at a particular optimum battery weight, beyond which the range then decreases with increasing battery weight. Thus, comparing Fig. 39 with Figs. 14 and 15 it is concluded that the medium-scale gas IC engine-powered quadrotor UAV performance is much more scalable.

Finally, Figs. 40 and 41 show the forward flight performance results as a function of vehicle forward speed, v_V, for a particular IC engine-powered quadrotor design. Figure 41a shows how the blade collective pitch, θ_{75}, is adjusted as dictated by the trim solution. Finally, these figures also show that there is an optimum vehicle forward cruising speed that minimizes the fuel burn rate (Fig. 41b) and another speed that maximizes the flight range (Fig. 40a).

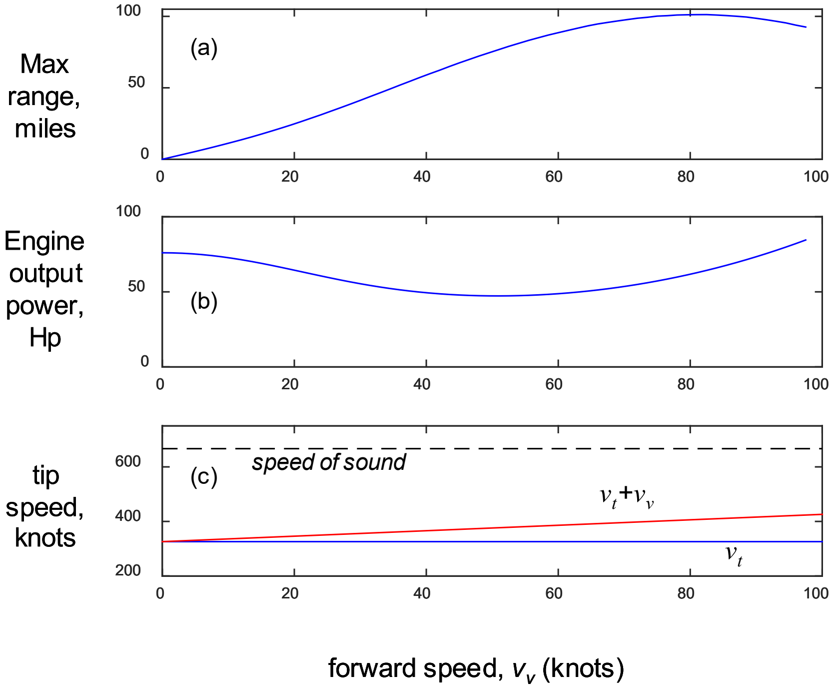

Fig. 40 **IC engine-powered quadrotor UAV forward flight performance vs. forward speed: a) maximum range, b) engine output power, c) blade tip speed; [$n = 0.45$ (H-type layout), fuel capacity $W_{f,0} = 50$ lb, payload $W_p = 400$ lb, $N_r = 4$]**

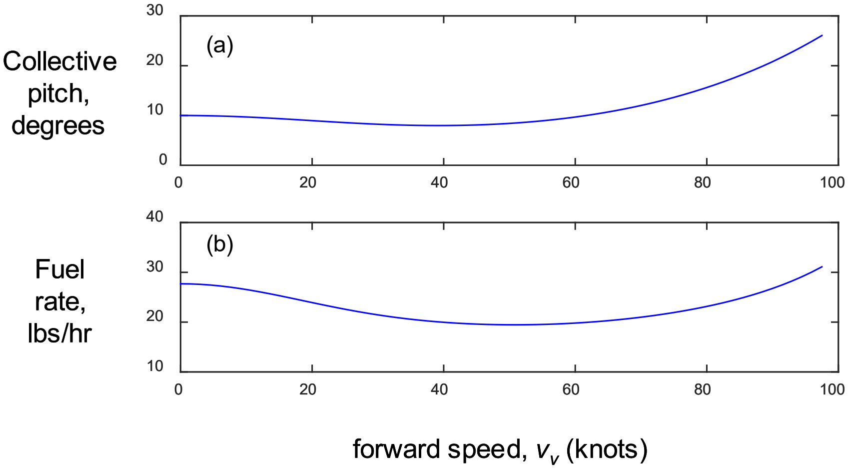

Fig. 41 **IC engine-powered quadrotor UAV forward-flight performance vs. forward speed: a) blade collective pitch, b) fuel burn rate; [$n = 0.45$ (H-type layout), fuel capacity $W_{f,0} = 50$ lb, payload $W_p = 400$ lb, $N_r = 4$]**

4. Serial Hybrid Gas-Electric Multirotor UAV Configuration

This section describes the design and analysis of a serial hybrid gas-electric powered multirotor VTOL UAV system depicted schematically in Fig. 42. As before, the design is conducted based on the assumption of quasi-steady operation.

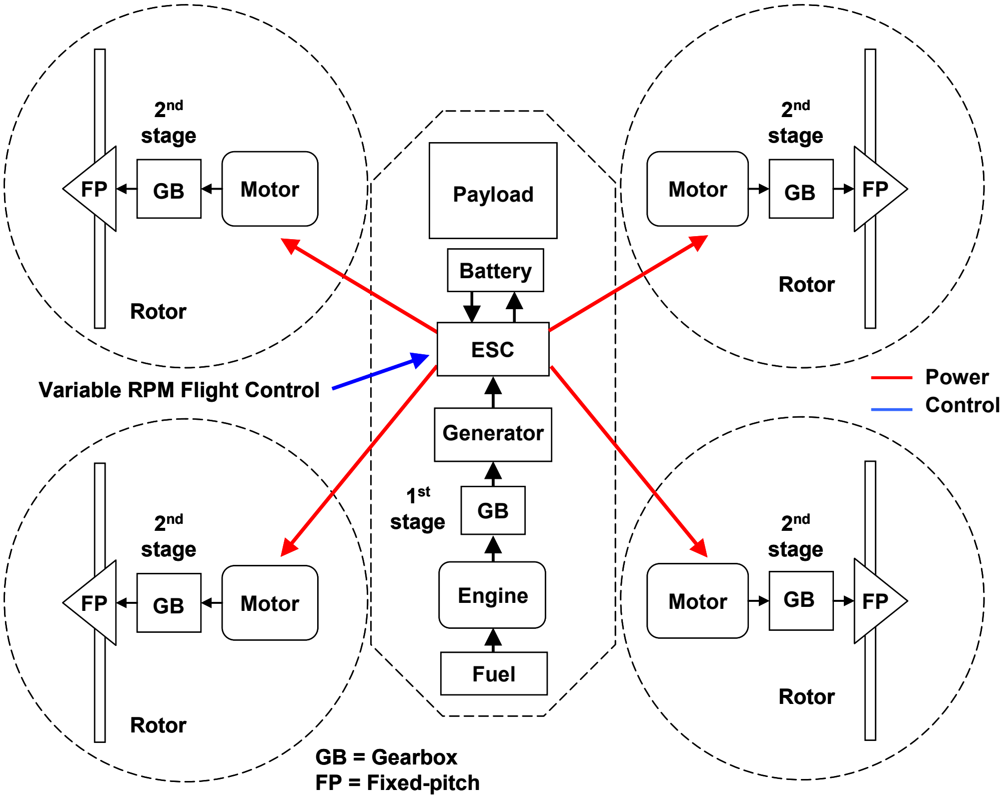

Fig. 42 **Serial hybrid gas-electric powered multirotor UAV with variable rotor RPM flight control**

In this configuration, there is no direct mechanical connection between engine and rotors. Instead, the centralized IC piston engine drives a generator that feeds electric power into the ESC along with a battery. The ESC then distributes the electric power to each of the nacelle motors to drive the rotors and variable rotor RPM flight control is assumed. In this arrangement, two gearbox stages are also included: 1) a first-stage gearbox located between the engine and generator and 2) a second-stage gearbox located between the electric motors and the rotors. The purpose of both gearbox stages is to provide the potential for optimized impedance matching between each element. For this investigation, an iterative sizing algorithm and design code is developed and utilized to obtain a family of feasible designs. The hover and forward flight performance of these designs is then evaluated for a variety of payloads and forward speeds.

4.1 Modeling and Design of Series Hybrid Gas-Electric VTOL UAV

Similar to the pure electric and pure gas-powered cases presented in Sections 2 and 3, an iterative design code is developed that determines the size of each component based on power and energy requirements during hover conditions. The flowchart of the sizing algorithm developed under this project for the series hybrid gas-electric multirotor VTOL UAV configuration is shown in Fig. 43.

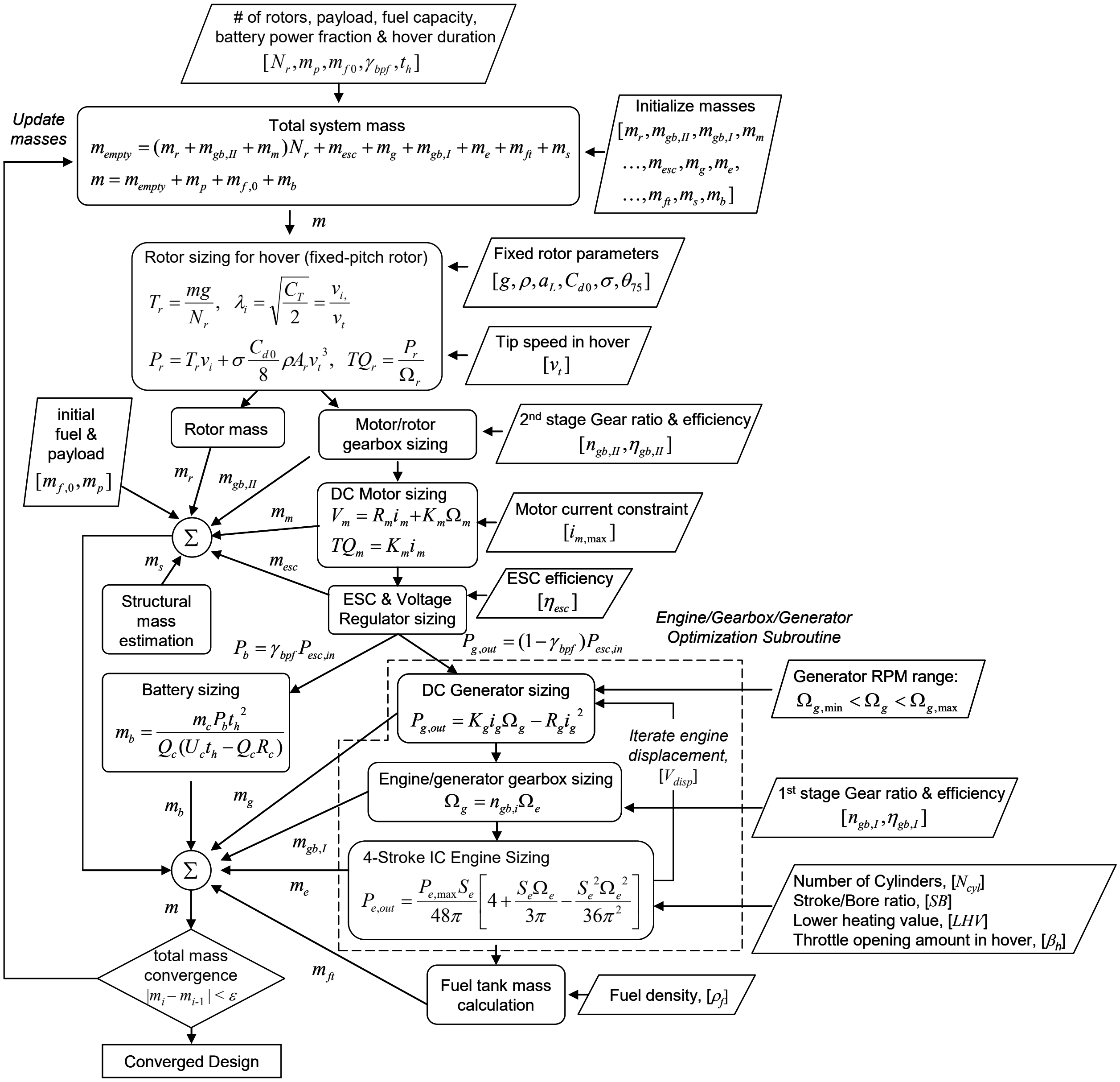

Fig. 43 Iterative sizing algorithm for design of the series hybrid gas-electric multirotor VTOL UAV configuration with variable RPM rotor flight control

To evaluate the hover and forward flight performance, the total gross weight of the vehicle must be computed. The total mass, m, and empty mass, m_{empty}, are

$$\begin{aligned} m_{empty} &= (m_r + m_{gb,II} + m_m)N_r + m_{esc} + m_g + m_{gb,I} + m_e + m_{ft} + m_s \\ m &= m_{empty} + m_p + m_{f,0} + m_b \end{aligned} \tag{88}$$

Where m_{empty} is composed of the N_r rotor masses, m_r, the N_r motor-rotor gearbox masses, $m_{gb,II}$, the N_r electric motor masses, m_m, the ESC mass, m_{esc}, the DC electric generator mass, m_g, the IC engine mass, m_e, the engine-generator gearbox mass, $m_{gb,I}$, the fuel tank mass, m_{ft}, and the vehicle structural mass m_s. Furthermore, the total vehicle mass, m, consists of m_{empty} together with the fuel, battery, and payload masses $m_{f,0}$, m_b, and m_p respectively. The iterative design code determines the size of each component based on power and energy requirements during hover. Starting with initialized mass estimates for each component, the required rotor thrust, T_r, and rotor power, P_r, is computed. These results are then propagated down the drivesystem where each subsequent component is sized based on the required rotational speed and power levels. The updated component masses from the i^{th} iteration step are then used to generate a new estimate, $m_{empty,i}$, which is compared with the prior estimate, $m_{empty,i-1}$, to evaluate convergence (see Fig. 43). The details of each component model are described in the following subsections.

4.1.1 Hover and Forward-Flight Aeromechanics Model

Please refer to Section 2.1.1 since the hover and forward-flight aeromechanics model is identical to the models used for the battery-electric and IC engine-powered quadrotor cases.

4.1.2 Fixed-Pitch Variable Speed Rotor Trim Solution in Forward Flight

Please refer to Section 2.1.2 since both the battery-electric and series gas-electric hybrid cases designed in this study utilize the identical fixed-pitch rotor, variable rotor RPM flight control method.

4.1.3 Rotor Sizing Based on Hover Condition

Please refer to Section 2.1.3 since the rotor model and sizing process for the battery-electric and series gas-electric hybrid multirotor UAV cases are identical.

4.1.4 DC Electric Motor Model

Please refer to Section 2.1.4 since the motor model and sizing process for the battery-electric and series gas-electric hybrid multirotor UAV cases are identical.

4.1.5 DC Electric Generator Model

The series hybrid configuration utilizes a DC electric generator to convert mechanic power proved by the gas IC engine into electrical power to drive the motors. Here, the DC generator model is essentially identical to the DC electric motor model in Section 2.1.4. The steady-state model of the DC electric generator is depicted schematically in Fig. 44.

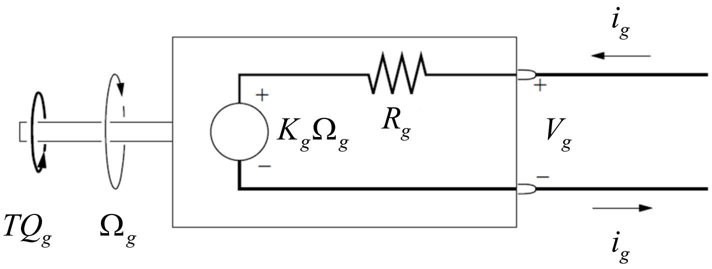

Fig. 44 Permanent magnet DC electric generator model

The steady-state torque and voltage relations assumed for the generator are

$$\begin{aligned} V_g &= R_g i_g + K_g \Omega_g \\ TQ_g &= K_g i_g \end{aligned} \tag{89}$$

Here, V_g is generator armature voltage, i_g is generator current, TQ_g is generator shaft torque, and Ω_g is generator shaft rotation speed. The generator parameters are the torque constant, K_g, and armature resistance R_g. It is also common to define the speed constant

$$K_{v,g} = \frac{1}{K_g} \tag{90}$$

which is typically reported in units of RPM/V. Following Johnson,[11] the generator mass, m_g, is estimated based on the maximum design torque $TQ_{g,\max}$ as

$$m_g = 0.137(TQ_{g,\max})^{0.8587} \qquad \text{Units}: TQ_{g,\max}\ \{\text{Nm}\},\ m_g\ \ \{\text{kg}\} \tag{91}$$

Furthermore, following Gur and Rosen,[12] $K_{v,g}$ is empirically estimated based on m_g as

$$K_{v,g} = \frac{B_K}{m_g} \quad \text{Units}: K_{v,g}\left\{\frac{\text{RPM}}{\text{V}}\right\},\ m_g\ \ \{\text{kg}\} \tag{92}$$

Where $B_K = 170 \left\{\frac{\text{RPM kg}}{\text{V}}\right\}$ was selected and used in the present study. Next, further following Gur and Rosen,[12] R_g is empirically estimated using

$$R_g = \frac{B_R}{{K_{v,g}}^2} \qquad \text{Units}: K_{v,g}\left\{\frac{\text{RPM}}{\text{V}}\right\},\ R_g\ \{\Omega\} \tag{93}$$

Where $B_R = 60{,}000\left\{\frac{\text{V}^2\,\Omega}{\text{RPM}^2}\right\}$ was used in the present study. In addition, the generator input power, $P_{g,in}$, and output power, $P_{g,out}$, are computed as

$$P_{g,in} = TQ_g \Omega_g \ \text{ and } \qquad P_{g,out} = V_g i_g \tag{94}$$

Which after applying Eq. 21 gives the relation

$$P_{g,out} = P_{g,in} - R_g {i_g}^2 \tag{95}$$

Finally, generator efficiency is computed as

$$\eta_g = \frac{P_{g,out}}{P_{g,in}} \tag{96}$$

4.1.6 Internal Combustion Piston Engine Model

In this study, both the gas IC engine-powered UAV and the hybrid gas-electric UAV configurations share the same piston engine model. Please refer to Section 3.1.4 for the engine model details.

4.1.7 Electric Battery Model

In this study, both the battery-electric powered UAV and the hybrid gas-electric UAV configurations share the same multi-cell Li-Po battery model. Please refer to Section 2.1.6 for the details of the electric battery model.

4.1.8 Gearbox Sizing

As shown in Fig. 42, the serial hybrid gas-electric propulsion system model includes the possibility of a gearbox stage between the engine and generator (stage I), and another gearbox stage between the motor and rotor (stage II). See Fig. 45.

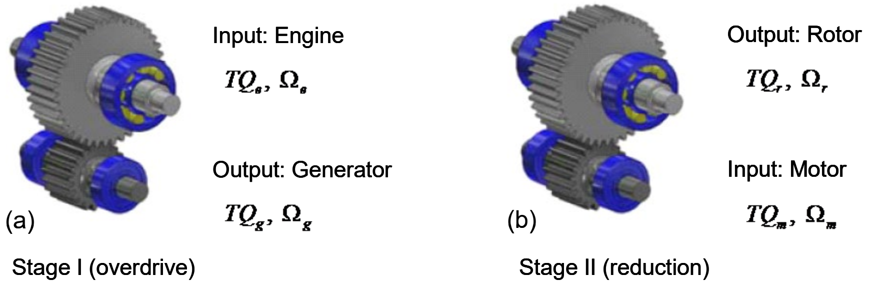

Stage I (overdrive)

Stage II (reduction)

Fig. 45 Single-stage gearboxes in serial gas-electric hybrid multirotor UAV: a) stage I, engine-generator gearbox (overdrive) and b) stage II, motor-rotor gearbox (reduction)

By connecting the engine and generator with gearbox stage I, we have the following rotational speed and torque relations

$$\Omega_g = \eta_{gb,I}\Omega_e \quad \text{and} \quad TQ_g = \eta_{gb,I}\frac{TQ_e}{n_{gb,I}} \tag{97}$$

and due to the presence of the stage II motor-rotor gearbox we also have

$$\Omega_r = \eta_{gb,II}\Omega_m \quad \text{and} \quad TQ_r = \eta_{gb,II}\frac{TQ_m}{n_{gb,II}} \tag{98}$$

Where $n_{gb,I}$ and $n_{gb,II}$ are the gear ratios and $\eta_{gb,I}$ and $\eta_{gb,II}$ are the efficiencies of gearbox stages I and II respectively. In each case, the gearbox masses are estimated based on the single-stage gearbox mass calculation method described in Section 2.1.5. In particular, for stage I we have

$$\begin{aligned} m_{gb,I} &= \rho_g \pi \frac{C_p^{\,2}}{\bar{s}_{fc}^{\,2}\cos\phi\sin\phi} K_o K_v K_s K_m C_f \left(1 + n_{gb,I}\right)\left(1 + \frac{1}{n_{gb,I}^{\,2}}\right) TQ_e && \text{for } n_{gb,I} \neq 1 \\ m_{gb,I} &= 0 && \text{for } n_{gb,I} = 1 \end{aligned} \tag{99}$$

and for the mass of stage II we have

$$\begin{aligned} m_{gb,II} &= \rho_g \pi \frac{C_p^{\,2}}{\bar{s}_{fc}^{\,2}\cos\phi\sin\phi} K_o K_v K_s K_m C_f \left(1 + n_{gb,II}\right)\left(1 + \frac{1}{n_{gb,II}^{\,2}}\right) TQ_m && \text{for } n_{gb,II} \neq 1 \\ m_{gb,II} &= 0 && \text{for } n_{gb,II} = 1 \end{aligned} \tag{100}$$

where the mass dropout case (m_{gb}=0) for 1:1 ratio direct-drive (no gearbox) situation is included.

4.1.9 Electronic Speed Controller and Power Converter

The interface between the generator, the battery, and the electric motors is the ESC, which is depicted schematically in Fig. 46.

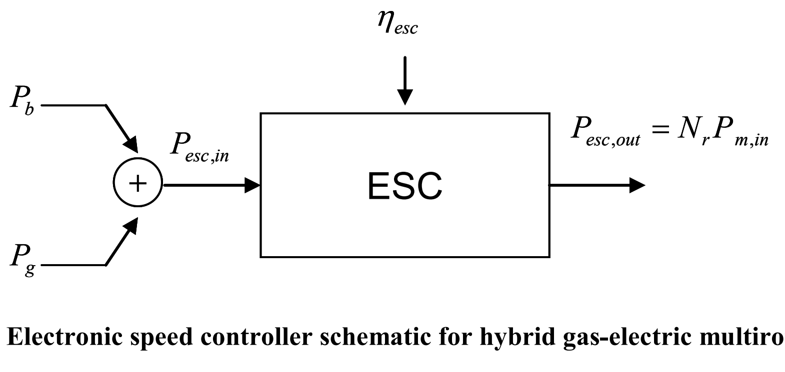

Fig. 46 Electronic speed controller schematic for hybrid gas-electric multirotor UAV

The required ESC output power, $P_{esc,out}$, is given in Eq. 49, and the relation between the ESC input power, $P_{esc,in}$, efficiency, η_{esc}, and $P_{esc,out}$, are given in Eq. 50. Furthermore, in this case, the ESC accepts electric power from both the generator and the battery hence we have

$$P_{esc,in} = P_{g,out} + P_b \tag{101}$$

After considering Eqs. 21, 26–28, 97, 49, and 50, the total required ESC input power in terms of rotor power, P_r, and rotor torque, TQ_r, is found to be

$$P_{esc,in} = \frac{N_r}{\eta_{esc}}\left(\frac{P_r}{\eta_{gb,II}} + \left(\frac{n_{gb,II}}{\eta_{gb,II}}\right)^2 TQ_r^{\,2}\frac{R_m}{K_m^{\,2}}\right) \tag{102}$$

Combining Eqs. 101 and 102 we arrive at the following condition for operation,

$$P_{g,out} + P_b = \frac{N_r}{\eta_{esc}}\left(\frac{P_r}{\eta_{gb,II}} + \left(\frac{n_{gb,II}}{\eta_{gb,II}}\right)^2 TQ_r^{\,2}\frac{R_m}{K_m^{\,2}}\right) \tag{103}$$

Finally, the ESC mass is estimated using the empirical relation (Eq. 52) as before.

4.1.10 Fuel Tank

Please refer to Section 3.1.6 since the fuel tank sizing process for both the IC engine-powered UAV and series gas-electric hybrid UAV are identical.

4.1.11 Hybrid Gas-Electric Multirotor UAV Structural Mass Estimation

The remaining major system mass contribution to be included in the sizing analysis is the vehicle structural mass m_s. In the case of the hybrid gas-electric powered VTOL UAV considered in this study, m_s is estimated as

$$m_s = f_{sm}((m_r + m_{gb,II} + m_m)N_r + m_{esc} + m_g + m_{gb,I} + m_e + m_{ft} + m_p + m_{f,0} + m_b) \tag{104}$$

where f_{sm} the structural mass fraction. This is the same structural mass estimation approach used for the battery-electric VTOL UAV configuration (Eq. 53). This study considers $f_{sm} = 0.25$, which is a measure of overall structural efficiency.

4.1.12 Battery Sizing and Engine/Gearbox/Generator Subsystem Optimization

As was done for both the battery-electric and IC engine-powered cases in Sections 2 and 3, the hybrid gas-electric UAV system is sized around the hover condition since this will be considered the maximum power demand case.

Starting with Eq. 102 together with Eqs. 13, 18, and 19, the required power input into the ESC during hover is

$$P_{esc,in,h} = \frac{N_r}{\eta_{esc}} \left(\frac{P_{r,h}}{\eta_{gb,II}} + \left(\frac{n_{gb,II}}{\eta_{gb,II}} \right)^2 TQ_{r,h}^{\ 2} \frac{R_m}{K_m^{\ 2}} \right) \tag{105-a}$$

where the rotor torque during hover is

$$TQ_{r,h} = \frac{1}{v_{t,h}} \sqrt{\frac{m^3 g^3}{2\rho\pi N_r^{\ 3}}} + \sigma \frac{C_{d0}}{8} \rho\pi R_r^{\ 3} v_{t,h}^{\ 2} \tag{105-b}$$

and the rotor power during hover is

$$P_{r,h} = \frac{1}{R_r} \sqrt{\frac{m^3 g^3}{2\rho\pi N_r^{\ 3}}} + \sigma \frac{C_{d0}}{8} \rho A_r v_{t,h}^{\ 3} \tag{105-c}$$

In the case of the hybrid gas-electric UAV, both the engine and battery can simultaneously add power to the rotor through the ESC (Eq. 101). Thus, during hover we have

$$P_{b,h} + P_{g,out,h} = P_{esc,in,h} \tag{106}$$

Where $P_{b,h}$ and $P_{g,out,h}$ are the electric power outputs from the battery and generator, respectively, during hover. The relative power contribution between the battery and engine becomes an important additional degree-of-freedom in hybrid gas-electric UAV design and operation. In order to proceed with the design, we define the battery power fraction parameter, γ_{bpf}, as follows

$$P_{b,h} = \gamma_{bpf} P_{esc,in,h} \quad \text{and} \quad P_{g,out,h} = (1-\gamma_{bpf}) P_{esc,in,h} \quad \text{with} \quad [0 < \gamma_{bpf} < 1] \tag{107}$$

which satisfies condition (106). Here, γ_{bpf}, is a non-dimensional design parameter, which selects the battery and generator power contributions during hover. Upon selection of γ_{bpf} and applying Eqs. 105 and 107, $P_{b,h}$ and $P_{g,out,h}$, can be explicitly computed for a given total vehicle mass, *m*. In this study, it is assumed that both the battery and engine are used during hover (i.e., $\gamma_{bpf} \neq 0$) and that only the engine is used during forward flight (i.e., γ_{bpf}=0).

$$P_b = \begin{cases} \gamma_{bpf} P_{esc,in,h} & \text{hover} \\ 0 & \text{forward flight} \end{cases} \quad \text{and} \quad P_{g,out} = \begin{cases} (1-\gamma_{bpf}) P_{esc,in,h} & \text{hover} \\ P_{esc,in} & \text{forward flight} \end{cases} \tag{108}$$

Hence, the mass of the battery, m_b, can now be determined based on $P_{b,h}$ for a specified hover endurance time, t_h, using Eq. 45. Note, in Eq. 45, t_d is specified as $t_d = t_h$.

Next, the engine and generator are sized and matched using the following procedure. First, using Eqs. 89, 94, and 95 we obtain the general relation

$$P_{g,out} = TQ_g\Omega_g - \frac{R_g}{K_g^{\ 2}}TQ_g^{\ 2} \tag{109}$$

from which we solve the quadratic formula for the generator input torque TQ_g required to deliver $P_{g,out}$ at a given Ω_g as

$$TQ_g = \frac{\Omega_g}{2a_g} - \sqrt{\frac{\Omega_g^{\ 2}}{4a_g^{\ 2}} - \frac{P_{g,out}}{a_g}} \quad \text{with} \quad a_g = \frac{R_g}{K_g^{\ 2}} \tag{110}$$

Where the ratio parameter, a_g, is defined for convenience. It is also noted based on the generator empirical relation (Eq. 93) that

$$a_g = B_R\left(\frac{\pi}{30}\right)^2 \tag{111}$$

is a mass independent constant. From Eq. 110, it is also observed that, for any given $P_{g,out}$, there is a minimum generator rotation speed

$$\Omega_{g,\min} = 2\sqrt{a_g P_{g,out}} \tag{112}$$

below which the generator cannot deliver the demanded output power.

Using these relations in addition to the gearbox and engine equations in Section 4.1.8 and Section 3.1.4, the procedure for matching and optimizing the engine and generator through the stage I gearbox with specified ratio $n_{gb,I}$ and efficiency $\eta_{gb,I}$ for a specified generator output power $P_{g,out}$ at a specified engine throttle opening β is developed. The engine/gearbox/generator matching and minimum weight design subroutine is described in Fig. 47. This algorithm searches over a specified generator operating speed range

$$\text{Search range: } [\Omega_{g,\min} < \Omega_g < \Omega_{g,\max}] \tag{113}$$

for the minimum mass design of the combined engine, stage I gearbox, and generator subsystem mass, m_{egg}

$$m_{egg} = m_e + m_{gb,I} + m_g \tag{114}$$

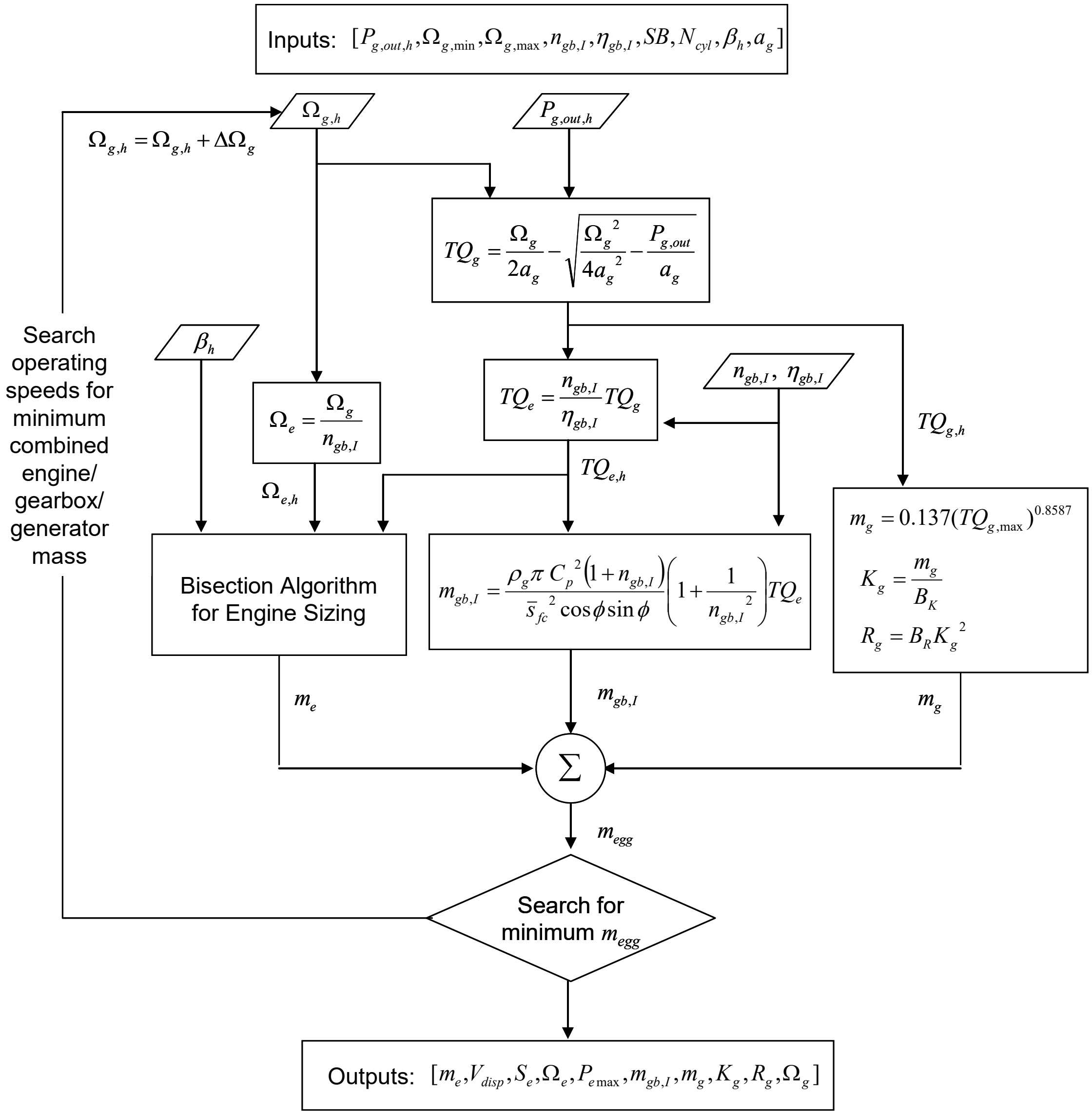

Fig. 47 Engine/gearbox/generator matching and optimization subroutine (also see Figs. 43 and 28)

This subroutine, which also contains the engine bisection sizing algorithm descried in Fig. 28, is executed during each iteration step within the overall hybrid gas-electric multirotor VTOL UAV design code (see Fig. 43).

4.1.13 Engine/Generator Running Line Calculation

The lack of direct mechanical connection between engine and rotors enables one of the key potential advantages offered by the serial hybrid configuration, which is the ability to adjust engine operating speed, Ω_e, independent of rotor speed, Ω_r, for a given load condition in order to maximize the fuel efficiency (i.e., minimize the fuel burn rate $\dot{m}_f$). For a given engine/gearbox/generator system, there are multiple

$[\Omega_e, TQ_e, \beta]$ combinations that yield a given generator output power, $P_{g,out}$. The engine torque, TQ_e, required for the generator to output $P_{g,out}$ is determined from the TQ_g expression in Eq. 110 together with the stage I gearbox relations (Eq. 97) giving

$$TQ_e = \frac{n_{gb,I}{}^2}{\eta_{gb,I}} \frac{\Omega_e}{2a_g} - \sqrt{\left(\frac{n_{gb,I}{}^2}{\eta_{gb,I}} \frac{\Omega_e}{2a_g}\right)^2 - \left(\frac{n_{gb,I}}{\eta_{gb,I}}\right)^2 \frac{P_{g,out}}{a_g}} \tag{115}$$

Next, this expression is equated with the partial throttle engine torque curve (Eq. 67) as

$$\underbrace{\frac{P_{e,\max} S_e}{\pi^3 v_P} \left(\frac{\beta 4\pi^2 v_{TQ}{}^2 + 2\pi\, S_e \Omega_e v_{TQ} - \frac{1}{\beta} S_e{}^2 \Omega_e{}^2}{4 v_{TQ}{}^2 + 2 v_P v_{TQ} - v_P{}^2} \right)}_{\substack{\textbf{Engine map:} \\ \text{torque curve at part throttle}}} = \underbrace{\frac{n_{gb,I}{}^2}{\eta_{gb,I}} \frac{\Omega_e}{2a_g} - \sqrt{\left(\frac{n_{gb,I}{}^2}{\eta_{gb,I}} \frac{\Omega_e}{2a_g}\right)^2 - \left(\frac{n_{gb,I}}{\eta_{gb,I}}\right)^2 \frac{P_{g,out}}{a_g}}}_{\substack{\textbf{Engine map:} \\ \text{torque curve at part throttle}}} \tag{116}$$

which, after algebraic manipulation, yields the following characteristic polynomial

$$c_4 \Omega_e{}^4 + c_3 \Omega_e{}^3 + c_2 \Omega_e{}^2 + c_1 \Omega_e + c_0 = 0 \tag{117-a}$$

with coefficients

$$\begin{aligned}
c_4 &= P_{e,\max}{}^2 \frac{S_e{}^6}{\beta^2} \\
c_3 &= -\frac{S_e{}^3 \pi}{a_g \beta} \left(P_{e,\max} n_{gb,I}{}^2 \pi^2 v_P (v_P{}^2 - 2 v_P v_{TQ} - 4 v_{TQ}{}^2) + 4 P_{e,\max}{}^2 S_e{}^2 v_{TQ} a_g \right) \\
c_2 &= \frac{2 S_e{}^2 \pi^2 v_{TQ}}{a_g} \left(P_{e,\max} n_{gb,I}{}^2 \pi^2 v_P (v_P{}^2 - 2 v_P v_{TQ} - 4 v_{TQ}{}^2) - 2 P_{e,\max}{}^2 S_e{}^2 v_{TQ} a_g \right) \quad (117\text{-b}) \\
c_1 &= \frac{4 S_e \pi^3 v_{TQ}{}^2 \beta}{a_g} \left(P_{e,\max} n_{gb,I}{}^2 \pi^2 v_P (v_P{}^2 - 2 v_P v_{TQ} - 4 v_{TQ}{}^2) + 4 P_{e,\max}{}^2 S_e{}^2 v_{TQ} a_g \right) \\
c_0 &= 16\pi^4 P_{e,\max}{}^2 S_e{}^2 v_{TQ}{}^4 \beta^2 + P_{g,out} \frac{n_{gb,I}{}^2 \pi^6 v_P{}^2}{a_g} (v_P{}^2 - 2 v_P v_{TQ} - 4 v_{TQ}{}^2)^2
\end{aligned}$$

The roots of Eq. 116 under WOT conditions ($\beta = 1$) contain the upper and lower engine speeds, $\Omega_{e,\max}$ and $\Omega_{e,\min}$, of the feasible range

$$[\Omega_{e,\min} < \Omega_e < \Omega_{e,\max}] \tag{118}$$

which defines the engine operating speed range for a given load $P_{g,out}$. The TQ_e values over the range (Eq. 117) are then computed from Eq. 114 and the corresponding β values are computed using Eq. 75. Furthermore, Eqs. 71–73 are then utilized to determine $\dot{m}_f$ over the feasible range Eq. 117 and then finally the optimum engine operating point $[\Omega_{eopt}, \beta_{opt}]$ with lowest value of $\dot{m}_f = \dot{m}_{f\,\min}$ is obtained.

Figure 48 shows the engine torque map for a sample matched engine/generator combination for the case with no gearbox between engine and generator (direct drive case) [$SB = 1.0$, $N_{cyl} = 4$, $a_g = 0.25$, $n_{gb,I} = 1.0$, $P_{g,out,\max} = 100\ \text{Hp}$] designed using the procedure shown in Fig. 47. Here, the TQ_e curves at different β settings are plotted in blue, the engine efficiency contours are shown in green, and the generator characteristic curves for constant $P_{g,out}$ are shown in red. For any given $P_{g,out}$, the feasible Ω_e operating range (Eq. 117) is identified by the intersection of the engine WOT torque curve and the generator characteristic curve. Finally, the optimized engine running line for minimum fuel burn rate for the range [$50 \le P_{g,out} \le 100$ Hp] is calculated and overlaid onto Fig. 48 (black dots).

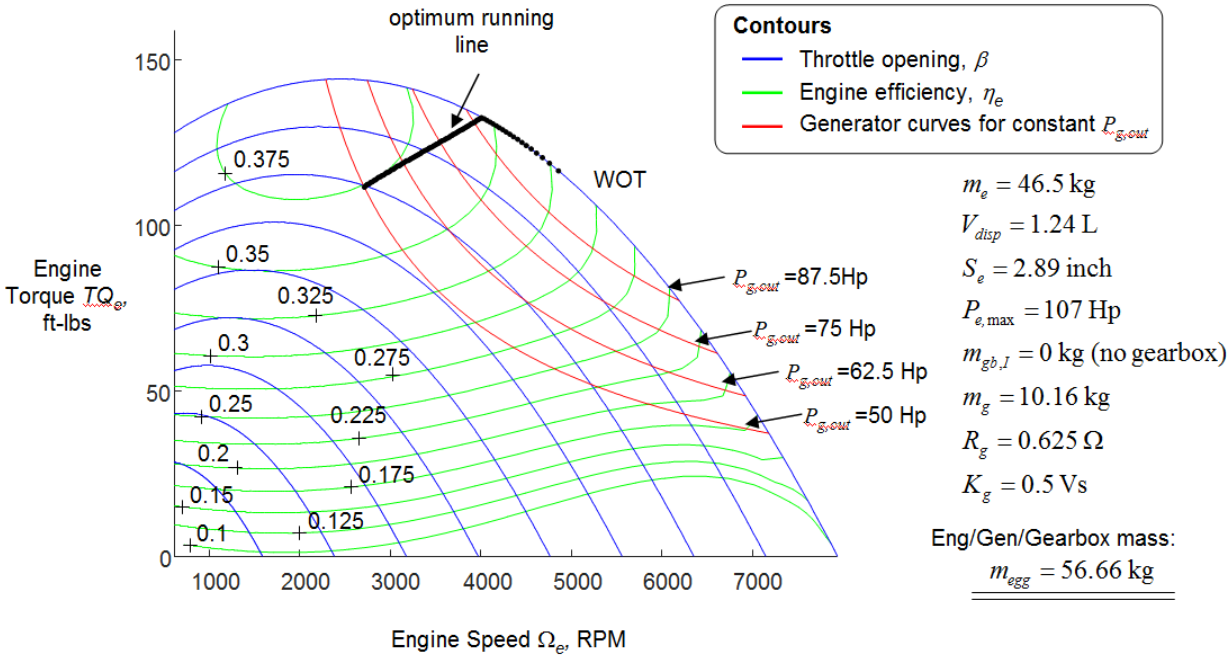

Fig. 48 Characteristic torque-speed curves and optimum running line for the matched engine/generator combination (direct-drive): [$SB = 1.0$, $N_{cyl} = 4$, $a_g = 0.25$, $n_{gb,I} = 1.0$, $P_{g,out,\max} = 100$ Hp]

Figures 49 and 50 illustrate the effect of the gearbox (stage *I*) between engine and generator. Figure 49 shows the matched engine/gearbox/generator design for the case with a reduction gearbox ($n_{gb,I}$ = 0.75) and Fig. 50 shows the case with an overdrive stage ($n_{gb,I}$ = 1.5). Compared to direct-drive, the generator overdrive reduces both the engine and generator mass but also now adds in a non-zero gearbox mass resulting in nearly the same overall mass (m_{egg} = 56.6 kg for direct-drive and m_{egg}= 57.4 kg with overdrive). However, now the advantage of the overdrive is seen by comparing the operating lines in Figs. 48 and 50. It is seen that the overdrive shifts the operating line higher closer toward peak engine efficiency. Conversely, with gear reduction (Fig. 49) the operating line is pushed lower into the less efficient engine operating zone and the system mass is significantly increased (m_{egg} = 72.6 kg with reduction stage and m_{egg}= 56.6 kg with direct-drive). Clearly, the best design is the case with the generator overdrive $n_{gb,I}$ >1.

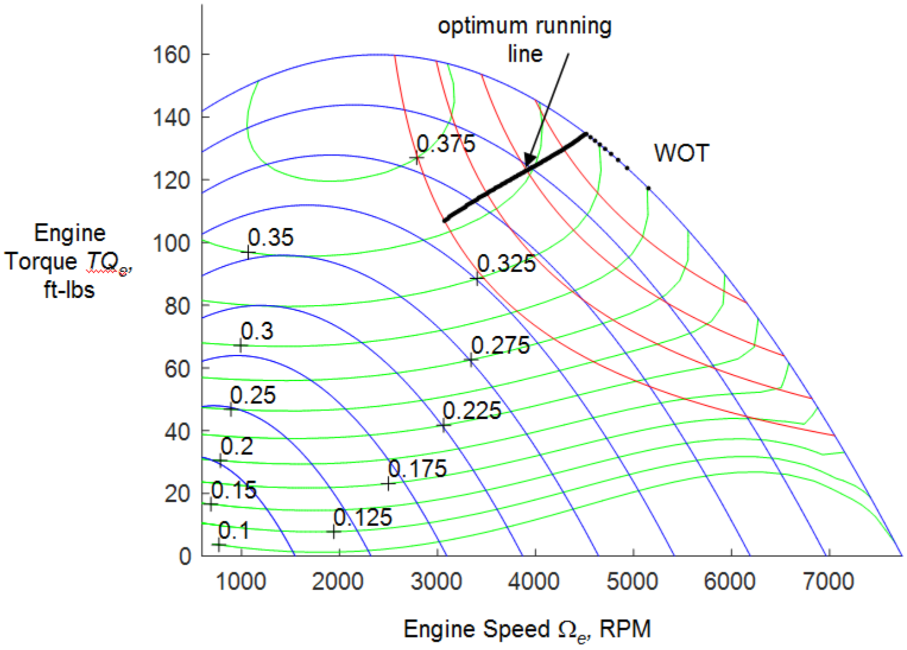

$m_e = 50.30$ kg

$V_{disp} = 1.34$ L

$S_e = 2.96$ inch

$P_{e,\max} = 117$ Hp

$m_{gb,I} = 8.73$ kg

$m_g = 13.65$ kg

$R_g = 0.625\ \Omega$

$K_g = 0.5$ Vs

Eng/Gen/Gearbox mass:

$m_{egg} = 72.68$ kg

Fig. 49 Characteristic torque-speed curves and optimum running line for the matched engine/generator combination (reduction): [SB = 1.0, N_{cyl} = 4, a_g = 0.25, $n_{gb,I}$ = 0.75, $P_{g,out,max}$ = 100 Hp]

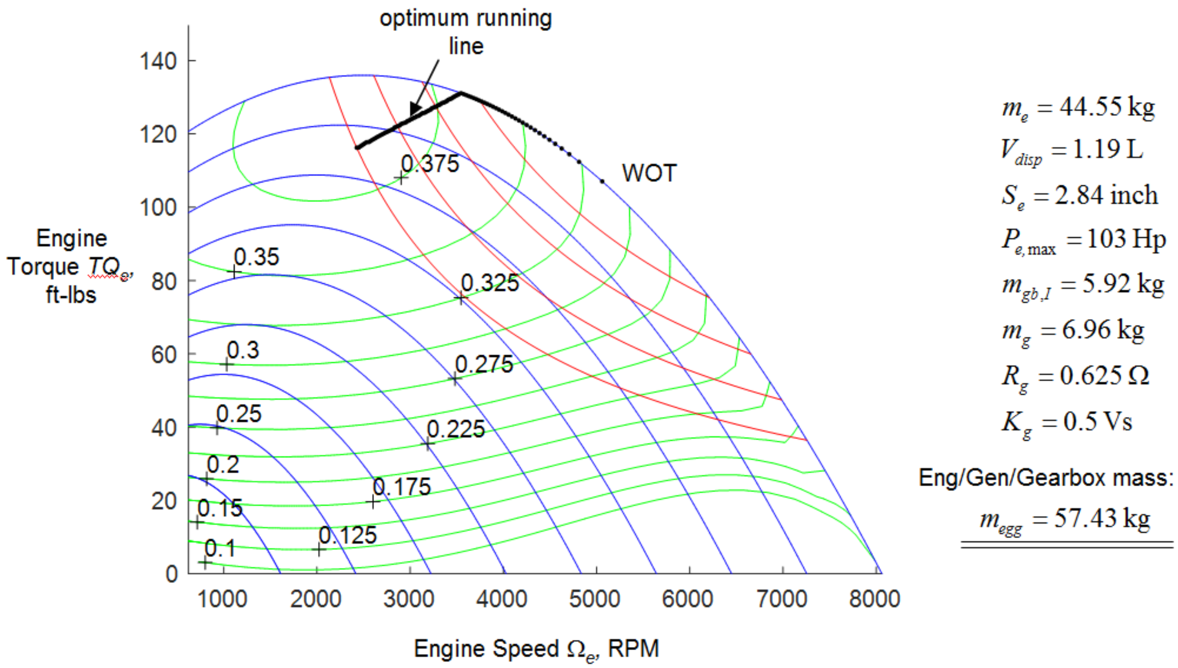

Fig. 50 Characteristic torque-speed curves and optimum running line for the matched engine/generator combination (overdrive): [SB = 1.0, N_{cyl} = 4, a_g = 0.25, $n_{gb,I}$ = 1.5, $P_{g,out,max}$ = 100 Hp]

4.2 Series Gas-Electric Hybrid VTOL UAV Design Results

This section shows the design and performance results obtained by applying the sizing and design code shown in Fig. 43 and described in Section 4.1 for the medium-scale series gas-electric hybrid multirotor VTOL UAV configuration shown in Fig. 43.

Table 6 gives the system parameters used in the design study and analysis. As described in Section 4.1.1, the battery is used to assist the engine during hover conditions as dictated by the battery power fraction γ_{bpf} (Eq. 108). To establish a baseline, the sizing code is first utilized to explore the design space assuming no battery (i.e., $\gamma_{bpf} = 0$). The code is used to generate a family of designs over a range of different initial fuel loads, $W_{f,0}$, maximum payload weights, W_p, and stage I and II gear ratios $n_{gb,I}$ and $n_{gb,II}$.

Table 6 Fixed design parameters for medium-scale series gas-electric hybrid VTOL UAV

Parameter	**Value**	**Parameter**	**Value**
Acceleration of gravity, g	9.81 m/s^2	Gearboxes:	
Air density, ρ	1.225 kg/m^3	Stage efficiencies, $\eta_{gb,I}$ η_{gbII}	0.97
		Gear pressure angle, ϕ	20°
Number of rotors, N_r	[4, 6 & 8]		
Number of blades per rotor, N_b	4	Gear material:	
Blade lift coefficient slope, a_L	5.7	Density, ρ_g	7870 kg/m^3
Blade drag coefficient, C_{d0}	0.008	Elastic modulus, E	200 GPa
Rotor solidity ratio, σ	0.12	Poisson's ratio, ν	0.29
Blade pitch at 3/4 span, θ_{75}	10°	Contact strength, s_{fc}	125,000 psi
Blade tip speed in hover, $v_{t,h}$	550 ft/s		
		Four stroke piston engine:	
Structural mass fraction, f_{sm}	0.25	Stroke over bore ratio, SB	1.0
		Number of cylinders, N_{cyl}	4.0
Motor current constraint, $i_{m,\max}$	400 A	Throttle parameter in hover, β_h	0.95
ESC efficiency, η_{esc}	0.85		
Generator parameter, a_g	0.25 J^{-1}s^{-1}	Li-Po battery cell:	
		Voltage, U_c	3.7 V
Fuel:	43.71 MJ/kg	Resistance, R_c	$6.0 \times 10^{-3}\ \Omega$
Lower heating value, LHV	720 kg/m^3	Charge capacity, Q_c	2200 mAh
Density, ρ_f		Mass per cell, m_c	63.33 g

Figure 51 shows the maximum flight range for the direct-drive case as a function of design payload weight, W_p, for three different design fuel capacities $W_{f,0}$ = [5, 10, and 15 lb]. Note, as before, each point marked on the plots corresponds to a unique design. Also note that, similar to the pure electric and pure gas-powered cases in Sections 2 and 3, the maximum flight range is a function of vehicle forward speed v_v. The range values reported here correspond to the maximum range values achieved at the speed for maximum range, v_{mr}. Next, the effects of the engine/generator gearbox (stage I) and the motor/rotor gearbox (stage II) are evaluated. Figure 52 shows the maximum range achieved for different stage I and II gearbox ratios. As discussed in Section 4.1.13, the stage I gearbox will be overdriving ($n_{gb,I} > 1.0$) and the stage II gearbox will be a reduction stage ($n_{gb,II} < 1.0$). Similar to the results in Sections 2 and 3, Fig. 52 demonstrates that range is significantly extended by use of gearboxes. In particular, these results show that the effect of the stage II gearbox is more significant than stage I and that the optimum $n_{gb,II}$ is approximately 0.2 to 0.3. Furthermore, with $n_{gb,I}$, the benefits are diminishing for $n_{gb,I} > 2.0$. Finally, in Fig. 52, as $n_{gb,II} \rightarrow 1$ the mass dropout effect is observed as the gearbox mass vanishes at the 1:1 direct-drive condition.

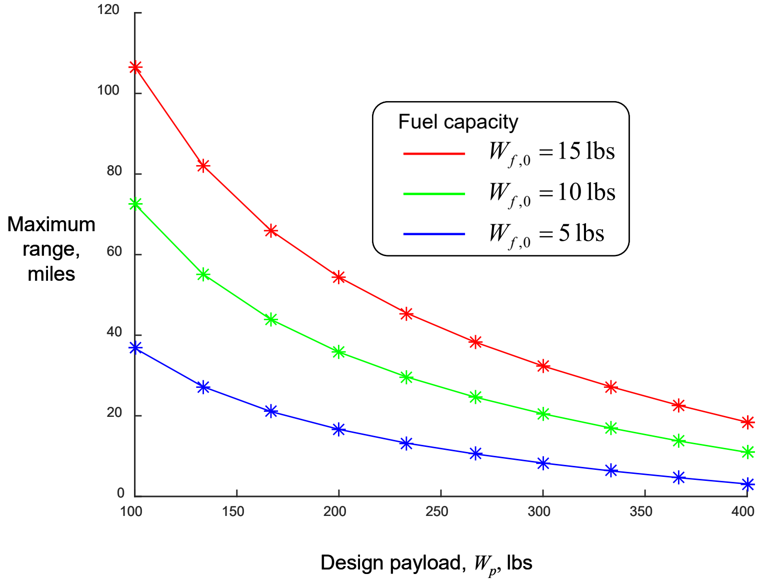

Fig. 51 **Series gas-electric hybrid quadrotor maximum range vs. design payload: $n_{gb,I} = 1$, $n_{gb,II} = 1$, (direct-drive), $\gamma_{bpf} = 0$**

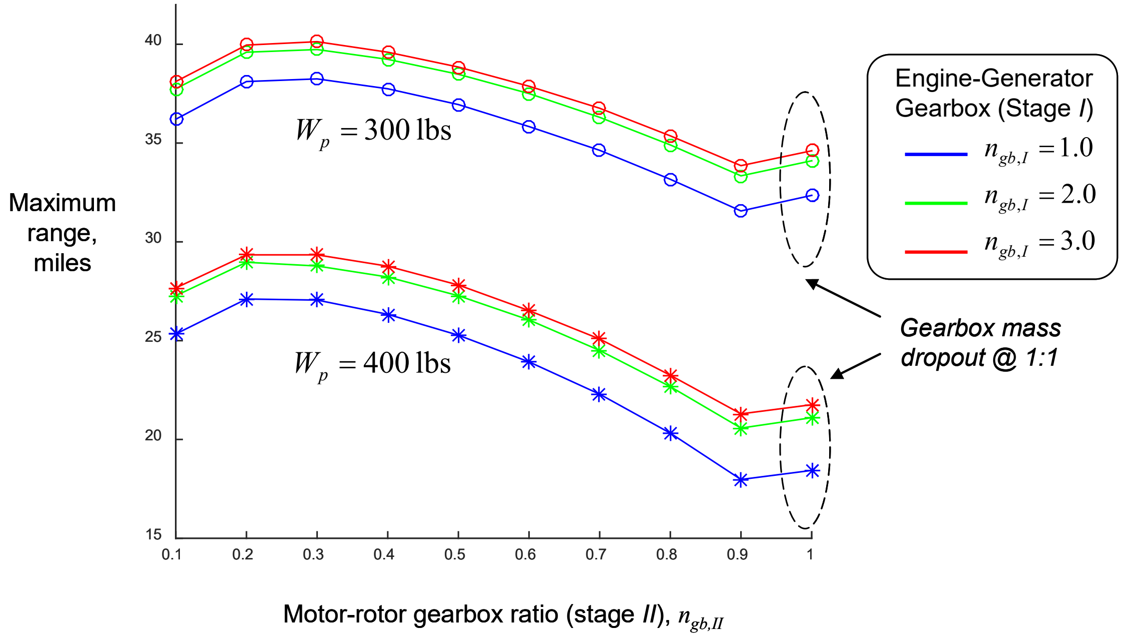

Fig. 52 **Series gas-electric hybrid quadrotor maximum range for $n_{gb,I}$ and $n_{gb,II}$ combinations; $W_{f,0} = 15$ lb, W_p = [300 and 400 lb], $\gamma_{bpf} = 0$**

The gearbox ratio effects are further illustrated in Fig. 53, which shows the baseline direct-drive case plotted together with the near optimum ratio case [$n_{gb,I} = 2.0$, $n_{gb,II} = 0.3$]. For each of the three fuel capacities considered, $W_{f,0}$ = [5, 10, and 15 lb], this figure shows that the range-extending benefit of the gearboxes becomes more significant at higher payload levels, W_p.

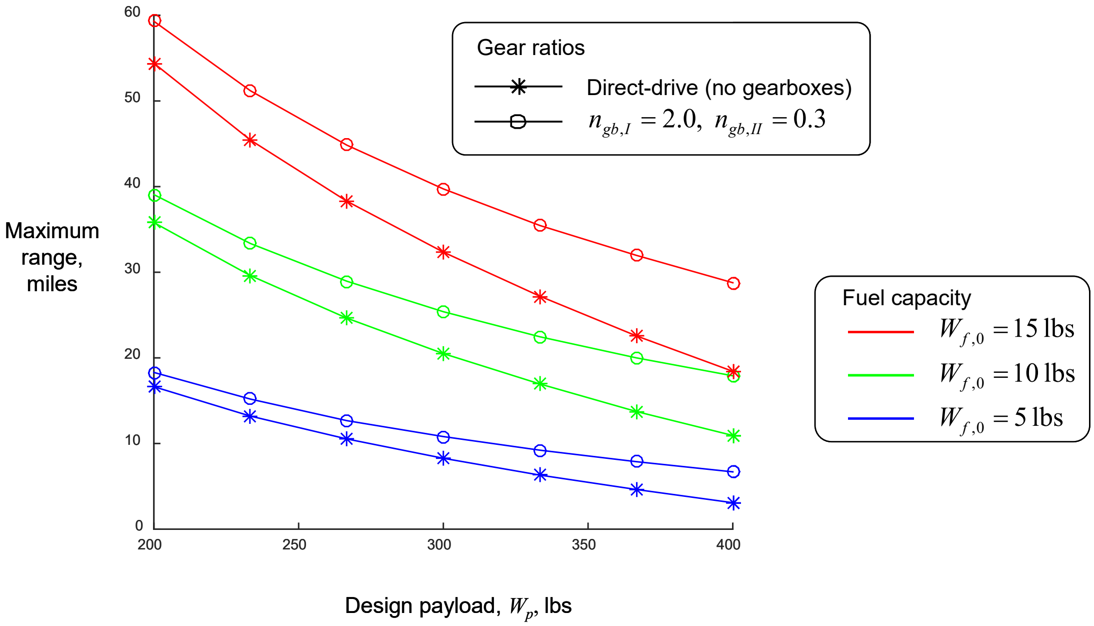

Fig. 53 Series gas-electric hybrid quadrotor maximum range vs. design payload for direct-drive and near optimum gear ratio cases; $\gamma_{bpf} = 0$

Furthermore, Fig. 54 shows the effect of fuel capacity on maximum flight range at four different maximum design payloads W_p = [100, 200, 300, and 400 lb] for direct-drive and the near optimum gear ratio case [$n_{gb,I} = 2.0$, $n_{gb,II} = 0.3$]. In agreement with intuition, increasing onboard fuel capacity results in an increased flight range. The curves are slightly nonlinear with diminishing range increases at higher fuel levels. However, over the range of values considered in this study (i.e., the medium scale), the range-fuel curves are not close to saturating. Hence, the medium-scale series gas-electric hybrid quadrotor, like the pure IC engine-powered case in Section 3, are both very scalable by straightforward increases in onboard fuel capacity (see Figs. 39 and 54). This is in sharp contrast to the medium-scale battery-electric-powered quadrotor configuration, where the range-battery weight curves show peak values with decreasing flight ranges for larger batteries beyond the peak (see Fig. 14).

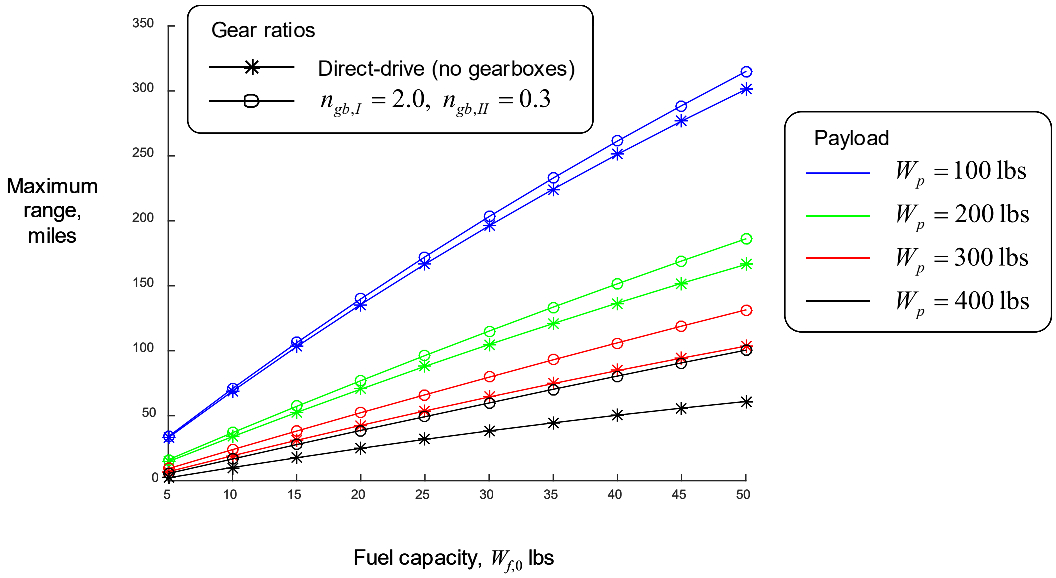

Fig. 54 Series gas-electric hybrid quadrotor maximum range vs. fuel capacity for direct-drive and near optimum gear ratio cases; $\gamma_{bpf} = 0$

Figures 55–59 give more details of the system design and performance. Here again, two design families of series hybrid gas-electric quadrotor are evaluated (one direct-drive and the other with [$n_{gb,I}$ = 2.0, $n_{gb,II}$ = 0.3]). Figure 55a shows the maximum flight range, Fig. 55b shows the engine output power, P_e, during hover, Fig. 55c shows the rotor diameter, Fig. 55d gives the engine displacement volume, V_{disp}, Fig. 55e shows Ω_e and Ω_r during hover, and Fig. 55f shows the values of i_g and i_m also during hover.

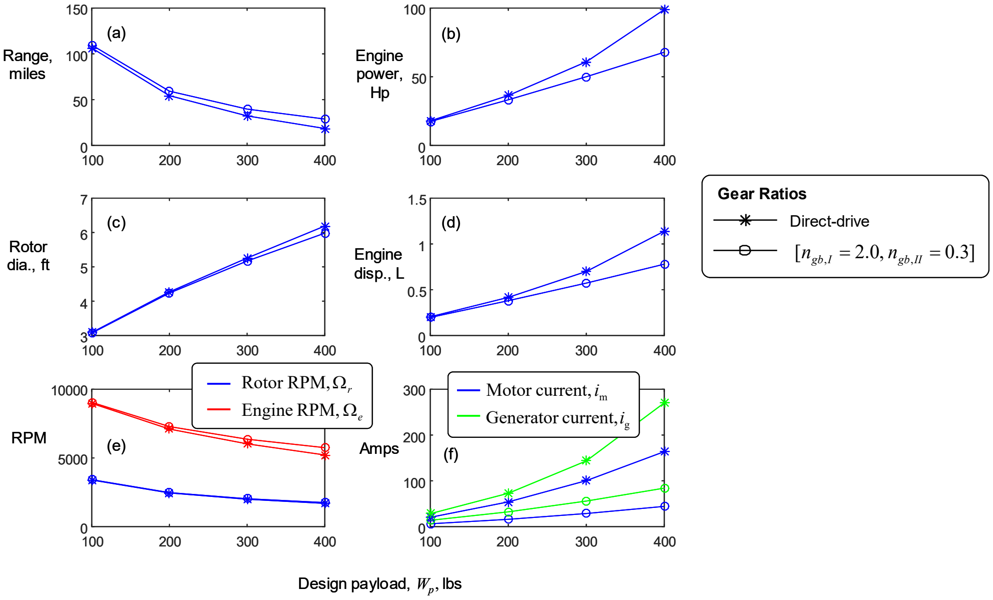

Fig. 55 Series gas-electric hybrid quadrotor design results and performance vs. design payload for direct-drive and near optimum gear ratio cases: $W_{f,0}$ = 15 lb, $\gamma_{bpf} = 0$

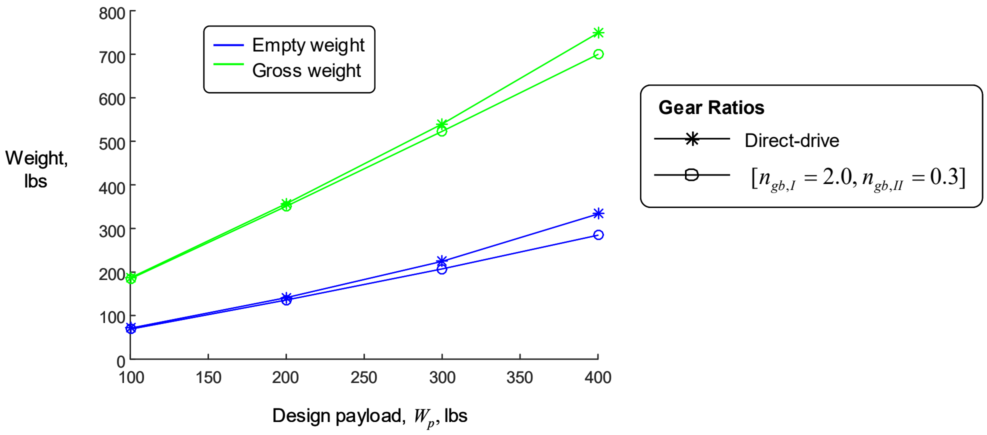

Fig. 56 Series gas-electric hybrid quadrotor design results and performance vs. design payload for direct-drive and near optimum gear ratio cases: $W_{f,0}$ = 15 lb, γ_{bpf}=0

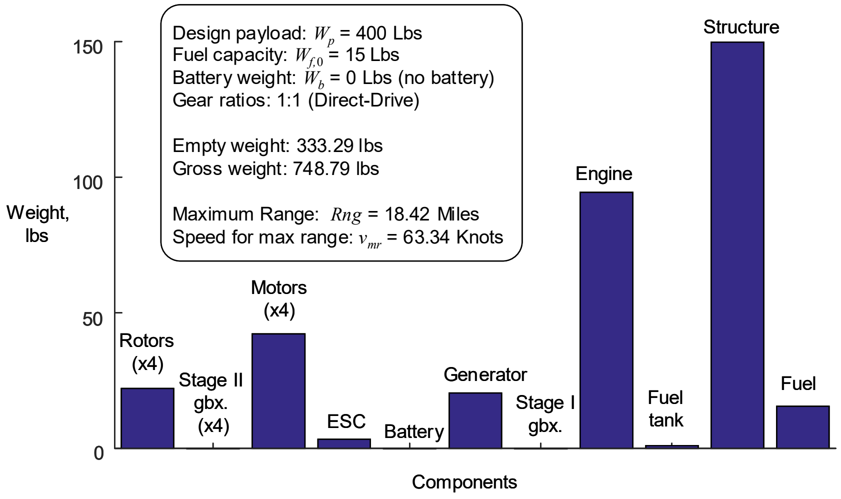

Fig. 57 Series gas-electric hybrid quadrotor component weights for direct-drive design: W_p = 400 lb, $W_{f,0}$ = 15 lb, γ_{bpf} = 0

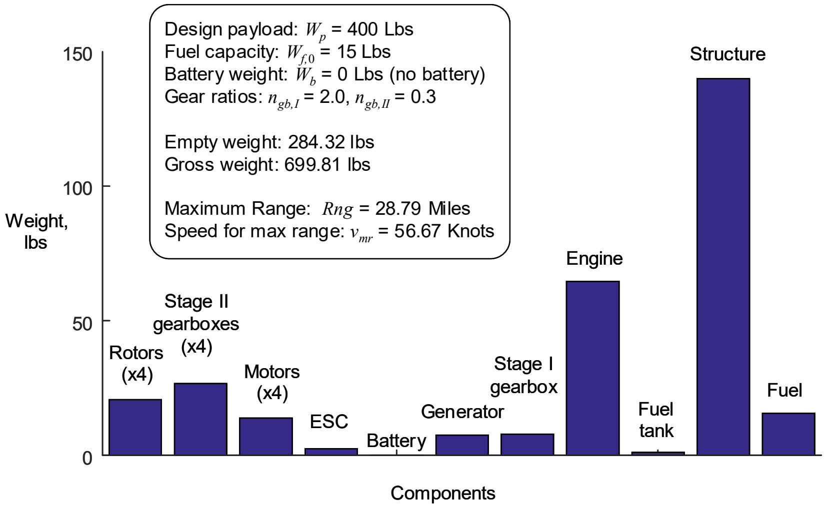

Fig. 58 Series gas-electric hybrid quadrotor component weights for near-optimum gear ratio design: W_p = 400 lb, $W_{f,0}$ = 15 lb, γ_{bpf} =0

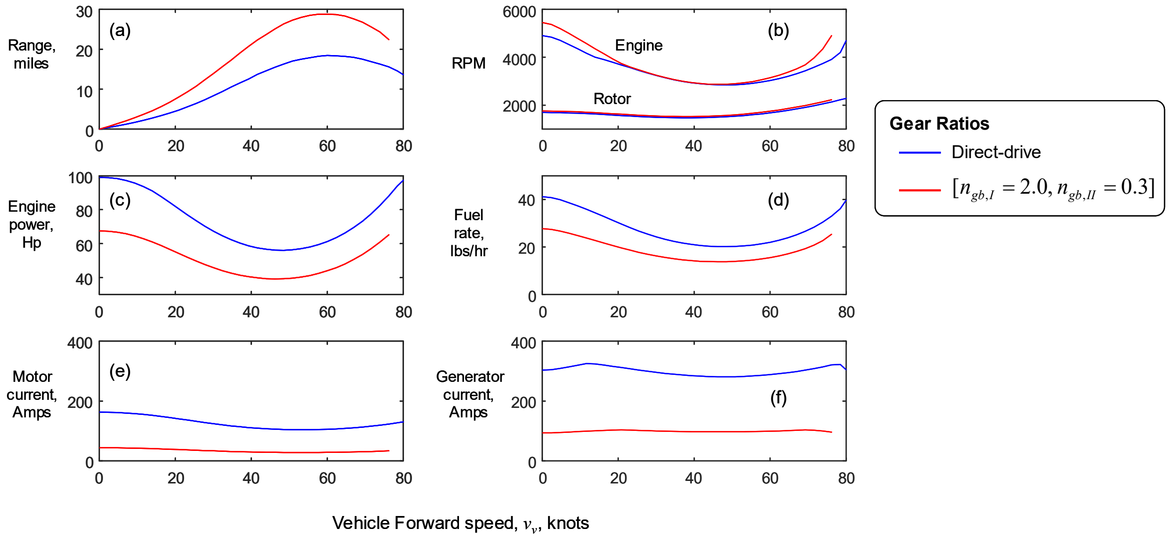

Fig. 59 Series gas-electric hybrid quadrotor forward flight performance vs. vehicle forward speed for direct-drive and near-optimum gear ratio designs: W_p = 400 lb, $W_{f,0}$ = 15 lb, γ_{bpf} = 0

It is observed that the main difference between direct-drive and the near-optimum gear ratio design families is that, at higher payload levels, direct-drive requires a larger engine with more engine power in order to drive the larger i_g and i_m currents through the generator and motors.

Figure 56 shows the resulting empty and gross vehicle weights for the direct-drive and the near optimum gear ratio series gas-electric hybrid quadrotor designs. Furthermore, Figs. 57 and 58 show the component weights of each subsystem for cases with design payload of W_p = 400 lb. For both hybrid gas-electric quadrotor design families presented here it is noted that the fuel weight ($W_{f,0}$ = 15 lb) is on the order of 5% of the vehicle empty weight. As seen in Figs. 57 and 58, the reduced engine weight in near-optimum gear ratio design is offset by the added weight of the gearboxes. As a result, as seen in Fig. 56, empty and gross vehicle weights for the direct-drive and near optimum gear ratio designs are similar over the entire range of payloads. However, at the higher payload levels (W_p > 300 lb) the flight range of the near-optimum gear ratio design is significantly improved compared with direct-drive (28 miles versus 18 miles with W_p = 400 lb as shown in Fig. 53). At lower payload levels (W_p < 200 lb) the range-extending benefits of the gearboxes are less significant and direct-drive may be the better design choice due to lower complexity and reduced part count. Finally, Fig. 59 shows the forward flight performance of the series gas-electric hybrid quadrotor designs for the case with W_p = 400 lb and $W_{f,0}$ = 15 lb.

Figures 59a and 59c demonstrate the forward flight "power bucket" phenomena, which is where the optimum forward speed for maximum range ($v_{mr} \cong 60$ knots) occurs while the maximum power demands occur at low speeds and in hover. Furthermore, it is also observed in Fig. 59b how the engine and rotor speeds, Ω_e and Ω_r, vary independently due to the lack of direct mechanical connection in the series hybrid gas-electric arrangement. The engine is allowed to find the best operating point depending on the load. Furthermore, for the fixed-pitch rotors, Ω_r is adjusted by the variable rotor RPM flight control to maintain trim in steady flight. To compare the hybrid system to a pure IC engine-powered case with direct mechanical engine/rotor connection, it is interesting to observe the virtual gear ratio (see Fig. 60) by plotting Ω_r/Ω_e from Fig. 59b. Figure 60 shows that at low flight speeds approaching hover the most virtual reduction occurs ($\Omega_r / \Omega_e \cong 0.3$) while at the most efficient cruising speed, v_{mr} , this ratio climbs to about $\Omega_r / \Omega_e \cong 0.6$. In essence, the motor/generator arrangement in the hybrid system is functioning as a virtual continuously variable transmission (CVT).

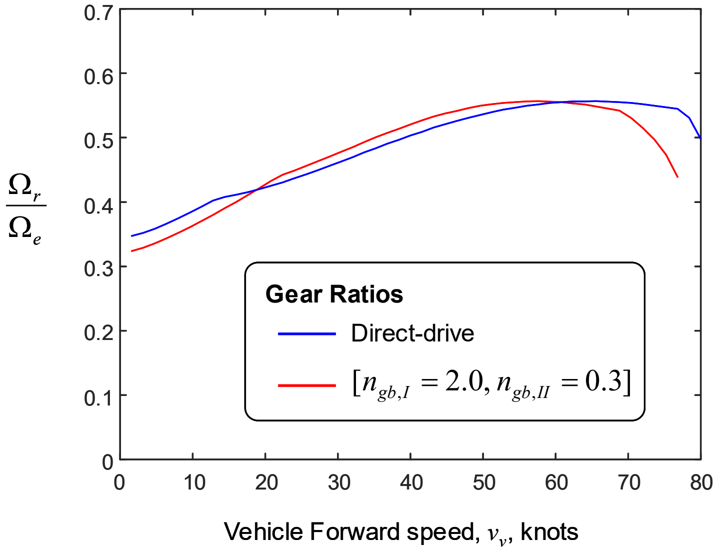

Fig. 60 Series gas-electric hybrid quadrotor virtual gear ratio vs. vehicle forward speed for direct-drive and near-optimum gear ratio designs: $W_p = 400$ lb, $W_{f,0} = 15$ lb, $\gamma_{bpf} = 0$

Next, the effect of additional rotors is explored. Thus far in this report, all of the results presented have been for quadrotor ($N_r = 4$) configurations. The gas-powered designs presented in Section 3 were especially restricted to $N_r = 4$ due to their multistage H- and X-type mechanical transmission systems. In the case of battery-electric and serial gas-electric hybrid configurations, the number of rotors can be much more easily increased due to the lack of mechanical connections.

Figure 61 shows the maximum fight range versus design payload for the baseline quadrotor configuration ($N_r = 4$) and an octorotor configuration ($N_r = 8$). Both designs are direct-drive (no gearboxes) and the results are for three different design fuel capacities, $W_{f,0}$ = [5, 10, and 15 lb]. This figure shows that increasing the number of rotors from four to eight increases the flight range for the same amount of fuel. Furthermore, this range increase is more significant at the higher payload levels $W_p > 300$ lb. The effect of adding more rotors appears almost identical to the effect of adding gearboxes (see Fig. 53). Next, Fig. 62 shows the combined effect of increasing the number of rotors and including the stage I and II gearboxes.

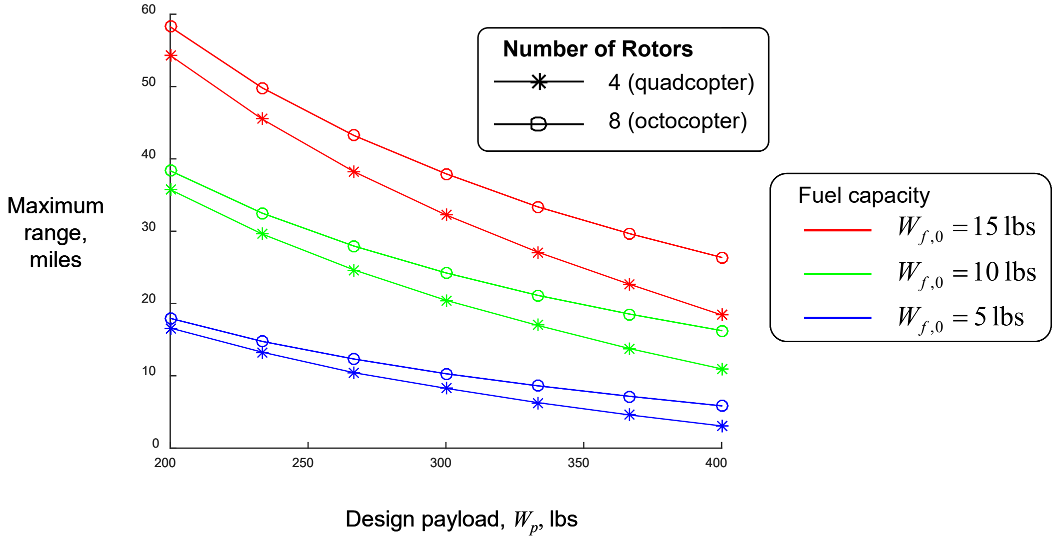

Fig. 61 Maximum range vs. payload for the series gas-electric hybrid quadrotor ($N_r = 4$) and octorotor ($N_r = 8$) configurations with direct-drive: $W_{f,0}$ = [5, 10, and 15 lb] and $\gamma_{bpf} = 0$

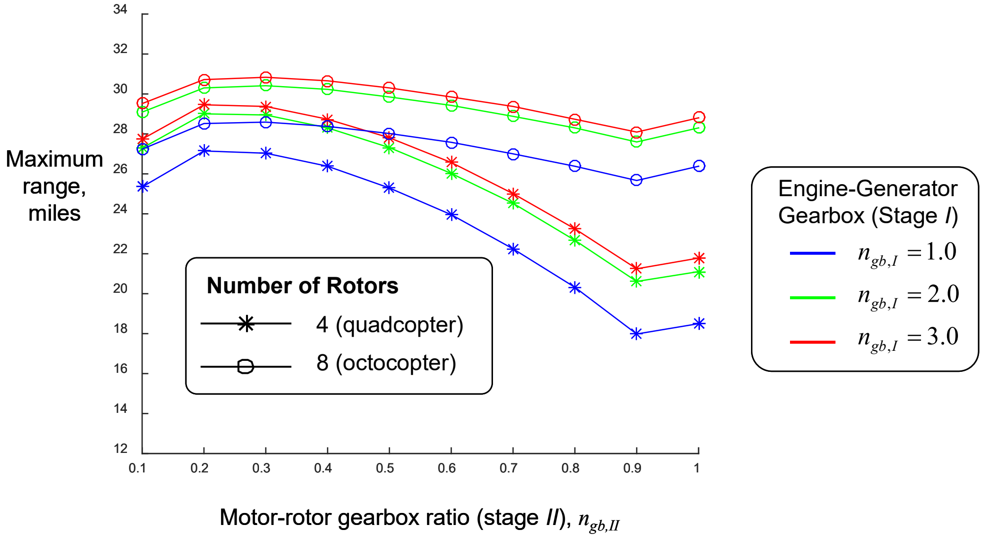

Fig. 62 Maximum range for the series gas-electric hybrid quadrotor ($N_r = 4$) and octorotor ($N_r = 8$) configurations for different $n_{gb,I}$ and $n_{gb,II}$ combinations: $W_{f,0} = 15$ lb, $W_p = 400$ lb, and $\gamma_{bpf} = 0$

It is seen that the range increases gained by incorporating gearboxes into the octorotor design is not as dramatic as it is for the quadrotor configuration. From a practical point of view, it appears that the best design choice for the medium-scale octorotor would be direct-drive. For the hexacopter (N_r = 6) (not shown) and quadrotor the best design choice would include gearboxes.

Figure 63 shows that both the empty and gross vehicle weights are slightly lower for the direct-drive octorotor designs. Figure 64a shows the maximum flight range,

Fig. 64b shows the engine output power, P_e, during hover, Fig. 64c shows the rotor diameter, Fig. 64d gives the engine displacement volume, V_{disp}, Fig. 64e shows Ω_e and Ω_r during hover, and Fig. 64f shows the values of i_g and i_m, also during hover. The main difference due to the increased number of rotors is that the rotor diameter becomes smaller, as can be seen in Fig 64c.

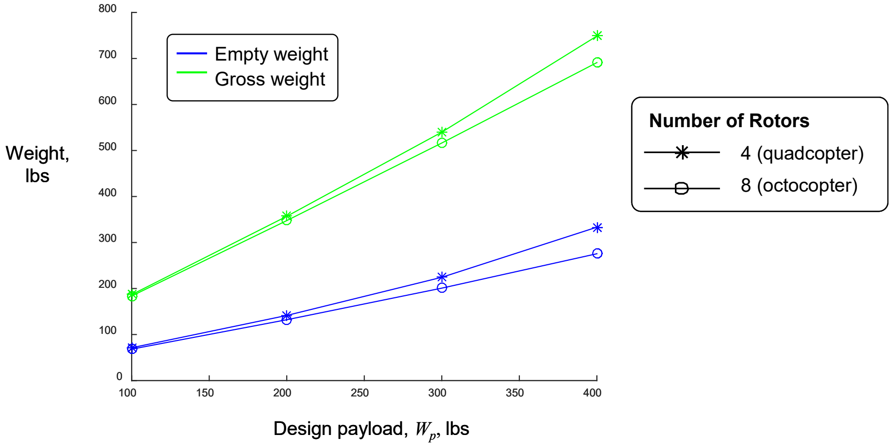

Fig. 63 **Series gas-electric hybrid quadrotor and octorotor empty and gross vehicle weights vs. design payload for direct-drive: $W_{f,0}$ = 15 lb and γ_{bpf} = 0**

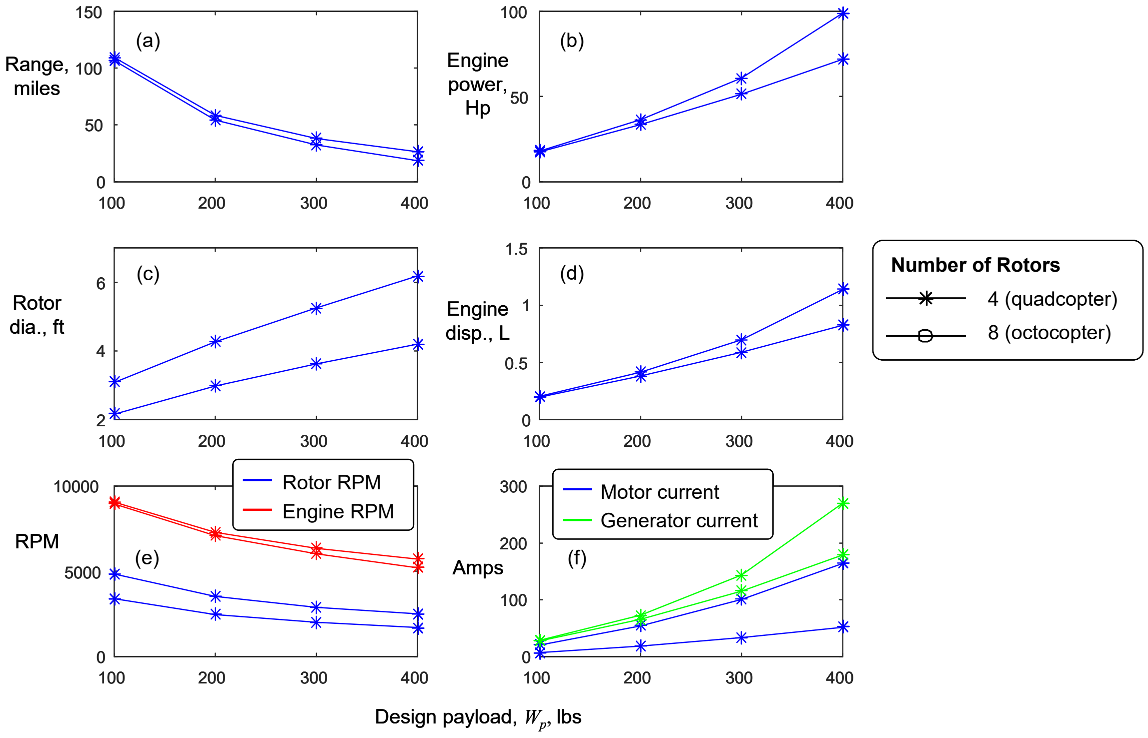

Fig. 64 **Series gas-electric hybrid quadrotor and octorotor design results and performance comparison vs. design payload for direct-drive: $W_{f,0}$ = 15 lb and γ_{bpf} = 0**

Next, the design and operational concept of battery-assisted hover will be explored. Recalling Eqs. 106–108, the concept of battery power fraction γ_{bpf} is introduced. The battery-assisted hover concept is outlined further in Fig. 65, which shows a notional plot of total power that must be supplied to the motors for hover and forward cruise. During hover, the combined power from both the engine and battery are used. During cruise, only engine power is used. By including γ_{bpf} in the design, this concept attempts to take advantage of the "power bucket" phenomenon whereby the engine and generator are sized for the lower cruise power levels, which will result in a lighter weight engine and generator. The hover-assist battery will then be sized to supply the extra power during hover. However, the battery size must also account for the desired hover endurance time, t_h, since now it will not be possible to sustain hover without battery assistance. It is hoped that the weight savings from the engine and generator will be greater than the added weight of the hover-assist battery in order to yield flight range gains over the baseline ($\gamma_{bpf} = 0$) serial gas-electric hybrid designs with no battery presented in Figs. 51–64.

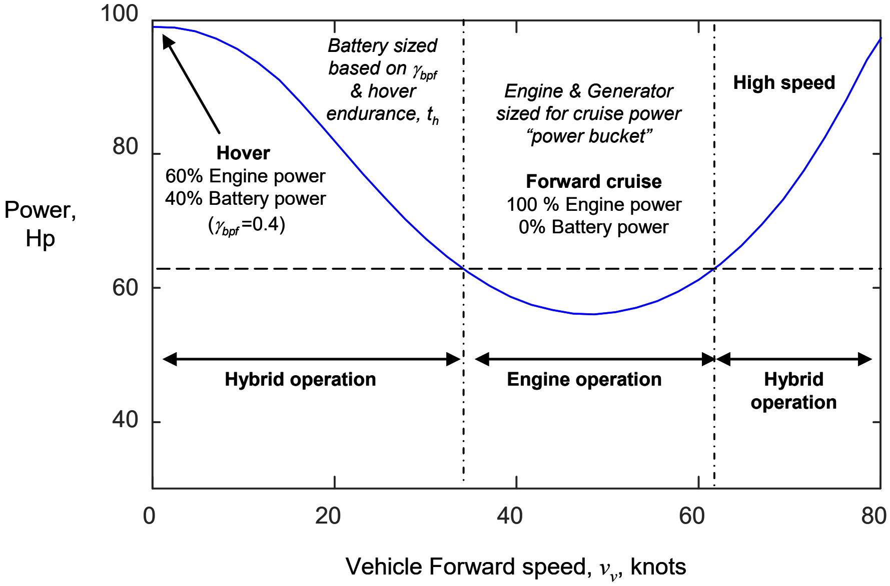

Fig. 65 Notional power vs. forward speed plot illustrating the battery-assisted hover concept

Figures 66–69 show the design results including battery-assisted hover [$0 < \gamma_{bpf} < 1$] for the medium-scale series gas-electric hybrid quadrotor UAV with direct-direct drive (i.e., $n_{gb,I} = n_{gb,II} = 1$ and $m_{gb,I} = m_{gb,II} = 0$). As before, each point on plots represents a unique design. In particular, Fig. 66 shows the maximum flight range as a function of γ_{bpf} for the three different hover endurance times t_h = [6, 9, and 12] minutes for a case with design payload W_p = 400 lb and fuel capacity $W_{f,0}$ =15 lb.

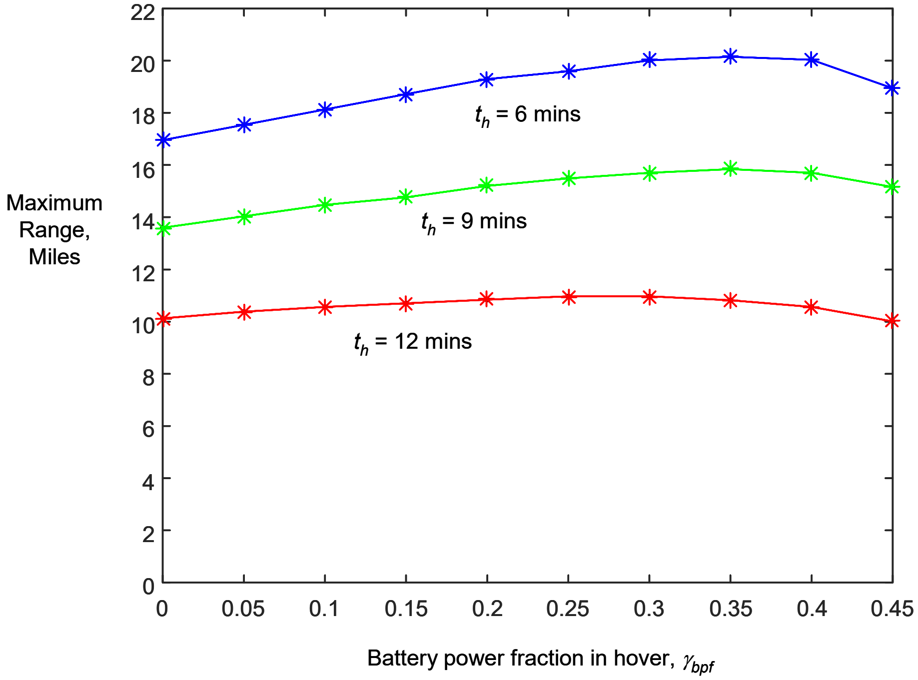

Fig. 66 **Maximum flight range vs. battery power fraction in hover γ_{bpf} for the series gas-electric hybrid quadrotor with direct-drive for t_h = [6, 9, and 12] min; $W_{f,0}$ = 15 lb and W_p = 400 lb**

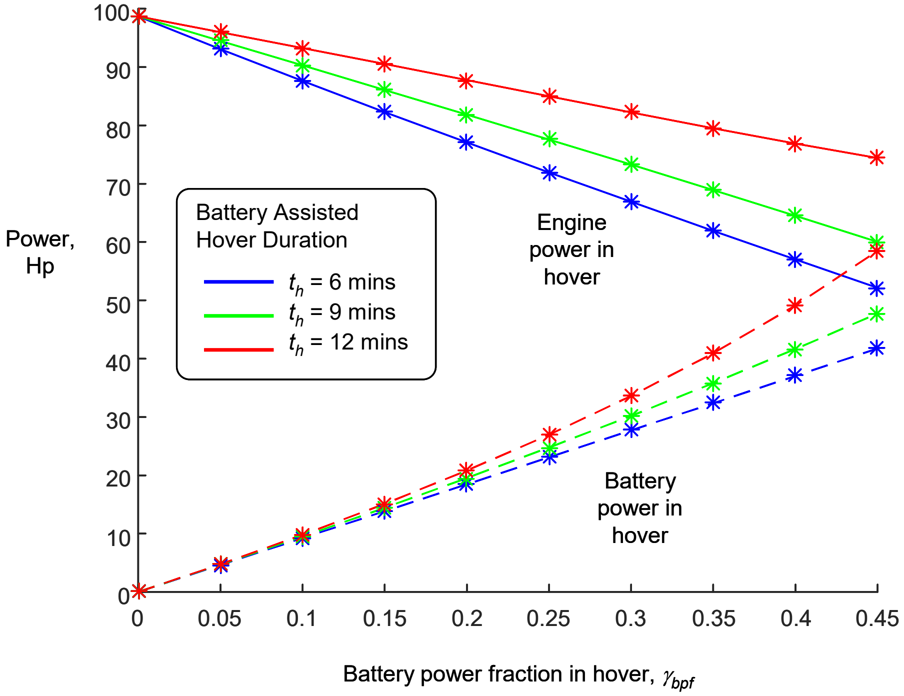

Fig. 67 **Engine and battery power during hover vs. battery power fraction γ_{bpf} for the series gas-electric hybrid quadrotor with direct-drive for t_h = [6, 9, and 12] mins; $W_{f,0}$ = 15 lb, W_p = 400 lb**

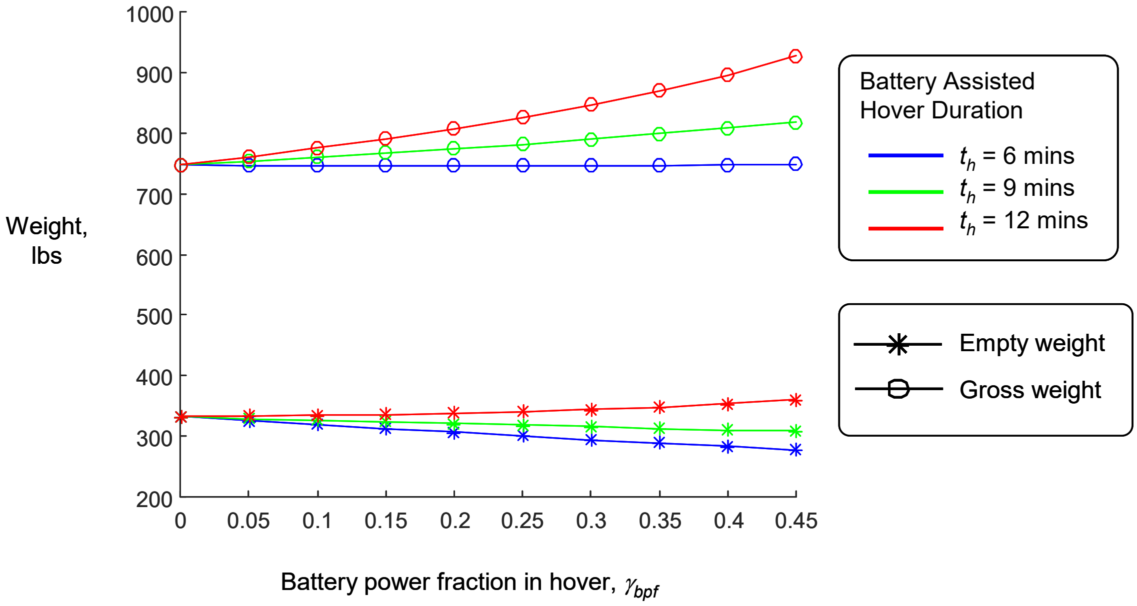

Fig. 68 **Empty and gross vehicle weights vs. battery power fraction γ_{bpf} for the series gas-electric hybrid quadrotor with direct-drive for t_h = [6, 9, and 12] min; $W_{f,0}$ = 15 lb, W_p = 400 lb**

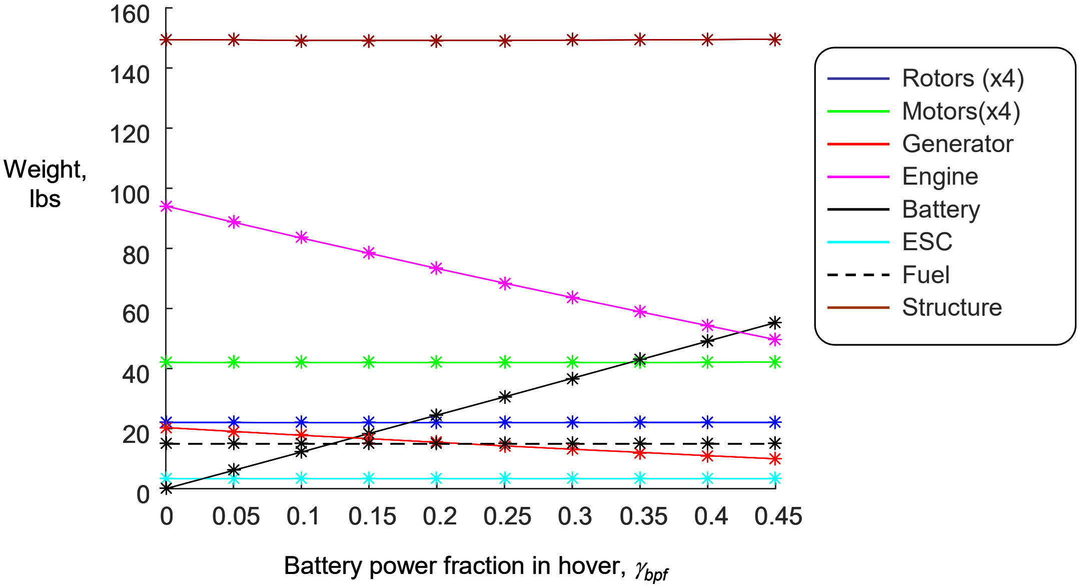

Fig. 69 **Maximum flight range vs. battery power fraction in hover γ_{bpf} for the series gas-electric hybrid quadrotor with direct-drive for t_h = [6, 9, and 12] min; $W_{f,0}$ = 15 lb, W_p = 400 lb**

Here, it is seen that only minor range benefits are gained from the inclusion of the hover assist battery in the design. Note also that the overall range decreases with increasing hover endurance times, t_h. This effect is due to two factors: 1) the fuel burned off during hover reduces the amount left for forward flight, and 2) larger values of t_h require larger batteries with increased W_b affecting overall system weight.

Furthermore, Fig. 67 shows the corresponding power outputs from the engine and battery, P_e and P_b, during hover. This figure shows that, as to be expected, P_e decreases as P_b increases with γ_{bpf}. Note again that the overall power levels are higher for the larger t_h values due to the overall increase in system mass, which is plotted in Fig. 68. Figure 68 shows that for $t_h = 6$ minutes, the gross vehicle weight is nearly constant across the range of γ_{bpf}. In other words, for designs with $t_h = 6$ minutes, the decrease in engine and generator weight is almost identical to the added battery weight. When $t_h = 9$ and 12 minutes, the gross vehicle weight actually rises with γ_{bpf}.

Figure 69 shows how the mass of each component varies with γ_{bpf} for the case $t_h =$ 6 minutes. This figure shows that as battery weight increases both engine and generator weights decrease.

5. Performance Comparisons

This section explores and compares the performance of the battery-electric, IC engine-powered and series gas-electric hybrid quadrotor configurations designed based on Sections 2, 3, and 4.

Table 7 gives a summary of each of the three different configuration designs that are evaluated. In order to have the comparisons be as fair as possible, the best design for each configuration with respect to maximum flight range is utilized in this study (Table 7).

Table 7 Medium-scale quadrotor UAV designs

Configuration	Description
Battery-electric quadrotor	See Fig. 2 and Table 2 Gear ratio: $n_{gb} = 0.2$ (5:1) Design process: Fig. 3
IC engine-powered quadrotor	See Fig. 23 and Table 5 Transmission: X-type with n optimized as shown in Section 3.1.5 Design process: Fig. 24
Series gas-electric hybrid quadrotor	See Fig. 42 and Table 6 Stage I and II gear ratios: $n_{gb,I} = 2.0$, $n_{gb,II} = 0.3$ Design process: Fig. 43

Each configuration is studied under full and partial payload conditions and their performance is also evaluated for a payload drop-off mission scenario. The partial payload condition is important because it shows how sensitive or robust a given design is to off-nominal operating conditions. In particular, the partial payload case is important since any given design may not always be carrying its full design payload.

The operational flexibility and scalability of the electric, gas, and hybrid gas-electric configurations are demonstrated in Figs. 70 and 71. Figure 70a shows the maximum range as a function of actual payload, which is different from the design payload (W_p = 400 lb in this case). Furthermore, Fig. 70b shows the corresponding optimum vehicle forward speeds for the maximum range. In addition, Fig. 71 illustrates the degree to which the flight range scales with onboard energy supply (i.e., fuel or battery).

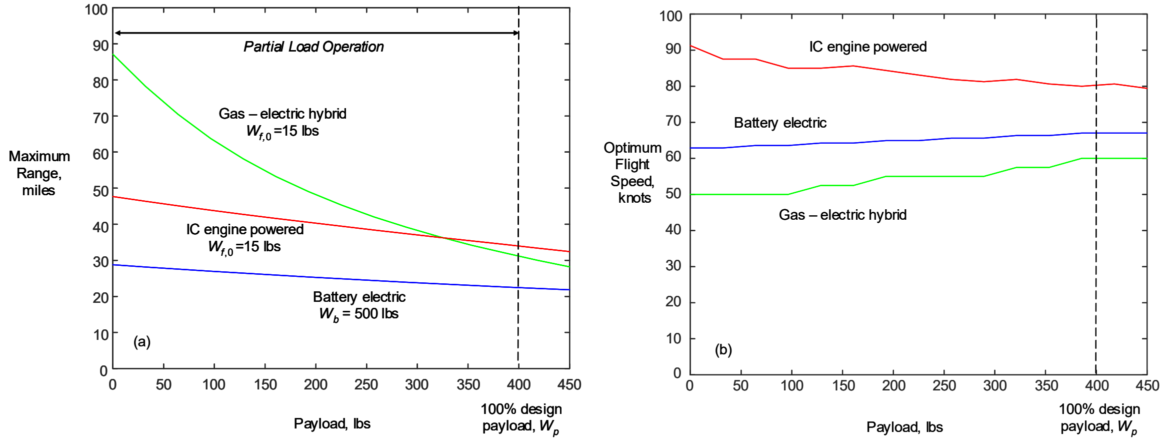

Fig. 70 Maximum flight range and optimum flight speeds during partial payload operation for design payload W_p = 400 lb

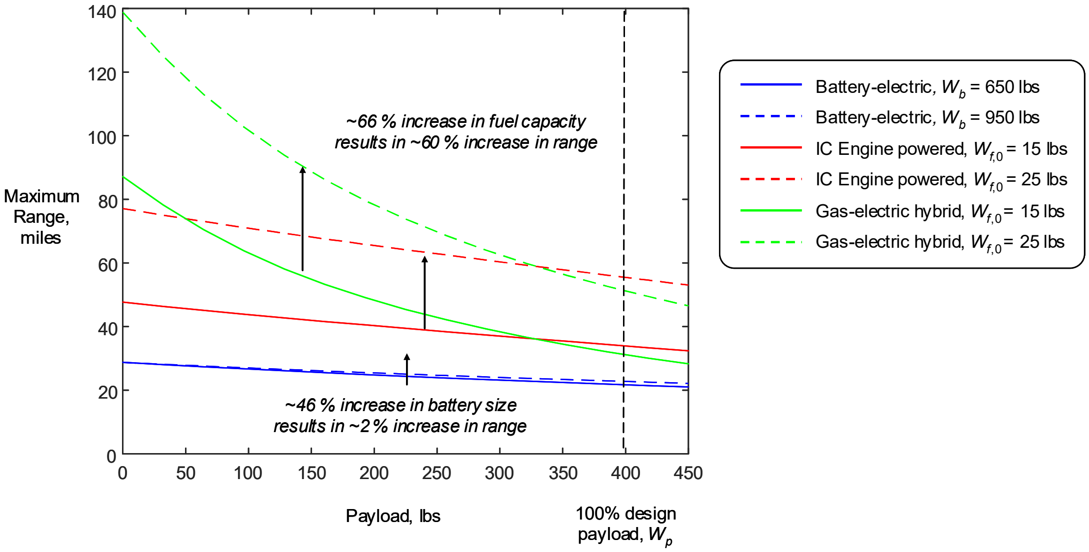

Fig. 71 Flight range scalability with onboard energy supply; design payload W_p = 400 lb

Results from Figs. 70 and 71 illustrate several key characteristics and differences summarized as follows:

1) When operating at full 100% design payload level:
    - The pure IC engine-powered quadrotor has the longest range and has the highest speed.
    - The gas-electric hybrid quadrotor has similar range to the pure IC engine-powered case; however, it operates with the slowest flight speed.
    - The battery-electric design has the lowest range but the flight speed is slightly higher than the hybrid design.
2) When operating with reduced partial payloads:
    - The gas-electric hybrid system offers, by far, the most operational flexibility allowing the engine/generator/motor system to find the most efficient operating point at each payload level resulting in significantly higher flight ranges at partial payloads compared with the pure IC engine and battery-electric configurations. This is partially due to the fact that, as discussed with Fig. 60, the lack of engine rotor mechanical connection enables the system to function as a virtual CVT.
3) Range scalability with onboard energy supply (Fig. 71):
    - Flight range scales almost linearly with onboard fuel supply for both the IC engine-powered and the gas-electric hybrid configurations.
    - In the battery-electric configuration, flight range does not scale linearly with battery size. At the medium scales investigated, maximum flight range saturates at about 25 to 30 miles.

In addition to the simple range metric used throughout this study whereby the payload is assumed constant during the entire flight duration, another important mission scenario is the payload drop-off mission.

Figure 72 shows a schematic of the payload drop-off mission in which the vehicle flies out to a drop-off location with full design payload, W_p, drops-off the payload and then returns to the start location with no payload ($W_p = 0$). For a given W_p, the performance metric is the maximum drop-off range, r_{do}, which is the distance from the start location to the drop-off point.

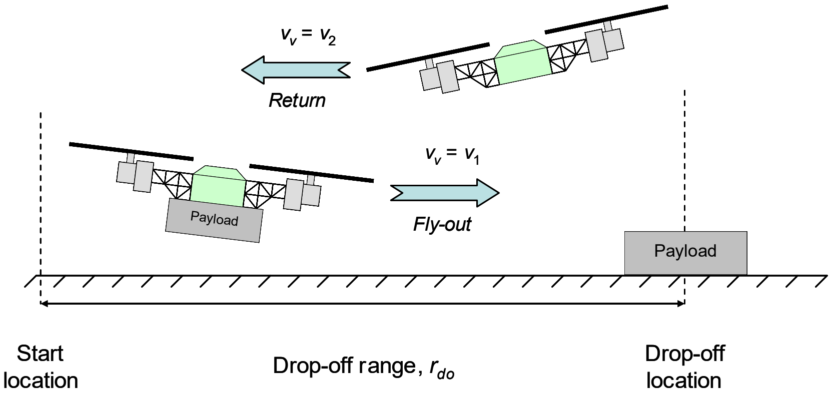

Fig. 72 Payload drop-off mission scenario

Figure 73 shows the maximum drop-off radius and optimum forward speeds for the battery-electric quadrotor as a function of battery weight at two different design payload levels: W_p = 100 and 400 lb. Figure 73a again illustrates the range saturation phenomena that occurs with the battery-electric designs and Fig. 73b shows that the optimal speed during the payload fly-out leg is different than the return speed. Figure 74 shows a comparison of the payload drop-off ranges for all three configurations and the corresponding optimum forward speeds as a function of design payload. Finally, Fig. 75 shows the payload drop-off range for a fixed design payload of W_p = 400 lb as a function of actual payload (partial payload). Also shown on Fig. 75 are the corresponding vehicle empty weights and rotor diameters for each design.

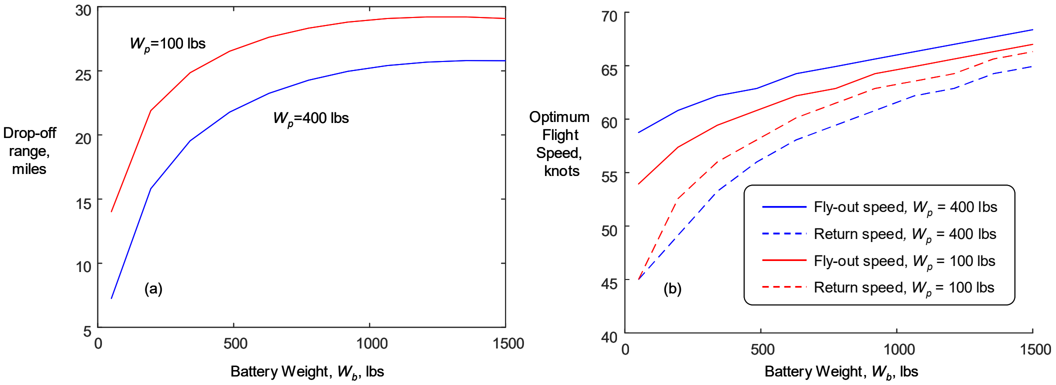

Fig. 73 Payload drop-off mission range and flight speeds vs. battery weight for the battery-electric quadrotor configuration, n_{gb} = 0.2

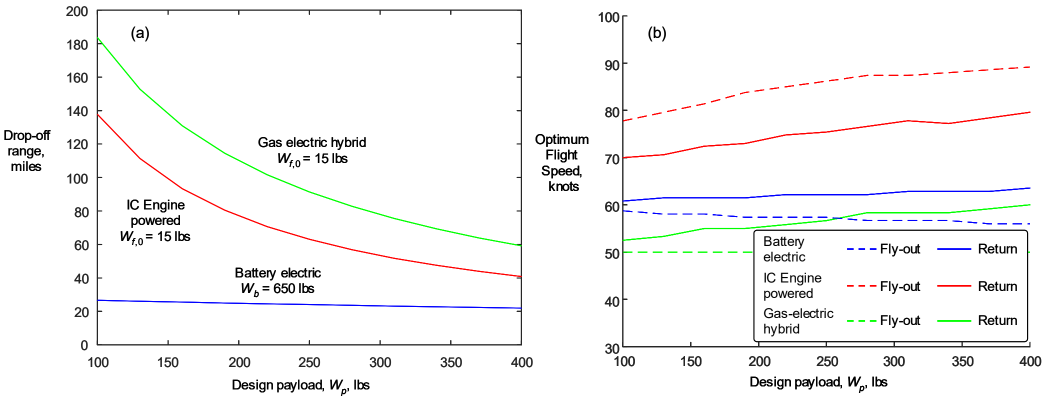

Fig. 74 Payload drop-off mission range and flight speeds vs. design payload weight for the battery-electric, IC engine-powered and gas-electric hybrid systems (Table 7)

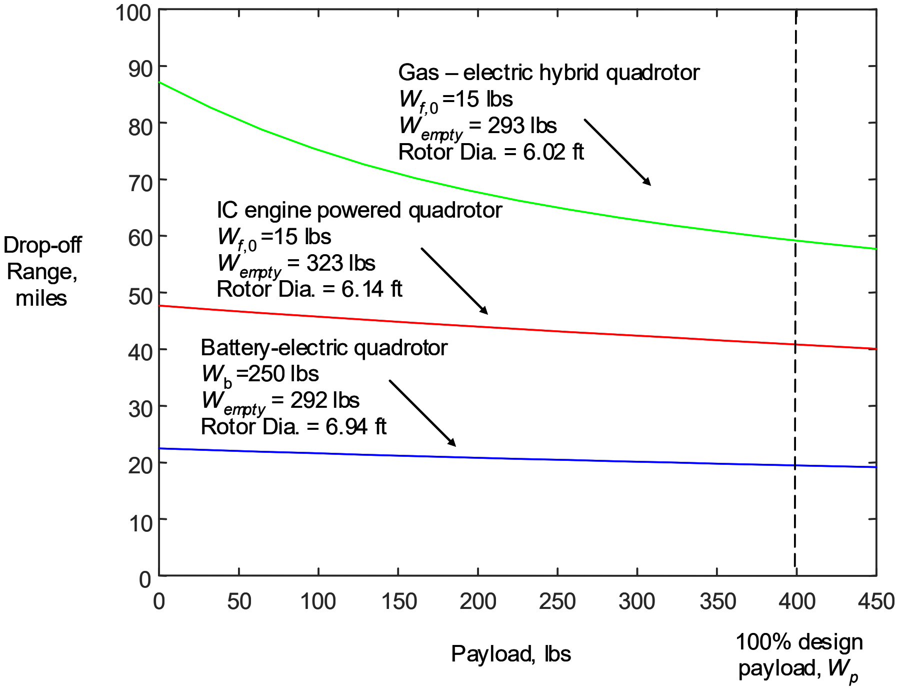

Fig. 75 Payload drop-off range for partial payload operation for design payload W_p = 400 lb

Figures 74 and 75 again show that the hybrid configuration is the most adaptable for multiple payload mission scenarios and is thus able to achieve significantly higher payload drop-off ranges for an equivalent level of onboard energy. In this case, the vehicle empty weights and rotor diameters of each design are similar for the same size design payload; however, the weight of the battery-electric configuration tends to scale much more rapidly due to large battery weights compared to the much lower weight of fuel for the other two configurations.

6. Conclusions

This research developed a comprehensive suite of computational tools for the design, optimization, and analysis of battery-electric, IC engine-powered, and series gas-electric hybrid multirotor VTOL UAVs at the medium scale (100–1000 lb range). The results show that, for maximum overall performance when operating at 100% design payload, the IC engine-powered configuration outperforms both the battery-electric and hybrid gas-electric designs. However, the results also show that the hybrid-electric configuration is able to achieve the highest overall range during partial load and variable payload missions such as the payload drop-off scenario. Finally, the results show that the battery-electric configuration is only competitive when the mission radius is below about 25 miles. Greater than this range, the battery-electric designs do not scale with battery size, while the mission range for both the IC engine-powered and serial gas-electric hybrid configurations essentially scale linearly with onboard fuel capacity. In all configurations at the medium scale, significant hover duration and range benefits were gained by the inclusion of gearboxes within the drive system designs. The benefits of the gearboxes became more significant with increasing payload. One of the key advantages of the gas-electric hybrid is the ability for the system to function as a virtual CVT whereby the engine speed varies independently of rotor RPM to maintain the most efficient operating point for a given payload level. Based on this, the partial load efficiency of the ESC is critical in order for the hybrid system to maintain its advantages over the IC engine-powered configuration. Another potential area to consider, which was not considered in this study, is the use of a mechanical CVT in the IC engine-powered drivesystem. If the partial load efficiency of the CVT can exceed that of the ESC then the IC engine-powered multirotor VTOL UAV at medium scale could be very close to the hybrid case. Another potential method for further increasing performance of the hybrid gas-electric configuration, which is explored in this study, is the concept of battery-assisted hover. Battery-assisted hover enables a smaller engine to be utilized fully during cruise while both the engine and battery power are combined during hover. The results of this study found only limited benefits of this method at the medium scale investigated. Finally, another key advantage of both the battery-electric and gas-electric hybrid configurations is the relative ease of adding more rotors due to the lack of mechanical connection to the engine. In the case of the gas-electric hybrid, it was found that going from a quadrotor ($N_r = 4$) to an octorotor ($N_r = 8$) configuration had a similar beneficial effect on flight range as gearboxes. Overall, the series gas-electric hybrid configuring shows much benefit for VTOL UAV applications at the medium scale.

7. References

1. Chan CC, Chau KT. Modern electric vehicle technology. Oxford (England): Oxford University Press; 2001.
2. Aldridge EC, Stenbit JP. Unmanned aerial vehicles roadmap: 2002–2027. Washington (DC): Office of the Secretary of Defense; 2002 Dec.
3. Perazzola C. Tomorrow's ground power today. Proceedings of the SAE TOPTEC Conference; Society of Automotive Engineers; 2002 June; Warrendale, PA.
4. Wilson SB. Micro air vehicle project. Proceedings of the DARPA Tech Symposium; 2002; Anaheim, CA.
5. Norris G. Hydrogen power offers leap forward for UAVs. Flight International. 2003:33.
6. Bennett E. NASA's helios prototype-soaring to a new record. SAMPE Journal. 2002;38(3):41–47.
7. Harmats M, Weihs D. Hybrid-propulsion high-altitude long-endurance remotely piloted vehicle. Journal of Aircraft. 1999;36(2):321–331.
8. Unmanned Systems Technology. Top flight technologies announces hybrid multirotor drone. 2015 Mar 20 [accessed 2015 Mar]. http://www.unmannedsystemstechnology.com/2015/03/top-flight technologies announces-hybrid-multirotor-drone/.
9. Johnson W. Helicopter theory. Princeton (NJ): University Press; 1980.
10. Bershadsky D, Haviland S, Johnson E. Electric multirotor propulsion system sizing for performance prediction and design optimization. Proceedings of the 57th AIAA/ASCE/AHS/ASC Structures, Structural Dynamics, and Materials Conference; 2016 Jan 4–8; San Diego, CA. https://doi.org/10.2514/6.2016-0581.
11. Johnson W. NASA design and analysis of rotorcraft. Washington (DC): NASA (US); 2015 Apr. Report No.: NASA/TP-2015-218751.
12. Gur O, Rosen A. Optimizing electric propulsion systems for unmanned aerial vehicles. Proceedings of the 12th AIAA/ISSMO Multidisciplinary Analysis and Optimization Conference; 2008 Sep. 10–12; Victoria, Canada.

13. Rejman E, Rejman M. Gears weight equations – gear chain weight calculation methodology. 2011 Feb [accessed 2020 May 6]. http://mech-ing.com/journal/Archive/2011/2/22_E.Rejman, M.Rejman.pdf.

14. Schömann J. Hybrid-electric propulsion systems for small unmanned aircraft [PhD thesis]. [Munich (Germany)]: Technical University of Munich; 2014.

List of Symbols, Abbreviations, and Acronyms

AGMA	American Gear Manufacturing Association
BMEP	brake mean effective cylinder pressure
CVT	continuously variable transmission
DARPA	Defense Advanced Research Projects Agency
DC	direct current
EM	electric motor
ESC	electronic speed controller
HEV	hybrid-electric vehicle
IC	internal combustion
Li-Po	lithium polymer
MAV	micro aerial vehicle
NASA	National Aeronautics and Space Administration
UAV	unmanned aerial vehicle
VTOL	vertical takeoff and landing
WOT	wide open throttle

1 (PDF)	DEFENSE TECHNICAL INFORMATION CTR DTIC OCA
1 (PDF)	CCDC ARL FCDD RLD CL TECH LIB
1 (PDF)	UNIVERSITY OF TENNESSEE H DESMIDT
1 (PDF)	CCDC ARL FCDD RLV P M RIGGS